KU LEUVEN

ARENBERG DOCTORAL SCHOOL
Faculty of Science

Dynamics and phase behavior of (non-)ideal liquid-crystals under shear

Christian Lang

Supervisor:
Prof. dr. M. P. Lettinga

Dissertation presented in partial fulfillment of the requirements for the degree of Doctor of Science (PhD): Physics

February 4, 2019

Dynamics and phase behavior of (non-)ideal liquid-crystals under shear

Christian LANG

Examination committee:
Prof. dr. C. Maes, chair
Prof. dr. M. P. Lettinga, supervisor
Prof. dr. C. Clasen
Prof. dr. C. Haesendonck
Prof. dr. M. Wuebbenhorst
Prof. dr. J. K. G. Dhont
(University of Düsseldorf)
Prof. dr. P. P. A. M. van der Schoot
(Eindhoven University of Technology)

Dissertation presented in partial fulfillment of the requirements for the degree of Doctor of Science (PhD): Physics

February 4, 2019

Uitgegeven in eigen beheer, Christian Lang, Celestijnenlaan 200A, box 2402, B-3001 Leuven (Belgium)

Preface

The goal of this thesis is to form a better understanding of the influence of non-ideality parameters such as flexibility and polydispersity on the rheological behavior of rodlike particle suspensions. Special focus is laid on the behavior of rods under simple shear flow.

This research is funded by the European Commission within the Horizon 2020 project under the DiStruc Marie Skłodowska Curie innovative training network; Grant Agreement No. 641839.

The author acknowledges Pavlik Lettinga and Jan Dhont for their great help and the manifold fruitful discussions. Further thanks go to the board of DiStruc who provided the author with uncountable helpful comments and suggestions. I am deeply indebted to my girlfriend Judith for her endless patience with my writing of this thesis.

Abstract

As the simplest form of polymeric materials, rodlike polymers provide a unique opportunity to test and review the theory of polymer dynamics. Liquid crystalline solutions of rodlike particles are of high industrial relevance and their flow behavior during processing strongly influences the properties of the final products.

While industrially used materials are mostly non-ideal in several aspects such as flexibility and polydispersity of the particles, the theory of polymer dynamics is best applicable only to ideal rods. The attempt of this thesis is to provide new insights into the effect of such non-ideality parameters on the flow behavior of rodlike suspensions.

Rodlike bacteriophages are used in this work in order to formulate materials with well-defined system characteristics, which can be alternated in a controlled way to understand non-ideal suspensions of rods. These rodlike viruses form various liquid-crystalline phases in aqueous suspension. However, here we focus on isotropic suspensions which have neither positional nor orientational order in the equilibrium state.

The dynamics and phase behavior of suspensions in the isotropic state are measured under flow by means of a combination of small angle neutron scattering with rheology and heterodyne dynamic light scattering under flow. Based on the experimental outcome, the theory of rodlike polymers is reviewed.

In chapter 2, a revised theory for ideal rodlike particles is derived and tested in chapter 4. In chapter 5, we test the theory against the influence of non-ideality parameters to gain a deeper understanding of the nature of these influences. Particularly, new expressions for the rotational diffusion coefficient under tube dilation and a non-equilibrium pair-correlation function are derived to supplement the Fokker-Planck equation for rods.

In chapter 5, it is shown theoretically as well as experimentally that particle

morphology is one of the key influences on the flow behavior of rods. In this respect, length and flexibility are two counteracting parameters. With increasing length, the dynamics of the rods slow down significantly leading to higher zero shear viscosities, while an increase of particle flexibility has the opposite effect. Furthermore, the onset of shear thinning depends crucially on the particle length. An increase in length shifts the onset of shear thinning to smaller shear-rates. In section 5.3.2, we use the understanding of this length dependence to make our theoretical predictions quantitative by experimentally determining the prefactor of the rotational diffusion coefficient in the tube model for the first time. This is very useful, as it is the basis for the understanding of other phenomena studied here and reported in literature. Due to a morphological transition to a hairpin state, an increase in flexibility causes an increase of the viscosity in the intermediate and high shear-rate regime, such that under strong flow, higher length and higher bending rigidity are both promoting shear thinning.

In sections 4.3.1 and 5.2, small amplitude oscillatory shear is used to demonstrate that the rotational diffusion and the particle flexibility crucially influences the quasi-linear flow behavior of rods. It is found that, not unlike polymers, rods of finite stiffness possess a relaxation time spectrum, see section 5.5.

Extensional flow measurements are conducted to demonstrate the effect of flexibility in the highly non-linear flow regime, see section 5.4. It is found that an increase in particle flexibility leads to a decrease in extensional viscosity. The Trouton ratios of rodlike systems are shown to be comparatively large despite of low normal stresses.

In section 5.6, it is demonstrated that the zero shear behavior of polydisperse rodlike particle suspensions does not involve higher complexities, while the shear thinning behavior becomes very complex and, therefore, cannot be understood by employing linear mixing rules in the governing equations for particle dynamics.

Finally, it is shown in section 5.7 that a high enough length of rods is crucial for a gradient shear banding transition to occur. Also, it is demonstrated that none of the systems under investigation undergo stable gradient shear banding.

Beknopte samenvatting

Als de eenvoudigste vorm van polymere materialen bieden staafvormige polymeren een unieke gelegenheid om de theorie van de polymeerdynamica te testen en te beoordelen. Vloeibaar kristallijne oplossingen van staafvormige deeltjes hebben een hoge industriële relevantie en hun stromingsgedrag heeft daardoor een sterke invloed op de eigenschappen van de eindproducten.

Hoewel industriëel gebruikte materialen meestal niet-ideaal zijn in een of meerdere aspecten, zoals flexibiliteit en polydispersiteit van de deeltjes, is de theorie van de polymeerdynamica tot op de dag van vandaag alleen in staat om ideale staven te beschrijven en zelfs deze theoriëen zijn niet goed getest voor niet-linear stromingsgedrag. In dit profschrift wordt gepoogd om nieuwe inzichten te verkrijgen in het effect van dergelijke niet-idealiteitsparameters op het stromingsgedrag van staafachtige suspensies.

Om materialen te formuleren met duidelijk gedefiniëerde systeemkarakteristieken, die op een gecontroleerde manier kunnen worden gevariëerd om niet-ideale suspensies van staven te begrijpen, worden staafvormige bacteriofagen in dit werk gebruikt. Deze staafvormige virussen vormen verschillende vloeibaar-kristallijne fasen in waterige suspensie. In dit proefschrift richten we ons echter op de isotrope fase waar staven geen positionele zowel als orientationele ordening hebben.

Het dynamick- en fasegedrag van deze vloeibaar kristallijne oplossingen onder stroming word gemeten door middel van een combinatie van kleine-hoek-neutronenverstrooiïng met reologie en heterodyne dynamische lichtverstrooiïng onder stroming. Gebaseerd op het experimentele resultaat, wordt de theorie van staafvormige polymeren herzien.

Een herziene theorie voor staafvormige deeltjes is afgeleid en getest tegen de invloed van niet-idealiteitsparameters om een dieper inzicht te krijgen in de aard van deze invloeden. In het bijzonder worden nieuwe uitdrukkingen voor de rotationele diffusiecoëfficiënt onder buisdilatatie en een niet-evengewichtspaar-

correlatiefunctie afgeleid om den Fokker-Planck-vergelijking voor staven te vervolledigen.

Er wordt zowel theoretisch als experimenteel aangetoond dat de deeltjesmorfologie van zeer grote invloed is op het stromingsgedrag van staafjes. Daarbij zijn lengte en flexibiliteit twee tegenwerkende parameters. Met toenemende lengte vertraagt de dynamica van de staven aanzienlijk, leidend tot hogere nulschuifviscositeiten, terwijl de toename van deeltjesflexibiliteit het tegenovergestelde effect heeft. Verder hangt het begin van afschuifverdunning in belangrijke mate af van de deeltjeslengte. Een toename in lengte verschuift het begin van afschuifverdunning naar kleinere afschuifsnelheden. Door gebruik te maken van de bibliotheek aan virus deeltjes konden we precies de lengte afhankelijkheid, gegeven door een al eerder theoretisch ingevoerde constante, bepalen, wat zeer nuttig is omdat dit al basis dient om alle andere fenomenen te begrijpen. Vanwege het belang van uitgesloten volume-interacties, verhoogt een toename in flexibiliteit de viscositeit in het tussenliggende en hoge afschuifsnelheidregiem, zodanig dat onder sterke stroming, hogere lengte en flexibiliteit beide afschuifverdunning bevorderen.

Oscillerende afschuifexperimenten met kleine amplitude worden gebruikt om an te tonen dat de rotatiediffusie en de flexibiliteit van de deeltjes van cruciaal belang zijn voor het quasi-lineaire stromingsgedrag van staven. Het is gebleken dat staven, net als polymeren, een relaxatietijdspectrum hebben.

Rekmetingen worden uitgevoerd om het effect van flexibiliteit in het zeer niet-lineaire stroomregime aan te tonen. Er is gevonden dat een toename in deeltjesflexibiliteit leidt tot een afname van de extensionele viscositeit. De Trouton-verhoudingen van staafvormige systemen zijn naar verhouding groot ondanks lage normaal spanningen.

Er wordt aangetoond dat het nulafschuifgedrag van polydisperse staafvormige deeltjessuspensies geen hogere complexiteiten met zich meebrengt, terwijl het afschuifverdunningsgedrag zeer complex wordt en daarom niet kan worden begrepen door lineaire mengregels te gebruiken in de van toepassing zijnde vergelijkingen voor deeltjesdynamica.

Tenslotte wordt aangetoond dat een voldoende hoge lengte van staven cruciaal is voor het optreden van een gradiënt-afschuifband-overgang. Het is ook aangetoond dat ogenschijnlijke gradiënten van de ordeparameter over de tussenruimte van een Couette-cel die wordt gedetecteerd door neutronenverstrooiing bewijzen dat geen gradiënt-afschuifband-instabiliteit optreedt.

List of Abbreviations

SANS	small angle neutron scattering
HDLS	heterodyne dynamic light scattering
DNA	deoxyribonucleic acid
PEG	polyethylene glycol
SAOS	small amplitude oscillatory shear
LDV	laser Doppler velocimetry
AFM	atomic force microscopy
DEK	Doi-Edwards-Kuzuu
MSD	mean square displacement
EOM	equation of motion
FP	Fokker-Planck
RTS	relaxation time spectrum
I-N	isotropic-nematic
LVE	linear viscoelastic
GSBI	gradient shear banding instability
s.t.	such that

List of Symbols

a	tube radius
A	surface area/baseline
B	amplitude
c	constant
cos	cosine
C	constant/modulation
d	thickness
d_t	total derivative with respect to time
D	current filament diameter
D_r	rotational diffusion coefficient
$D_{\min}$	minimum filament diameter
D_r^0	free rotational diffusion coefficient
D_r^{coll}	collective rotational diffusion coefficient
D_{tube}	tube diameter
$D_\parallel$	parallel diffusion coefficient
$D_\perp$	perpendicular diffusion coefficient
$\overline{D}_r$	reduced rotational diffusion coefficient
$\langle D_r \rangle$	mean rotational diffusion coefficient
exp()	exponential function

$\mathbf{E}$	rate of deformation tensor
$\mathbf{f}$	force
$\mathcal{F}$	free energy
g	full pair correlation function
g_i	relaxation strength (elastic modulus)
g^0	Onsager equilibrium pair correlation function
g^1	non-equilibrium pair correlation function
G_2	measured correlation function
G'	storage modulus
G''	loss modulus
h_{ij}	mobility matrix
$\mathbf{H}$	Oseen tensor
$\mathbf{I}$	unit tensor
I_0	scattering intensity amplitude
k_B	Boltzmann constant
$\mathbf{k}_f$	wave vector of scattered light
$\mathbf{k}_i$	wave vector of incident beam
K	width of the scattering intensity profile
lim	limit
L	length
$L^{(i)}$	length of species i
$L^{(m)}$	mean length
n	refractive index
N	number of beads/particles
p	pressure
P_2	second order Legendre polynomial

$\langle P_2 \rangle$	order parameter
Pe	Peclet number
Pe^{eff}	effective Peclet number
$\mathbf{q}$	scattering vector
$\mathbf{Q}$	traceless orientation tensor
$\mathbf{r}$	positional coordinate
$\mathbf{R}$	relative position coordinate
$\mathbf{R}^{(0,\theta)}$	rotation tensor
$\mathbf{R}_i$	position of bead nr. i
R_t	tube radius
R_{min}	minimum filament radius
R_1	initial filament radius
$\boldsymbol{\mathcal{R}}$	rotation operator
$\mathbf{s}$	surface normal vector
sin	sinus
$\mathbf{S}$	orientational ordering tensor
t	time coordinate
t_b	time of filament rupture
t_{osc}	Doppler frequency
T	temperature
$\mathcal{T}$	biaxiality
$\boldsymbol{T}$	Doi-Edwards torque
$\overline{\boldsymbol{T}}$	inter-particle torque
$\overline{\boldsymbol{T}}^0$	equilibrium inter-particle torque
$\overline{\boldsymbol{T}}^1$	non-equilibrium inter-particle torque
$\mathbf{u}$	orientation coordinate

U potential energy

$\mathbf{v}$ velocity

V pairwise additive inter-particle potential

$\mathcal{V}$ inter-particle potential

W work

X geometric correction constant

α angle

$\alpha_{\max}$ angle of the director

β reciprocal thermal energy/angle between wave vector and velocity

γ strain

$\dot{\gamma}$ shear-rate

$\mathbf{\Gamma}$ velocity gradient tensor

δ_{ij} unit tensor

$\delta()$ Dirac delta function

∂_t partial derivative with respect to time

ϵ deformation

$\dot{\epsilon}$ extension rate

ζ_r rotational friction coefficient

ζ_t bead friction coefficient

ζ_0 translational bead friction coefficient

$\zeta_\parallel$ parallel friction coefficient

$\zeta_\perp$ perpendicular friction coefficient

η shear viscosity

η_e elongational viscosity

η_s solvent viscosity

η_0 zero shear viscosity

$[\eta]$ intrinsic viscosity

$[\eta_e]$ intrinsic elongational viscosity

θ azimuthal angle

λ eigenvalue

λ_1 largest eigenvalue

ν number density

π Archimedes constant

Π_2 square root of the rate of deformation tensor

ρ dimensionless relative volume fraction

σ surface tension

$\boldsymbol{\Sigma}$ extra stress tensor

$\boldsymbol{\Sigma}^{(e)}$ elastic stress

$\boldsymbol{\Sigma}^{(v)}$ viscous stress

Σ_{21} shear stress

τ relaxation time/lag time

τ_e relaxation time of short scale particle undulation

τ_{end} longest relaxation time

τ_{flex} relaxation time of particle undulation

τ_r rotational relaxation time

$\tau_{\parallel}$ parallel relaxation time

φ volume fraction

φ_{NI} volume fraction at nematic-isotropic transition

φ_{IN} volume fraction at isotropic-nematic transition

$\varphi^{(i)}$ volume fraction of component i

$\varphi^{(m)}$ mean volume fraction

ϕ planar angle

χ	characteristic function
ψ	probability density function
$\boldsymbol{\omega}$	angular velocity

Contents

List of Figures

List of Tables

Chapter 1

Introduction

The widespread natural occurrence of rod-like particles is due to the large versatility of material functionality which can be tuned for example by changing their shape and size. Rods found in nature vary from inorganic nano-particles [3, 4, 5] to biological filaments [6, 7, 8, 9, 10, 11], which can have various chemical composition, causing their structure-property relations. Enhanced mechanical, electrical, and optical macroscopic material properties of suspensions [12, 13, 14, 15] are just some examples for these structural effects. This eminent presence has both motivated and triggered the use of rod-like particles in a vast diversity of engineering products such as biomedical applications [16], coatings [17], composite materials [18, 19, 20], and structured consumer products [21]. A lowering of the percolation threshold with increasing aspect ratio, allowing for network formation at relatively low particle volume fractions [22], and the formation of ordered liquid-crystalline phases [23, 24] play the most important role for these applications.

Neither of these transitions could occur in the absence of particle motility. This circumstance makes nearly all questions about material performance and structure a matter of particle dynamics. On the other hand, the effect of flow on rod-like particles strongly depends on the phase of the dispersion, or in other words, the positional and orientational ordering. The flow behavior can range from simple shear thinning at low concentrations [25, 26, 27] to rich dynamic behavior such as tumbling and kayaking in the nematic liquid-crystalline state [28, 29]. Despite the influence of the applied flow field on the rheological response, even shear flow as the simplest of all flow types can induce all aforementioned rheological characteristics in colloidal suspensions. A thorough understanding of the underlying physics governing the shear flow behavior of such systems can

serve as a benchmark for tackling a large amount of even more complicated rheological problems. Since the dynamics of rods in the nematic and smectic phase have been extensively studied [30, 31, 32, 33, 34, 29, 1, 35, 24, 36, 37, 38, 39, 40], the topics of this thesis are the dynamics and phase-behavior of semidilute rod-like colloidal suspensions under the influence of shear flow, since the complexities of particle-interaction and caging in this regime are not fully understood yet. Only a small part of this thesis is devoted to the comparison of simple shear flow and uniaxial elongational flow.

We consider a system of rods as ideal, if the rods are monodisperse and if the aspect ratio of the particles is larger than 100, with a persistence length much larger than the contour length, which also implies a high bending rigidity, given by the persistence length. Only such a system can be described by the theory of Onsager [41], which predicts the phase behavior of ideal rods. Many studies on the flow behavior of rod-like suspensions have been carried out for rather small aspect-ratio constituents [42, 43, 44], although the particle anisotropy has a strong influence on the rheological response. In addition, a majority of the large aspect-ratio particles, such as carbon nanotubes [45, 46, 47], glass fibers [48, 49] or actin [50, 51], that were studied, face the problems of polydispersity and particle flexibility. Such non-ideal particle characteristics can play a very important role and might hamper the identification of the origin of observable phenomena. Due to this reason, the focus of this study lies on identification of non-ideality influences on the shear flow behavior of rod-like colloids, starting off with identifying the response of ideal rods.

In order to classify such non-ideality aspects, a suitable model system is necessary. Ideally, such a system should suffice all criteria of ideal rods, such as large aspect ratio, high stiffness and monodispersity, but allows for a controlled alternation of these properties. Already in the 1930s, tobacco mosaic virus was found to show birefringence under flow [52, 53] and form liquid-crystalline structures [54]. Their stiffness and inherent monodispersity makes virus particles well-suited for rheological studies and hence superior to other potential rod-like model systems. Small drawbacks of tobacco mosaic virus , however, are its comparatively small aspect-ratio and the low yield of the production, which is an issue for macroscopic rheological experiments. This problem was solved by employing rod-like bacteriophages such as the fd wild-type virus [55]. Fd wild-type belongs to the lambda-class [56], which is a large class of rod-like bacteriophages with similar thickness but differing length and flexibility. Thus, the usage of this species allows for an alternation of particle characteristics. In order to explore an even higher bandwidth of non-ideality, bio-engineering of these phages can be employed, the first of which was reported by Overmann et al. [57]. Induced mutations in the virus genome thereby lead to an alternation of either length or stiffness of the wild-type virus or both. We exploit this to

produce fd-Y21M, which we call the ideal rod here, since this system undergoes an isotropic-nematic phase transition in perfect accordance with Onsager's theory.

A rheological investigation of structured fluids always needs to be accompanied by an analysis of the structural changes under flow, as the mechanical response underlies shear induced structural changes that need to be quantified. Optical and electrical birefringence [52, 58], optical microscopy [29], light scattering [59, 60], X-ray [61, 32], as well as neutron diffraction experiments [62, 63] are suitable for this purpose. The most straightforward of these experiments is small angle neutron scattering (SANS), since neither a signal loss at high concentrations, which is an issue in birefringent experiments, nor a beam-induced particle damage and sensitivity for back ground correction, which are issues for SAXS, occurs. Thus, SANS provides the best available contrast of all listed experiments. For this reason, rheology combined with SANS (rheo-SANS) is employed in this thesis. Parts of the study are supported by heterodyne dynamic light scattering under flow (flow-HDLS) which is employed to measure velocity profiles.

A number of studies report on the aforementioned kind of experimental investigations of fd wild-type virus and its mutants. Among the first were the measurement of rotational diffusion of the fd wild-type at different concentrations using electrical birefringence measurements [64] as well as the rheological investigation of shear thinning as a function of ionic strength of the suspending medium [55]. A characterization of the visco-elastic properties followed in 2000 [65] and not much later, the rheological properties of fd viruses in the nematic phase [29] as well as in the isotropic-nematic phase transition regime [34] were investigated. It was found that virus suspensions can undergo flow instabilities [66] and further investigations on the effect of ionic strength [67], as well as on the suspension to gel transition [68, 69] were conducted. For the mutant virus fdY21M, the phase behavior was compared to that of the wild-type virus [70], establishing the mutant as the ideal rod-like particle. Further studies additionally showed that fd behaves as a quasi-ideal rod in equilibrium as well as under flow [29].

Theoretical studies on the relations between structure and rheological properties of rod-like colloidal suspensions were performed already in the early 1920s with the prediction of an orbital motion of rods under shear flow in a dilute suspension [71]. The first theoretical description of rheological properties for semidilute rod-like suspensions under moderate shear flow followed later [72]. In the early 1960s, a first calculation of the rotational diffusion coefficient of rods in a dilute suspension was given [73]. This motivated further theoretical investigations in moderate [74] as well as strong [75] shear flow. With the advent of the tube model [76], a deeper analysis of the particle behavior under shear flow was made

feasible [77, 78, 79, 80], including a revision of the rotational diffusion coefficient in semidilute suspensions which allowed for the first sophisticated estimate of the zero shear viscosity [81]. Later, corrections for the zero shear viscosity were introduced [82]. The rheology of rod-like suspensions in the vicinity of the isotropic-nematic phase transition was reviewed by Olmsted in the late 1990s [83, 84, 85] and an ab initio theory for the isotropic, nematic as well as phase transition states by Dhont and Briels [86] followed.

In this thesis, we first investigate the shortcomings of Dhont-Briels theory [86] for semidilute systems, resulting from neglecting the caging of particles, in the first part of the thesis. We show that the tube model is essential to understand the concentration dependence of the zero shear viscosity, $\eta_0 \sim \varphi^2$, of our model rod suspensions, leading to the observable strong shear thinning over several orders of magnitude. A drawback of the tube model is that it cannot be used for quantitative predictions due to an unknown prefactor in the equations. In order to understand industrially relevant systems, such as those listed above, this quantification is inevitable. Therefore, in the second part of the thesis, we establish and use a library of wild-type and mutant rod-like bacteriophages, spanning a range of different contour lengths. This allows us to identify the prefactor in the tube model. Since, however, our rod-like particles vary in contour length, L, while their persistence length, L_p, is constant, we cannot rule out the possibility that the particles bend, strongly affecting the result of our estimation. Therefore, we use two systems of similar length but very different bending rigidity, $L_p k_B T$, in order to understand the effect of particle flexibility on the flow behavior. Combining both, the knowledge of the length dependence, and the knowledge of the flexibility dependence, completes the quantification of the tube model. To our knowledge, an experimental investigation of the prefactor of the tube model has not been accomplished before.

Due to the strong shear-thinning of our systems, which results in the extreme case of $d\eta/d\dot{\gamma} \sim L^{-1}$ for very long particles, we cannot neglect the possibility of shear banding. Therefore, we employ our library of rods to assess the possibility of shear banding in semidilute rod-like systems and find that our systems do not form stable shear bands. Finally, we investigate the behavior of rods in elongational flow, which is found to be in marked contrast to the behavior in shear flow, with regards to the effect of particle flexibility.

Chapter 2

Theory

2.1 Introduction

The alignment of dispersions of rods in shear flow is determined by a competition between rotational diffusion of the rods, which tends to randomize the rod orientation, and the shear rate, $\dot{\gamma}$, which tends to orient rods in order to decrease the macroscopic stress. The ratio of the two rates defines the Peclet number, $Pe = \dot{\gamma}/D_r$, where D_r is the rotational diffusion coefficient. In section 2.2, first the simple case of non-interacting rods is considered, calculating the diffusion rates due to hydrodynamic friction. When particles only interact via hydrodynamics, the intrinsic viscosity at high shear rates can also be calculated, if the concentrations are very low, and if all rods are disentangled, following Hinch and Leal [75], see section 2.3. For completeness, also two similar theoretical approaches for the intrinsic elongational viscosity are introduced, both of which are based solely on hydrodynamic interactions.

For entangled rods the situation becomes much more complicated. With increasing concentration, rods become entangled and cannot rotate freely due to topological constraints. Clearly, the topological constraints are due to simultaneous interactions between many rods. The increasing excluded volume causes a phase transition from the orientationally disordered isotropic phase to the orientationally ordered nematic phase. The thermodynamics of concentrated dispersions of very long and thin rods, up to concentrations well within the nematic phase, is accurately described within a second virial approach. Contrary to the dynamics, for the thermodynamics it is sufficient to consider simultaneous interactions between only two rods. It thus suffices to calculate the excluded

volume for just two rods to achieve an accurate description of the isotropic-to-nematic phase transition. Both dynamics and excluded volume effects play an important role in the rheological behavior of rod-dispersions, both of which should, therefore, be included in theoretical approaches addressing the flow behavior of rod-dispersions.

The collective rotational diffusion coefficient becomes equal to zero at the upper spinodal concentration related to the isotropic-to-nematic phase transition, while the rotational self-diffusion coefficient remains finite. Figure 2.1 displays simulations of the collective- and self-diffusion coefficients in dispersions of rods as a function of their concentration. For long and thin rods with hard-core interactions, the isotropic-to-nematic upper spinodal concentration is equal to $(L/d)\,\varphi = 4$, with L the length and d the diameter of the core of the rods, and φ the volume fraction.

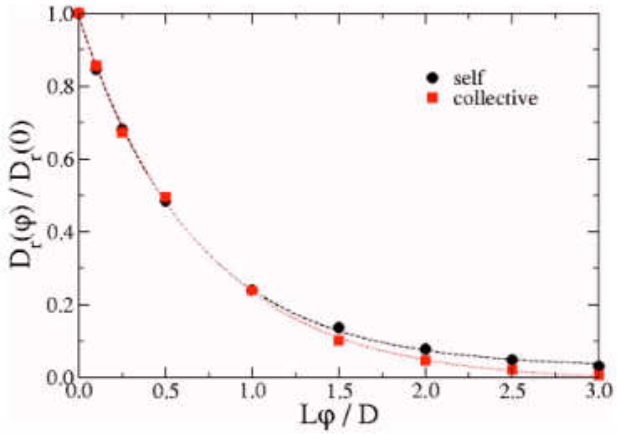

Figure 2.1: Relative rotational diffusion coefficient as a function of relative volume fraction for a single rod (black) and a collection of rods (red). Figure taken from Tao et al. [1]. The results are plotted up tho the highest concentration for which a simulation was feasible.

In section 2.4, we introduce the correct Fokker-Planck (FP) equation for the description of N interacting rods under flow, neglecting hydrodynamic interactions. In section 2.5, an approximate Fokker-Planck type of approach for the probability density of finding a particle with a certain orientation is introduced, following Doi, Edwards, and Kuzuu (DEK) [87]. This is used to give an estimate for the zero shear viscosity under the assumption that the dynamics is not affected by topological constraints involving multiple rod

interactions, and with the neglect of hydrodynamic interactions between the rods. The Fokker-Planck type of approach developed by Dhont and Briels [86] constitutes a microscopic foundation of the DEK theory. In addition, the DEK theory for the evaluation of visco-elastic response functions is based on free energy considerations, while in the Dhont-Briels approach the starting point is a microscopic expression for these response functions. Explicit expressions for rheological response functions are found that differ from those found in the semi-quantitative approach in the DEK theory, as shown in section 2.6. In section 2.6.1, it is shown that the Dhont-Briels theory is capable of predicting the critical slowing down of the collective rotational particle dynamics on approach to the upper isotropic-to-nematic spinodal, and in fact reproduces the Onsager theory for the isotropic-to-nematic transition. In this approach, the equilibrium form for the pair-correlation function for very long and thin rods is used, which neglects (i) the dynamics due to topological constraints involving multiple-rod interactions, (ii) the effect of shear flow on the pair-correlation function, and (iii) the effect of hydrodynamic interactions. Clearly, both the DEK approach and the FP approach developed by Dhont and Briels are expected to achieve an agreement with experiments on a qualitative and at most a semi-quantitative level.

In section 2.7, topological constraints for the particle dynamics are introduced on the basis of Doi's theory [77, 81, 88], which can be used within the Dhont-Briels framework to include topological constraints, as originally proposed within the frame work of the DEK theory. Moreover, the Dhont-Briels theory assumes that the pair-correlation function is not affected by shear flow, while in first approximation, the topological tube is also assumed to be unaffected by shear flow. The dilation of the tube due to shear is described at the end of section 2.7, as has been reported earlier [87, 89], but here, full consistency with the Dhont-Briels theory is achieved. The effect of shear flow on the pair correlation function, however, has not been addressed so far. A simplified approach to solve this problem is described in section 2.8 together with a possible but yet incomplete solution.

In the following, vectors and tensors are denoted with **bold** script. The reader is asked to infer either from the name of the object, or from context, whether an object is a vector or a tensor.

2.2 Friction coefficients of a single rod

Regarding a cylinder with length L and thickness d, located at a position $\mathbf{r}$ in space and pointing in the direction $\mathbf{u}$, it is evident that four principal

movements in space are possible. The rod can translate from $\mathbf{r}$ to $\mathbf{r}'$ either along or transverse to its long axis, or rotate either around its main axis, thereby changing neither $\mathbf{r}$ nor $\mathbf{u}$, or around its center point, from $\mathbf{u}$ to $\mathbf{u}'$. All of these motions can be induced by a Brownian force, but if the the rod is slender, $L/d \gg 1$, the rotation around the main axis can be neglected.

Suppose that a rod is situated in a fluid with a Newtonian solvent viscosity of η_s under an external field which exerts a torque $\overline{\mathbf{T}}$ on the rod. If the angular velocity $\boldsymbol{\omega}$ is small, the response will vary linearly with the signal, such that (s.t.)

$$\boldsymbol{\omega} \propto \overline{\mathbf{T}} \quad . \tag{2.1}$$

If the rod is thin enough, the motion around its associated vector $\mathbf{u}$ is negligible. Therefore, the two aforementioned vectors are both perpendicular to $\mathbf{u}$. A friction constant ζ_r is introduced as a linear coefficient in the given relation between torque and angular velocity:

$$\boldsymbol{\omega} = \frac{1}{\zeta_r}\overline{\mathbf{T}} \quad . \tag{2.2}$$

Picture the rod as made up by $N = L/d$ beads, numbered from $-N/2$ to $N/2$, where we call the bead to bead distance d. If the rod rotates, the velocity at the i-th bead will be

$$\mathbf{v}_i = \omega \times id\mathbf{u} \quad . \tag{2.3}$$

We neglect the hydrodynamic interaction and set the frictional force acting on segment N as $-\zeta_0 vN$, where the translational friction constant for a bead, $\zeta_0 = 3\pi\eta_s d$, is used. One can now calculate the torque due to hydrodynamic friction

$$\overline{\mathbf{T}} = \sum_{i=-N/2}^{N/2} id\mathbf{u} \times \zeta_0 \mathbf{v}_i = \eta_s \frac{\pi L^3}{4}\boldsymbol{\omega} \quad . \tag{2.4}$$

This defines the rotational friction coefficient

$$\zeta_r = \eta_s \frac{\pi L^3}{4} \quad . \tag{2.5}$$

The definition for the rotational diffusion constant is $D_r = k_B T \zeta_r^{-1}$, therefore, one has

$$D_r = \frac{4k_B T}{\pi\eta_s L^3} \tag{2.6}$$

as a first estimate for the rotational diffusion coefficient [87]. To include hydrodynamics, one can start with the linear constitutive equation for momentum density by Newton, which is written in terms of the force acting on a single bead $\mathbf{f}_i$ in the picture we adopted before,

$$\eta_s \Delta\mathbf{v} + \nabla p = -\sum_i \mathbf{f}_i \delta(\mathbf{r} - \mathbf{R}_i) \quad , \tag{2.7}$$

where p is the pressure and $\mathbf{R}_i$ the location of the i-th bead. Assuming that the fluid is incompressible, s.t.

$$\nabla \times \mathbf{v} = 0 \quad , \tag{2.8}$$

these two equations are solved by using the Fourier transform

$$\mathbf{v}(\mathbf{r}) = \sum_i \mathbf{H}(\mathbf{r} - \mathbf{R}_i) \cdot \mathbf{f}_i \quad , \tag{2.9}$$

where

$$\mathbf{H} = \frac{1}{8\pi\eta_s|\mathbf{r}|}(\mathbf{I} - \mathbf{rr}) \tag{2.10}$$

is called the Oseen tensor [90]. Since the beads of the rod move with the same velocity as the surrounding fluid, one gets

$$\mathbf{v}_i = \sum_j \mathbf{H}(\mathbf{R}_i - \mathbf{R}_j)\mathbf{f}_i \tag{2.11}$$

which has the nasty property of infinite trace. This problem is circumvented by just defining the main diagonal elements as $H_{nn} = \delta\zeta_r^{-1}$ and resetting

$$\mathbf{H} = \mathbf{H}(\mathbf{R}_i - \mathbf{R}_j) \quad \forall\ i \neq j \quad . \tag{2.12}$$

One can rewrite the Oseen tensor as

$$\mathbf{H} = (\mathbf{I} + \mathbf{uu})h_{ij} \quad , \tag{2.13}$$

using the mobility matrix

$$h_{ij} = \frac{1}{8\pi\eta_s|i-j|d} \quad . \tag{2.14}$$

We neglect the term h_{nn} for now. We can write the total force on the rod in terms of the thermodynamic potential

$$\sum_i \mathbf{f}_i = -\nabla(k_B T \ln\psi + U) \quad , \tag{2.15}$$

similarly, the torque on the rod is given by

$$\sum_i id\mathbf{u} \times \mathbf{f}_i = \boldsymbol{\mathcal{R}}(k_B T \ln\psi + U) \quad , \tag{2.16}$$

where $\boldsymbol{\mathcal{R}} = \mathbf{u} \times \partial/\partial\mathbf{u}$, ψ is the probability density of rod distribution and U is a yet unspecified potential. Substituting the result of the spatial as well as

orientational Fourier transforms into these equations yields

$$\sum_{i,j} \mathbf{H}_{ij}^{-1} \cdot [\mathbf{v} + jd\boldsymbol{\omega} \times \mathbf{u} - \nabla\mathbf{v} \cdot (\mathbf{r} + jd\mathbf{u})] = -\nabla(k_B T \ln\psi + U) \quad ,$$

$$\sum_{i,j} id\mathbf{u} \times \mathbf{H}_{ij}^{-1} \cdot [\mathbf{v} + jd\boldsymbol{\omega} \times \mathbf{u} - \nabla\mathbf{v} \cdot (\mathbf{r} + jd\mathbf{u})] = -\boldsymbol{\mathcal{R}}(k_B T \ln\psi + U) \quad (2.17)$$

Using the mobility matrix, this can be rewritten as

$$\sum_{i,j} h_{ij}^{-1} \left(\mathbf{I} - \frac{\mathbf{uu}}{2}\right) \cdot (\mathbf{v} - \nabla\mathbf{v} \cdot \mathbf{r}) = -\nabla(k_B T \ln\psi + U) \quad ,$$

$$\sum_{i,j} h_{ij}^{-1} ijd^2\mathbf{u} \times \left(\mathbf{I} - \frac{\mathbf{uu}}{2}\right) \cdot (\boldsymbol{\omega} \times \mathbf{u} - \nabla\mathbf{v} \cdot \mathbf{u}) = -\boldsymbol{\mathcal{R}}(k_B T \ln\psi + U) \quad (2.18)$$

By definition, the inverse mobility matrix gives us the friction coefficients $\zeta_t = \sum_{i,j} h_{ij}^{-1}$ $\zeta_r = \sum_{i,j} h_{i,j}^{-1} ij$. Plugging these coefficients into the equations above and solving for the velocity and angular velocity respectively gives

$$\mathbf{v} = \nabla\mathbf{v} \cdot \mathbf{r} - \frac{1}{\zeta_t}(\mathbf{I} + \mathbf{uu}) \cdot \nabla(k_B T \ln\psi + U) \quad ,$$

$$\boldsymbol{\omega} = \mathbf{u} \times \nabla\mathbf{v} \cdot \mathbf{u} - \frac{1}{\zeta_r}\boldsymbol{\mathcal{R}}(k_B T \ln\psi + U) \; . \quad (2.19)$$

Comparing the velocity to the full form obtained from the solution of the constitutive relation [87]

$$\mathbf{v} = -\left[\frac{1}{\zeta_\parallel}\mathbf{uu} + \frac{1}{\zeta_\perp}(\mathbf{I} - \mathbf{uu})\right] \cdot \nabla(k_B T \ln\psi + U) + \nabla\mathbf{v} \cdot \mathbf{r} \quad , \quad (2.20)$$

gives $\zeta_\parallel = \zeta_t/2$ and $\zeta_\perp = \zeta_t$. It can be observed that h_{ij} decreases quickly with $|i-j|$. Therefore, one can approximate the quantity as $h_{nm} \approx \overline{h}\delta_{nm}$, where

$$\overline{h} = 2\int_1^{N/2} djh_{0j} = \frac{\ln N/2}{4\pi\eta_s d} \quad . \quad (2.21)$$

From the definition of the friction coefficients, this gives:

$$\zeta_t = \frac{N}{\overline{h}} = \frac{4\pi\eta_s L}{\ln L/2d} \quad ,$$

$$\zeta_r = 2d^2\int_1^{N/2} dj\frac{j^2}{\overline{h}} = \frac{\pi\eta_s L^3}{3\ln L/2d} \quad . \quad (2.22)$$

Combined with the definition of the diffusion coefficient, this finally gives the perpendicular and parallel diffusion coefficients

$$D_\perp = \frac{k_B T \ln L/2d}{4\pi\eta_s L} \quad , \tag{2.23}$$

$$D_\parallel = \frac{k_B T \ln L/2d}{2\pi\eta_s L} \quad , \tag{2.24}$$

and the rotational diffusion coefficient [73]:

$$D_r^0 = \frac{3k_B T \ln L/2d}{\pi\eta_s L^3} \quad , \tag{2.25}$$

where the superscript zero was introduced to clarify that this quantity is strictly only valid in dilute suspensions.

2.3 Hydrodynamically interacting rods

While hydrodynamic interactions do not play an important role in shear flows of Brownian rods, strong effects of hydrodynamic interactions were stated for elongational flow [91, 82]. Although DEK theory can be used to calculate the elongational viscosity of rod-like colloidal suspensions as well, the absence of hydrodynamic interactions renders the approach questionable. The intrinsic elongational viscosity, $[\eta_e] = (\eta_e - 3\eta_s)/\eta_s\varphi$, instead, should be compared to either the theory by Batchelor [91]

$$[\eta_e] = \frac{4(L/d)^2}{9\ln \pi/\varphi} \quad , \tag{2.26}$$

or the theory by Shaqfeh and Fredrickson [82] which includes a more elaborate view on mid-range hydrodynamic interactions

$$[\eta_e] = \frac{4(L/d)^2}{9(\ln 1/\varphi + \ln\ln 1/\varphi) + 0.1518} \quad . \tag{2.27}$$

As described above, Brownian motion competes with shear flow in the sense that shear flow tends to orient the main axis of the particles along the velocity direction, while Brownian motion favors a random orientation of the rod. This competition can be described by the Fokker-Planck (FP) equation. Although different approaches of solving the FP equation can be found [78, 77, 86], only the Doi-Edward-Kuzuu (DEK) theory [77, 92, 87] and the Dhont-Briels theory [86] are discussed in detail here. For completeness, also a result of the

interaction-less Fokker-Planck equation in the limit of high shear rates, applied to dilute suspensions, is given [75]. Hinch and Leal solved the Fokker-Planck equation for low concentrations, high shear rates, and slow diffusion. Therefore, their equations apply to suspensions with high solvent viscosity such as the virus suspensions in glycerol of this work. Defining the so-called intrinsic viscosity, $[\eta] = (\eta - \eta_s)/\eta_s\varphi$, as a concentration-independent relative viscosity, then in the regime $1 \ll Pe \ll (L/d + d/L)^3$, the intrinsic viscosity becomes [75]

$$[\eta] = Pe^{-1/3}\frac{0.5(L/d)^2}{\ln L/d} \quad . \tag{2.28}$$

For even higher Peclet numbers, the viscosity becomes independent of Pe, such that $\eta \to \eta_s$.

2.4 N-particle Fokker-Planck equation

When interactions between particles are taken into account, the complexity of theoretical approaches increases dramatically. The first attempt to develop such a theory was by Hess [78], employing an irreversible-thermodynamics approach and using the phenomenological deGennes potential [93]. Later, Doi-Edwards [87] and Kuzuu [92] employed a Fokker-Planck type of approach. The governing equation for the probability density function $P_N(\mathbf{r}_1, ..., \mathbf{r}_N, \mathbf{u}_1, ..., \mathbf{u}_N; t)$ of finding N rods, located at the positions $\mathbf{r}_1$ to $\mathbf{r}_N$ with orientations $\mathbf{u}_1$ to $\mathbf{u}_N$, is the Fokker-Planck equation:

$$\begin{aligned}\partial_t P_N(\mathbf{r}_1, ..., \mathbf{r}_N, \mathbf{u}_1, ..., \mathbf{u}_N; t) = \sum_{i=1}^{N}\{&\nabla_i \cdot \hat{\boldsymbol{D}}(\mathbf{u}_i) \cdot [\nabla_i P_N + \beta P_N \nabla_i V] \\ &-\nabla_i \cdot [P_N \boldsymbol{\Gamma} \cdot \mathbf{r}_i] \\ &+D_r \boldsymbol{\mathcal{R}}_i \cdot [\boldsymbol{\mathcal{R}}_i P_N + \beta P_N \boldsymbol{\mathcal{R}}_i V] \\ &-\boldsymbol{\mathcal{R}}_i \cdot [P_N \mathbf{u}_i \times (\boldsymbol{\Gamma} \cdot \mathbf{u}_i)]\}\end{aligned} \tag{2.29}$$

where the used symbols will be clarified in the following sections. In order to make analytical progress, this equation has to be drastically reduced. An important step is the integration of this equation with respect to all variables except for $\mathbf{u}_1$. Since the integral theorems of Gauss and Stokes dictate $\int d\mathbf{r}_i \nabla_i \cdot (\cdot) = 0$ and $\oint d\mathbf{u}_i \boldsymbol{\mathcal{R}} \cdot (\cdot) = 0$, this integration leads to an extraordinary simplification, resulting in the following Fokker-Planck equation for the one-

particle probability density function $\psi(\mathbf{u}_1;t) = \int d\mathbf{r}_1 ... \int d\mathbf{r}_N \oint d\mathbf{u}_2 ... \oint d\mathbf{u}_N P_N$:

$$\partial_t \psi(\mathbf{u}_1;t) = D_r \boldsymbol{\mathcal{R}}_1 \cdot \left[\boldsymbol{\mathcal{R}}_1 \psi + \int d\mathbf{r}_1 ... \int d\mathbf{r}_N \oint d\mathbf{u}_2 ... \oint d\mathbf{u}_N \beta P_N \boldsymbol{\mathcal{R}}_1 V \right] - \boldsymbol{\mathcal{R}}_1 \cdot [\psi \mathbf{u}_1 \times (\boldsymbol{\Gamma} \cdot \mathbf{u}_1)] \quad (2.30)$$

This equation can be treated further by reduction of the virials resulting from the remaining integral. In the following, two approaches are given which accomplish an analytical solution of equation 2.30.

2.5 DEK theory

The Fokker-Planck equation for the probability density function of a particle's orientation, $\psi(\mathbf{u};t)$, on which the DEK theory is based reads

$$\partial_t \psi \;=\; \boldsymbol{\mathcal{R}} \cdot \overline{D}_r \left(\boldsymbol{\mathcal{R}} \psi - \beta \, \psi \, \boldsymbol{T} \right) - \boldsymbol{\mathcal{R}} \cdot [\psi \mathbf{u} \times (\boldsymbol{\Gamma} \cdot \mathbf{u})] \;, \quad (2.31)$$

where $\boldsymbol{\Gamma} = \nabla \mathbf{v}$ is the velocity gradient tensor, and where

$$\boldsymbol{T} \;=\; -\boldsymbol{\mathcal{R}} \mathcal{V} \,, \quad (2.32)$$

is the torque on the test rod through the interaction with a single neighboring rod, and where $\overline{D}_r$ is an effective diffusion coefficient that accounts for topological constraints (which will be discussed later), and $\mathcal{V}$ is the pair-interaction potential. The last term describes the influence of shear flow. For the pair-interaction potential, a Maier-Saupe type of potential is used (which will be discussed later) with an unknown prefactor that characterizes the strength of the interactions.

For the derivation of the equation of motion of the orientational order parameter tensor $\mathbf{S} = \oint d\mathbf{u} \psi \mathbf{u}\mathbf{u} = \langle \mathbf{u}\mathbf{u} \rangle$ from this equation of motion, a factorization closure relation is used for averages of fourth order dyadic products of $\boldsymbol{u}$. Such an equation of motion is then used, within the DEK theory, to obtain expressions for rheological response functions as follows. Since the elastic stress is related to the change in free energy [87], we can write

$$\delta \mathcal{F} = \boldsymbol{\Sigma}^{(e)} : \boldsymbol{\delta\varepsilon} \;\;, \quad (2.33)$$

with a virtual deformation $\delta\varepsilon$. The free energy of the fluid is given by

$$\mathcal{F} = \nu \oint d\mathbf{u} (k_B T \psi \ln \psi + \psi \mathcal{V}) \;\;. \quad (2.34)$$

For an instantaneous deformation, the velocity gradient dominates equation 2.31, which can thus be approximated as

$$\delta\psi = -\boldsymbol{\mathcal{R}} \cdot [\psi \mathbf{u} \times (\boldsymbol{\Gamma} \cdot \mathbf{u})]\, \delta t \quad , \tag{2.35}$$

where $\boldsymbol{\Gamma}\delta t = \boldsymbol{\delta\varepsilon}$ was used. We can insert this expression into the perturbation of the free energy, giving

$$\delta\mathcal{F} = \nu \oint d\mathbf{u}\psi[-k_B T \boldsymbol{\mathcal{R}} \cdot (\mathbf{u} \times \boldsymbol{\delta\varepsilon} \cdot \mathbf{u}) + (\mathbf{u} \times \boldsymbol{\delta\varepsilon} \cdot \mathbf{u}\psi) \cdot \boldsymbol{\mathcal{R}}\mathcal{V}] \quad . \tag{2.36}$$

Using the mathematical identity (where summation over repeated indices is assumed)

$$\boldsymbol{\mathcal{R}} \cdot (\mathbf{u} \times \boldsymbol{\delta\varepsilon} \cdot \mathbf{u}) = -3\delta\varepsilon_{\mathrm{mn}} \left(u_{\mathrm{m}} u_{\mathrm{n}} - \frac{1}{3}\delta_{\mathrm{nm}} \right) \quad ,$$

leads to

$$\delta\mathcal{F} = \nu \boldsymbol{\delta\varepsilon} : [3k_B T(\mathbf{S} - \frac{1}{3}\mathbf{I}) - \langle (\mathbf{u} \times \boldsymbol{\mathcal{R}}\mathcal{V})\, \mathbf{u} \rangle] \quad . \tag{2.37}$$

This gives the elastic stress tensor to a first approximation, where $\mathcal{V} = 0$ [87],

$$\boldsymbol{\Sigma}^{(e)} = 3\nu k_B T \left(\mathbf{S} - \frac{1}{3}\mathbf{I} \right) \quad . \tag{2.38}$$

The viscous part of the stress tensor can be estimated by regarding the viscous dissipation:

$$W = \boldsymbol{\Gamma} : \boldsymbol{\Sigma}^{(v)} \quad . \tag{2.39}$$

In the simplest case [87], one can write the velocity of the i-th bead of our rod as

$$\mathbf{v}_i = -id(\boldsymbol{\omega}_0 \times \mathbf{u} - \boldsymbol{\Gamma} \cdot \mathbf{u}) = -id\mathbf{u}\, (\boldsymbol{\Gamma} : \mathbf{uu}) \quad , \tag{2.40}$$

where $\boldsymbol{\omega}_0 = \mathbf{u} \times \boldsymbol{\Gamma} \cdot \mathbf{u}$. With the friction force $\mathbf{f}_i = \zeta_0 \mathbf{v}_i$, one can denote the work done by the fluid as [87]

$$W = \nu \sum_i \langle \mathbf{f}_j \cdot \mathbf{v}_j \rangle = \nu \sum_{i=-N/2}^{N/2} \zeta_0 i^2 d^2 \langle (\boldsymbol{\Gamma} : \mathbf{uu})^2 \rangle =$$

$$= \nu\zeta_r \langle (\boldsymbol{\Gamma} : \mathbf{uu})^2 \rangle \quad . \tag{2.41}$$

by defining the fourth order alignment tensor, $\mathbf{S}^{(4)} = \langle \mathbf{uuuu} \rangle$, this leads to

$$\boldsymbol{\Sigma}^{(v)} = \frac{\nu k_B T}{2D_r^0} \mathbf{S}^{(4)} : \boldsymbol{\Gamma} \quad . \tag{2.42}$$

Together with the pure solvent stress, one finds the full extra stress tensor for the suspension

$$\mathbf{\Sigma} = 2\eta_s \mathbf{E} + \mathbf{\Sigma}^{(e)} + \mathbf{\Sigma}^{(v)} \quad , \tag{2.43}$$

where $\mathbf{E} = (\mathbf{\Gamma} + \mathbf{\Gamma}^T)/2$ is the rate of deformation tensor. The suspension viscosity can be calculated from equations 2.43 and the equation of motion resulting from equation 2.31 as $\eta = \mathbf{\Sigma}_{21}/\dot{\gamma}$.

For weak velocity gradients, so in the zero-shear limit, the viscosity can be given analytically. To see this, we multiply equation 2.31 by $\mathbf{uu}$ and integrate over $\mathbf{u}$, assuming for simplicity that $\mathcal{V} = 0$, giving an equation of motion for the orientational ordering tensor S:

$$d_t \mathbf{S} = -6D_r^0 \left[\mathbf{S} - \frac{1}{3}\mathbf{I} \right] + \mathbf{\Gamma} \cdot \mathbf{S} + \mathbf{S} \cdot \mathbf{\Gamma}^T - 2\mathbf{S}^{(4)} : \mathbf{E} \quad . \tag{2.44}$$

For small velocity gradients, this is approximated as

$$d_t \mathbf{S} = -6D_r^0 \left[\mathbf{S} - \frac{1}{3}\mathbf{I} \right] + \frac{1}{5}\mathbf{E} \quad , \tag{2.45}$$

where the following closure for the fourth order alignment tensor was used:

$$\mathbf{S}^{(4)} \approx \frac{1}{15} \left(\delta_{ij}\delta_{kl} + \delta_{ik}\delta_{jl} + \delta_{il}\delta_{jk} \right) \quad , \tag{2.46}$$

leading to the solution of equation 2.45:

$$\mathbf{S}(t) = \frac{1}{5} \int_{-\infty}^{0} dt' \exp\left[-6D_r^0 (t - t') \right] \mathbf{E}(t') \quad . \tag{2.47}$$

From equation 2.47, a simplified expression for the elastic stress tensor can be derived:

$$\mathbf{\Sigma}^{(e)} = \frac{3}{5} \nu k_B T \int_{-\infty}^{0} dt' \exp\left[-6D_r^0 (t - t') \right] \mathbf{E}(t') \quad , \tag{2.48}$$

which gives the following elastic contribution to the shear stress:

$$\Sigma_{21}^{(e)} = \frac{\nu k_B T}{10 D_r^0} \dot{\gamma} \quad . \tag{2.49}$$

From equation 2.42 and the closure, one finds for the viscous contribution to the shear stress:

$$\Sigma_{21}^{(v)} = \frac{\nu k_B T}{30 D_r^0} \dot{\gamma} \quad . \tag{2.50}$$

The zero shear viscosity, resulting from this stress tensor reads [87]

$$\eta_0 = \eta_s \left[1 + \frac{2\pi}{45 \ln(L/d)} \nu L^3 \right] \quad . \tag{2.51}$$

2.6 Dhont-Briels theory

The DEK theory has been reconsidered by Dhont and Briels, departing from an exact Fokker-Planck equation (but also with the neglect of hydrodynamic interactions), equation 2.29 , and from a microscopic expression for visco-elastic response functions. The analysis is based on the equation of motion

$$\partial_t \psi = D_r^0 \boldsymbol{\mathcal{R}} \cdot \left[\boldsymbol{\mathcal{R}} \psi - \beta \psi \overline{\mathbf{T}} \right] - \boldsymbol{\mathcal{R}} \cdot \left[\psi \mathbf{u} \times (\boldsymbol{\Gamma} \cdot \mathbf{u}) \right] \quad , \tag{2.52}$$

where D_r^0 is the rotational diffusion coefficient of a freely rotating rod (without the influence of interactions with other rods) and $\overline{\mathbf{T}}$ is the effective torque acting on the test particle due to the presence of the other rods

$$\overline{\mathbf{T}} = -\nu \int d\mathbf{R} \oint d\mathbf{u}' \psi(\mathbf{u}'; t) g(\mathbf{R}, \mathbf{u}, \mathbf{u}'; t) \boldsymbol{\mathcal{R}} \mathcal{V}(\mathbf{R}, \mathbf{u}, \mathbf{u}') \quad . \tag{2.53}$$

Note that in the DEK-theory, the torque is given by equation 2.32, which is simply the torque due to interaction of the test rod with a single neighboring rod, in contrast to the torque in the above equation which is the torque acting on the test rod by all other rods present in the system averaged with respect to their positions and orientations. The latter torque is a function of concentration and shear rate through the pair correlation function $g(\mathbf{R}, \mathbf{u}, \mathbf{u}'; t)$. The above equation of motion can be derived from the N-particle Fokker-Planck equation by integration with respect to the orientations of all rods except for one rod, and with respect to all position coordinates of the N rods. Here, ν is the number density, $\mathbf{R} = \mathbf{r} - \mathbf{r}'$ is the inter-particle distance, and, as before, $\mathcal{V}$ is the bare pair-interaction potential. The first term on the right-hand side of equation 2.52 describes the Brownian motion of the test particle and the third term describes the torque on the particle which is induced by the flow field. The above two equations represent the first equation of motion in a hierarchy of equations of motion for reduced probability density functions: the next equation of motion in this hierarchy is the equation of motion for the pair correlation function, which depends on the three-particle correlation function. If one would be able to find an exact (or at least an accurate approximate) expression for the pair correlation function, including multiple rod interactions, the two above equations would accurately describe the orientational probability density function ψ, which can be used in expressions for rheological response functions. The problem is that such an accurate approximate expression for the pair correlation in concentrated suspensions under flow conditions does not exist and its calculation is not feasible analytically. In the approach by Dhont and Briels [86], the pair correlation function is simply approximated by the equilibrium pair correlation function for very long and thin rods, which is equal to $\exp\{-\beta \mathcal{V}\}$. As discussed in the beginning of this introduction, this approach neglects the dynamics involving topological constraints where

multiple-rod interactions are essential, as well as the shear-rate dependence of the pair correlation function. Within this simple approximation, it is easily shown that

$$\overline{\boldsymbol{T}} = -\boldsymbol{\mathcal{R}}\overline{V} \, , \tag{2.54}$$

where the effective pair-interaction potential is equal to

$$\overline{V} = 2\nu d L^2 \beta^{-1} \oint d\mathbf{u}' \psi(\mathbf{u}';t)|\mathbf{u}\times\mathbf{u}'| \quad . \tag{2.55}$$

Within a Ginzburg-Landau type of expansion with respect to the orientational order parameter, we can approximate [1]

$$|\mathbf{u}\times\mathbf{u}'| \approx \frac{5\pi}{16}\left[1-\frac{3}{5}\mathbf{u}\mathbf{u}:\mathbf{u}'\mathbf{u}'\right] \quad , \tag{2.56}$$

so that equation 2.55 simplifies to

$$\overline{V} = \frac{5\pi}{8\beta}\nu d L^2 \left(1-\frac{3}{5}\mathbf{S}:\mathbf{u}\mathbf{u}\right) \quad , \tag{2.57}$$

yielding a closed expression for equation 2.52. Note that in the DEK theory, this so-called Maier-Saupe potential is introduced by hand, leading to an unknown prefactor that is stated to characterize the strength of the interactions.

Moreover, in the Dhont-Briels approach, the calculation of the stress tensor is based on a microscopic expression for the stress tensor. This leads to the following expression for the deviatoric part of the stress tensor in terms of the orientational order parameter tensor

$$\begin{aligned}\boldsymbol{\Sigma}^{(e)} &= 2\eta_s\dot{\gamma}\hat{\boldsymbol{E}} + 3\nu k_B T\left[\boldsymbol{S}-\frac{1}{3}\boldsymbol{I}+\frac{L}{d}\varphi\left(\boldsymbol{S}^{(4)}:\boldsymbol{S}-\boldsymbol{S}\cdot\boldsymbol{S}\right)\right] \\ &\quad +\frac{1}{6}Pe\left[\boldsymbol{S}^{(4)}:\hat{\boldsymbol{E}}-\frac{1}{3}\boldsymbol{I}\,\boldsymbol{S}:\hat{\boldsymbol{E}}\right]\end{aligned} \tag{2.58}$$

where $\hat{\boldsymbol{E}} = \hat{\boldsymbol{E}}/\dot{\gamma}$, and, as before, the volume fraction of rods is equal to $\varphi = \nu L d^2\pi/4$, and $\mathbf{S}^{(4)} = \langle\mathbf{uuuu}\rangle$.

Additionally, the equation of motion for the orientational ordering tensor, including thermodynamic interactions, can be found from multiplication of

[1] A systematic expansion of $|\mathbf{u}\times\mathbf{u}'|$ with respect to orthogonal polyadic products leads to the more correct prefactor 3/4, which also gives the correct value for the concentration of the upper isotropic-to-nematic spinodal of $(L/d)\varphi = 4$, instead of 5.

equation 2.52 with **uu** and subsequent integration over **u**, using the potential specified in equation 2.57:

$$d_t \boldsymbol{S} = -6D_r^0 \left[\boldsymbol{S} - \frac{1}{3}\boldsymbol{I} + \frac{L}{d}\varphi \left(\boldsymbol{S}^{(4)} : \boldsymbol{S} - \boldsymbol{S} \cdot \boldsymbol{S} \right) \right] + \boldsymbol{\Gamma} \cdot \boldsymbol{S} + \boldsymbol{S} \cdot \boldsymbol{\Gamma}^T - 2\boldsymbol{S}^{(4)} : \boldsymbol{E} \quad . \tag{2.59}$$

For $\mathbf{S}^{(4)}$, one can employ the closure relation [86]

$$\begin{aligned} \mathbf{S}^{(4)} : \mathbf{M} &= \frac{1}{5}(\mathbf{S} \cdot \mathbf{M} + \mathbf{M} \cdot \mathbf{S} - \mathbf{S} \cdot \mathbf{S} \cdot \mathbf{M} \\ &- \mathbf{M} \cdot \mathbf{S} \cdot \mathbf{S} + 2\mathbf{S} \cdot \mathbf{M} \cdot \mathbf{S} + 3\mathbf{S}\mathbf{S} : \mathbf{M}) \quad , \end{aligned} \tag{2.60}$$

with $\mathbf{M}$ an arbitrary but symmetric tensor, to obtain a closed equation of motion for $\mathbf{S}$. In the DEK theory, a simple factorization of $\mathbf{S}^{(4)}$ is used, which is not very accurate.

2.6.1 Isotropic-nematic phase transition

The equation of motion 2.59 can be used to calculate the location of the upper spinodal for the isotropic-to-nematic transition. To this end, in the absence of shear flow, the initially isotropic state is slightly aligned, after which the decay or growth of the perturbation is analyzed. The concentration where the (meta-)stable isotropic state becomes unstable on increasing the concentration defines the spinodal. Hence, we substitute $\mathbf{S}(t) = \mathbf{I}/3 + \boldsymbol{\delta S}(t)$ into equation 2.59 and linearize with respect to the perturbation $\delta S(t)$, which leads to

$$\frac{d\mathbf{S}}{dt} = -6D_r^{\text{coll}} \boldsymbol{\delta S} \quad , \tag{2.61}$$

where the collective rotational diffusion coefficient is given by

$$D_r^{\text{coll}} = D_r^0 \left(1 - \frac{1}{5}\frac{L}{d}\varphi \right) \quad , \tag{2.62}$$

The spinodal concentration is thus equal to $\varphi_{IN} = 5\,(d/L)$. The prediction by Onsager is $\varphi_{IN} = 4\,(d/L)$ [41]. The difference between the two results is due to the Ginzburg-Landau expansion 2.56 leading to the Maier-Saupe potential in equation 2.57. In a more exact expansion in equation 2.56, with respect to orthogonal polyadic products, the correct factor 4, instead of 5, would have been

found, in agreement with Onsager's prediction. The solution to equation 2.61 reads

$$\boldsymbol{\delta S}(t) = \boldsymbol{\delta S}(0) \exp\{-6D_r^{\text{coll}} t\} \quad . \tag{2.63}$$

Deep into the semidilute regime and thus sufficiently close to the isotropic-nematic spinodal point, the shear dependence of the viscosity is dominated by the critical slowing down of the collective rotational diffusion and does not depend on just the rotational self-diffusion of a single rod, but rather on the collective rotational diffusion coefficient, see figure 2.1. Therefore, the competition between shear flow and Brownian motion needs to be described by an effective Peclet number $Pe^{\text{eff}} = \dot{\gamma}/D_r^{\text{coll}}$.

2.7 Geometrical constraints for the rotational diffusion coefficient

As mentioned before, when it would be possible to derive an accurate expression for the pair correlation function in equation 2.53 for the torque, the equation of motion 2.59 would include topological constraints as well as the shear-rate dependence of the probability density function ψ for the orientation of a rod. The derivation of an accurate expression for the pair correlation function is not feasible analytically.

Multi-particle interactions become important in the semidilute concentration regime $\varphi^* \leq \varphi < \varphi_{IN}$, where $\varphi^* \sim 1/L^3$ is the overlap volume fraction of rods and $(L/d)\varphi_{IN} = 4$ is the isotropic-nematic (I-N) spinodal point. While it can be shown that interactions of more than two particles are not necessary to describe the thermodynamics of rod-like colloidal suspensions [41], this does not hold for the rotational diffusion of a test particle [94, 95, 96, 97, 98, 99, 89, 100, 101]. For purely geometrical reasons, the rotational motion of a test rod is severely reduced compared to a free rod with a rotational diffusion coefficient of D_r^0. The FP equation for N rods, equation 2.29, is in principle capable to predict all necessary particle interactions. Since we are unable to solve it, however, we constrain the rotational diffusion. According to Doi [77, 81], the surrounding particles in the semidilute concentration regime form a tube, constraining the motion of a test rod to essentially one dimension. This is similar to the case of flexible polymers. While the motion of the test rod perpendicular to the tube is almost zero $D_\perp \approx 0$, the motion along the tube with $D_\parallel$ is unaffected. Since a test particle can leave a tube after diffusion of roughly one half-length and enter another tube, and the two tubes are very seldom parallel to each other, rotational motion still takes place. This rotational motion is described by a rotational diffusion coefficient $\overline{D}_r \ll D_r^0$.

Let us assume that the tube size is a, then the angle between two tubes can be approximated as $\alpha = a/L$. Since the rotational motion solely takes place in the manner described above, one can denote the mean square displacement (MSD) as

$$\left\langle (\mathbf{u}(t) - \mathbf{u}(0))^2 \right\rangle = \alpha^2 \frac{t}{\tau_r} \quad , \tag{2.64}$$

where τ_r is the rotational relaxation time. Since the Einstein expression [102] for the MSD reads

$$\left\langle (\mathbf{u}(t) - \mathbf{u}(0))^2 \right\rangle = D_r t \quad , \tag{2.65}$$

and the relaxation time of rods must be proportional to the parallel self diffusion $\tau_r \sim L^2/D_r^0$, the combination of equations 2.64 and 2.65 gives a first expression for the actual rotational diffusion in semidilute suspensions

$$D_r \sim D_r^0 \left(\frac{a}{L}\right)^2 \quad . \tag{2.66}$$

In order to approximate the tube size, one estimates the number of neighboring particles $N(R_t)$, penetrating the tube. By definition, at least one particle penetrates the tube for full tube radius $N(R_t) = 1$ at $R_t = a$. Consider a small region of the tube surface area δA with a surface normal vector $\mathbf{s}$. If the neighboring tube is oriented in direction $\mathbf{u}'$ with a probability density $\psi(\mathbf{u}')$, it intersects δA, if the center of mass of both rods is located in the volume $L\delta A|u' \cdot s|$ and, thus, the number of penetrating rods can be given as

$$N(R_t) = \nu L \delta A \oint d\mathbf{u}' \psi(\mathbf{u}') |\mathbf{u}' \cdot \mathbf{s}| \quad . \tag{2.67}$$

One can approximate $|\mathbf{u}' \cdot \mathbf{s}| = |\mathbf{u} \times \mathbf{u}'||\sin\theta|$, where θ is the angle between $\mathbf{s}$ and $\mathbf{u} \times \mathbf{u}'$. Upon integration, one arrives at a number

$$N(R_t) = \frac{\nu A L}{\pi} \oint d\mathbf{u}' \psi(\mathbf{u}') |\mathbf{u} \times \mathbf{u}'| \quad . \tag{2.68}$$

Since $A = 2\pi R_t L$, a comparison with the boundary value gives the tube radius

$$a \sim \frac{1}{\nu L^2} \left(\oint d\mathbf{u}' \psi(\mathbf{u}') |\mathbf{u} \times \mathbf{u}'| \right)^{-1} \quad . \tag{2.69}$$

By assuming a random positioning of neighboring rods, such as it should always be the case below φ_{IN}, one arrives at the following description for this reduced rotational diffusivity

$$\overline{D}_r = c D_r^0 (\nu L^3)^{-2} \quad , \tag{2.70}$$

where c is a coefficient on the order of 10^3 [87, 2]. This, however, is only valid if the surrounding of our test rod is isotropic. In the anisotropic case, so under

an external field, the rotational diffusion depends on the average orientation of the surrounding rods [98], such as in polymers [103], s.t.

$$D_r = cD_r^0 \left[\nu L^3 \frac{4}{\pi} \int d\mathbf{u}' |\mathbf{u} \times \mathbf{u}'| \psi(\mathbf{u}'; t) \right]^{-2} \quad . \tag{2.71}$$

Using the Ginzburg-Landau expansion from equation 2.56 and averaging equation 2.71, the following mean rotational diffusion coefficient can be derived

$$\langle D_r \rangle = cD_r^0 \left[\frac{5}{4} \nu L^3 \left(1 - \frac{3}{5} \mathbf{S} : \mathbf{S} \right) \right]^{-2} \quad . \tag{2.72}$$

This allows for a revised Fokker-Planck equation, including caging and tube dilation in the rod diffusivity

$$\partial_t \psi = \langle D_r \rangle \boldsymbol{\mathcal{R}} \cdot \left[\boldsymbol{\mathcal{R}} \psi - \beta \psi \overline{\mathbf{T}} \right] - \boldsymbol{\mathcal{R}} \cdot \left[\psi \mathbf{u} \times (\boldsymbol{\Gamma} \cdot \mathbf{u}) \right] \quad . \tag{2.73}$$

This change in the prefactor of equation 2.31 leads to another expression for the elastic stress tensor,

$$\boldsymbol{\Sigma}^{(e)} = \frac{\nu k_B T}{10 \langle D_r \rangle} \mathbf{E} \quad , \tag{2.74}$$

while the viscous part of the stress tensor is less affected by concentration, given full hydrodynamic screening [87],

$$\boldsymbol{\Sigma}^{(v)} = \frac{\nu k_B T}{60 D_r^0} \mathbf{E} \quad . \tag{2.75}$$

Hence, the zero shear viscosity for interacting rods can be written as:

$$\eta_0 = \eta_s \left[1 + \frac{\pi}{90 \ln(L/d)} \nu L^3 + \frac{\pi}{30 c \ln(L/d)} \left(\nu L^3 \right)^3 \right] \quad . \tag{2.76}$$

2.8 Shear-rate-dependent pair correlation function

Since the simple approximation $g = \exp\{-\beta \mathcal{V}\}$ for the pair correlation function completely neglects the topological constraints at high rod-concentration which are now accounted for in the reduced rotational diffusion coefficient, one may still use this approximation to evaluate the torque in equation 2.53. This approximation accounts for interactions between rods in the dilute regime. Since this approximation is valid for systems in equilibrium, there may be contributions that depend on the shear-rate. Since in the integral for the effective torque in equation 2.53 only distances which are within the range of the pair-potential contribute, one needs the consider the distortion of the

pair correlation function by shear only for such short distances. Since the bare Peclet number is very much smaller than the reduced Peclet number (involving the reduced rotational diffusion coefficient) in the semi-dilute regime, a linear expansion with respect to the bare Peclet number is appropriate

$$g(\mathbf{R},\mathbf{u},\mathbf{u}';t) \approx g^{(0)}\left[1 + Pe\; g^{(1)}(\mathbf{R},\mathbf{u},\mathbf{u}';t)\right] \quad , \tag{2.77}$$

where $g^{(0)} = \exp\{-\beta\,\mathcal{V}\}$, and $g^{(1)}$ is an as yet to be determined correlation function. The effective torque in equation 2.53 can be written as

$$\overline{\mathbf{T}} \approx \overline{\mathbf{T}}^{(0)} + Pe\;\overline{\mathbf{T}}^{(1)} \quad , \tag{2.78}$$

where the first contribution has been calculated above. For the additional torque, we need to solve the following integral

$$\overline{\mathbf{T}}^{(1)}(\mathbf{u};t) = -\nu \int d\mathbf{R} \oint d\mathbf{u}'\psi(\mathbf{u}';t)g^{(0)}g^{(1)}\boldsymbol{\mathcal{R}}V \quad , \tag{2.79}$$

which requires full knowledge of $g^{(1)}$. In the next subsection, we evaluate this torque, where, however, quite strong approximations have to be made.

2.8.1 The road to a non-equilibrium pair correlation function

An equation of motion for the pair correlation function can be found by integration of the N-particle Fokker-Planck equation, equation 2.29, with respect to all positions and orientations except those for two rods. This equation is amenable to analytical progress only with quite gross approximations.

The first approximation is to neglect contributions from the three-particle probability density function, which contributes at higher concentrations. This leads to

$$\begin{aligned}\partial_t P_2(\mathbf{R},\mathbf{u},\mathbf{u}';t) = \sum_{i=1}^{2}\{&\nabla_i\cdot\hat{\boldsymbol{D}}(\mathbf{u}_i)\cdot[\nabla_i P_2 + \beta P_2\nabla_i V] \\ &-\nabla_i\cdot[P_2\boldsymbol{\Gamma}\cdot\mathbf{r}_i] \\ &+D_r\boldsymbol{\mathcal{R}}_i\cdot[\boldsymbol{\mathcal{R}}_i P_2 + \beta P_2\boldsymbol{\mathcal{R}}_i V] \\ &-\boldsymbol{\mathcal{R}}_i\cdot[P_2\mathbf{u}_i\times(\boldsymbol{\Gamma}\cdot\mathbf{u}_i)]\} \quad ,\end{aligned} \tag{2.80}$$

where P_2 is the two-particle probability density function. The pair correlation function is defined as

$$P_2 = P_1(\mathbf{R},\mathbf{u};t)P_1(\mathbf{R},\mathbf{u}';t)g(\mathbf{R},\mathbf{u},\mathbf{u}';t) \quad , \tag{2.81}$$

where P_1 is the single-particle probability density function, which was denoted as ψ before. Furthermore, $\hat{\boldsymbol{D}}(\mathbf{u}) = D_{\parallel}\mathbf{uu} + D_{\perp}(\mathbf{I} - \mathbf{uu})$ is the translational diffusion tensor.

The second approximation is to neglect the dependence of the P_1's on the orientations, that is, $P_1(\mathbf{R}, \mathbf{u}'; t) = P_1(\mathbf{R}, \mathbf{u}; t) = \nu/4\pi N$, where, as before, ν is the number density of rods. Hence,

$$P_2 = \left(\frac{\nu}{4\pi N}\right)^2 g^{(0)} \left[1 + \mathrm{Pe} g^{(1)}(\mathbf{R}, \mathbf{u}, \mathbf{u}'; t)\right] \quad . \tag{2.82}$$

This leads to the following equation of motion for the pair correlation function

$$\begin{aligned} \partial_t g(\mathbf{R}, \mathbf{u}, \mathbf{u}'; t) = \sum_{i=1}^{2} \{ & \nabla_i \cdot \hat{\boldsymbol{D}}(\mathbf{u}_i) \cdot [\nabla_i g + \beta g \nabla_i V] \\ & -\nabla_i \cdot [g\boldsymbol{\Gamma} \cdot \mathbf{r}_i] \\ & +D_r \boldsymbol{\mathcal{R}}_i \cdot [\boldsymbol{\mathcal{R}}_i g + \beta g \boldsymbol{\mathcal{R}}_i V] \\ & -\boldsymbol{\mathcal{R}}_i \cdot [g\mathbf{u}_i \times (\boldsymbol{\Gamma} \cdot \mathbf{u}_i)] \} \quad . \end{aligned} \tag{2.83}$$

Thirdly, since the relaxation of the pair correlation function for the small inter-particle separations of interest is fast, we neglect the time dependence of the pair correlation function, that is, we assume the pair correlation function to be enslaved by the externally imposed flow. Substitution of the expansion in equation 2.82, keeping zeroth and first order terms in Pe, and subsequently integrating of equation 2.83 with respect to the rod positions and one of the orientations then gives

$$\begin{aligned} \beta \frac{4\pi}{\rho} \boldsymbol{\mathcal{R}} \cdot \overline{\mathbf{T}}^{(1)} \quad &= \\ \boldsymbol{\mathcal{R}}^2 \int d\mathbf{R} \oint d\mathbf{u}' g^{(0)} g^{(1)} \quad &- \quad Pe\, \boldsymbol{\mathcal{R}} \cdot \left[\mathbf{u} \times \hat{\Gamma} \cdot \mathbf{u} \int d\mathbf{R} \oint d\mathbf{u}' g^{(0)}\right] \end{aligned} \quad , \tag{2.84}$$

where equation 2.79 has been used and where $\hat{\boldsymbol{\Gamma}} = \boldsymbol{\Gamma}/\dot{\gamma}$.

Next, we assume that the non-equilibrium pair correlation function is only a weak function of the inter-particle distance for the short distance of interest, that is

$$g^{(1)}(\mathbf{R}, \mathbf{u}, \mathbf{u}'; t) \approx g^{(1)}(\mathbf{u}, \mathbf{u}'; t) \quad \text{, for } \; R \leq R_V \; , \tag{2.85}$$

where R_V is the range of the pair-interaction potential. This can be used in equation 2.79, giving

$$\overline{\mathbf{T}}^{(1)}(\mathbf{u};t) = -\nu \oint d\mathbf{u}'\psi(\mathbf{u}';t)g^{(1)} \int d\mathbf{R}g^0 \boldsymbol{\mathcal{R}}V \quad . \tag{2.86}$$

We can expand the non-equilibrium pair correlation function in terms of dyadic products of the orientation of the test rod, which can be regarded as a Ginzburg-Landau expansion in the same spirit in which the Maier-Saupe potential is derived

$$g^{(1)} \approx C^0 + C^1 : \mathbf{uu} + C^2 \odot \mathbf{uuuu} + ... \quad , \tag{2.87}$$

where $\odot$ is the contraction with respect to four indices. To obtain the torque up to leading order in the orientational order parameter, it suffices to include only the leading term in equation 2.87. This finally leads to

$$\overline{\mathbf{T}}^{(1)}(\mathbf{u};t) = -\nu C^0 \oint d\mathbf{u}'\psi(\mathbf{u}';t) \int d\mathbf{R}g^{(0)} \boldsymbol{\mathcal{R}}V \quad . \tag{2.88}$$

The total torque is thus found, within these gross approximations, to be equal to

$$\overline{\mathbf{T}} = -2\beta^{-1}dL^2\nu(1 + Pe\, C^0)\boldsymbol{\mathcal{R}} \oint d\mathbf{u}'\psi(\mathbf{u}';t)|\mathbf{u} \times \mathbf{u}'| \quad . \tag{2.89}$$

Employing the same Ginzburg-Landau expansion as before, it is, thus, found that

$$d_t\mathbf{S} = -6\langle D_r \rangle \left[\mathbf{S} - \frac{1}{3}\mathbf{I} + \frac{L}{d}\varphi(1 + Pe\, C^0) \left(\mathbf{S}^{(4)} : \mathbf{S} - \mathbf{S} \cdot \mathbf{S} \right) \right] + \boldsymbol{\Gamma} \cdot \mathbf{S} + \mathbf{S} \cdot \boldsymbol{\Gamma}^T - 2\mathbf{S}^{(4)} : \mathbf{E} \quad , \tag{2.90}$$

where the unknown constant, C^0, serves as a free parameter in a comparison to experiments, or could be determined by computer simulations.

2.9 Non-ideal rods: Effects of particle flexibility

One major assumption is used for the derivation of all equations above: infinite bending rigidity, $L_p/d \to \infty$. If this assumption is dropped, the rod-like particles under inspection gain additional degrees of freedom [104, 87, 105]. This alternates first and foremost the diffusion coefficients, which play an important role for the stress relaxation in the suspension, as indicated by equation 2.49. If the bending rigidity of a semiflexible rod allows for one only

one bending mode along the total contour length, L, the excluded volume between particles is equivalent to that of stiff rods [106]. Here, only the effect of bending rigidity on the rotational diffusion is discussed, but it is shown in chapter 5 that this is insufficient to describe the non-equilibrium behavior of flexible rods. Assuming that the particles have enough time to diffuse according to the tube picture, the rotational diffusion coefficient, $\langle D_r \rangle$, changes [104, 107]. Given that the particle conformation is allowed to change slightly, one can introduce a linear correction term for the particle thickness in equation 2.72. It is obvious that the scaling argument is not changed for such a linear correction. The only change one would expect from such a linear correction can be placed into the prefactor c in the expression $\langle D_r \rangle = cD_r^0 \left(\cdot\right)^{-2}$(for the content inside the bracket, consult equation 2.72). The rotational relaxation time for rods, therefore, becomes $\tau_{\text{end}} = 1/\langle D_r \rangle$.

On the other hand, the particles gain more degrees of freedom especially at shorter timescales [108, 109, 110]. According to Morse theory [80, 111, 112], which is based on the worm-like chain model, scaling rules for all important diffusion coefficients can be given. At times $\tau_{\text{flex}} \ll \tau_r$ the particles can reduce the overall suspension stress by undulation with a wavelength $\sim 2L$. At even smaller timescales, stresses can relax via a smaller wavelength undulation mode with a relaxation time of τ_e. The inclusion of particle flexibility, therefore, leads to a relaxation time spectrum (RTS) for rod-like particles,

$$g_i(\tau_i) = \{g_{\text{end}}(\tau_{\text{end}}), g_r(\tau_r), g_{\text{flex}}(\tau_{\text{flex}}), g_e(\tau_e)\} \quad , \tag{2.91}$$

where the essentially free rotational diffusion inside the tube, $\tau_r = 1/D_r^0$, was included. In figure 2.2(b), the full relaxation time spectrum is sketched for a semidilute rod-like particle suspension. Figure 2.2(a) displays the dilute suspension case.

While the only timescale playing a role in steady state shear flow is τ_{end}, the linear viscoelasticity as well as the time resolved rotational diffusion strongly depend on the RTS. The given modification of Dhont-Briels theory, including the rotational diffusion coefficient $\langle D_r \rangle$, corrected for particle flexibility, as well as the non-equilibrium pair correlation function, can be used to describe the orientational ordering and suspension viscosity of semiflexible rods under steady shear flow.

2.10 Non-ideal rods: Effects of polydispersity

In a polydisperse environment, both the diffusion coefficients of rods as well as the particle-particle interactions change [113, 114, 105]. This complicates the

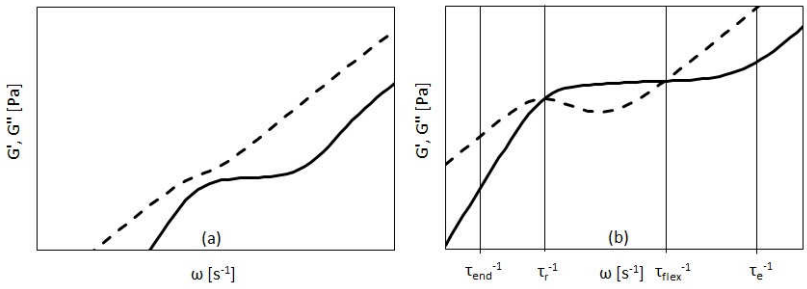

Figure 2.2: Dynamic moduli vs. frequency predicted by Morse theory in (a) the dilute and (b) the semidilute concentration regime.

solution of Dhont-Briels theory. However, one can assume for simplicity that the single particle behavior remains unchanged and still obeys Dhont-Briels theory in the given form and that the tube constructed by two different species is the roughly the same as that of two identical species. This assumption does not agree with the scaling of the tube size, $D_{\text{tube}} \sim L^2$, which shows a strong length dependence. If we consider that the motion of all rods is confined according to the tube picture, however, we can assume that the mean particle length in the mixture is the deciding quantity affecting the particle motility, as $\overline{D}_r \sim L^{-9}$. We regard bidisperse species with a small length bidispersity, $L^{(1)} \neq L^{(2)}$, described by the following linear mixing rule:

$$\varphi^{(m)} = \varphi^{(1)}(1-\rho) + \varphi^{(2)}\rho \quad , \tag{2.92}$$

where the relative volume fraction is called ρ. Using the definition of the volume fraction, $\varphi = (\pi/4)d^2L\nu$, we can easily prove that the same mixing rule holds for the lengths,

$$L^{(m)} = L^{(1)}(1-\rho) + L^{(2)}\rho, \tag{2.93}$$

given that the number density, $\nu = N/V$, is independent of polydispersity. Combining these mixing rules with equation 2.90, leads to a first simple description of the rheology and orientational ordering of a bidisperse, semidilute rod suspension. As an example, one can write down the zero shear viscosity,

$$\eta_0 = \eta_s \left[1 + \frac{\pi}{90\ln(L^{(m)}/d)}\nu(L^{(m)})^3 + \frac{\pi}{30c\ln(L^{(m)}/d)}\left(\nu(L^{(m)})^3\right)^3\right] \quad , \tag{2.94}$$

where the viscous stress tensor, with $\mathcal{V} = 0$, was taken into account. No simple expression for the the nonlinear viscosity can be obtained, but a solution of equation 2.90 with an incorporated linear mixing rule is unproblematic.

A mixing rule for a completely polydisperse sample can be structured in the same fashion, but it remains questionable if the given approach is sensible if very small and very long rods are present in the mixture, since for example, very small rods could act as a complex solvent for very long rods or phase separation between rods of different lengths could occur. In such cases, a full theoretical description like that of Marrucci and Grizzuti [113] needs to be considered.

Chapter 3

Experimental

3.1 Materials

In this thesis, rod-like bacteriophages of the lambda-class are used as a model system. In particular, these are fd wild-type, fdY21M, M13k07, M13-mini, and Pf1 wild-type virus. Since all phages of this class have the same thickness of 6.6 nm, a polyethylene glycol coating is applied to vary this geometrical parameter. The species themselves span a range of 0.33-1.96 μm in contour length with M13-mini the shortest and Pf1 the longest rod, and a range of 0.88-9.9 μm in persistence length, see table 3.1. To test for the effect of particle stiffness, we consider fd wild type and fdY21M, as the bending rigidity [115], $L_p k_B T$, of those systems is different, while their contour length is almost identical. For the other species, we need to keep in mind that L/L_p increases linearly with the contour length, which causes a decrease of the correlations between the rod ends and possibly allows the particles to bend considerably if $L \geq L_P$.

All viruses were grown inside their host-bacteria in Luria-Bertani broth [116, 117], following standard biological protocols [118]. The surface of all viruses consists of helically ordered proteins covering the core DNA. FdY21M virus is a stiff mutant of wild-type fd virus, where the 21st amino group of the capsid protein (g8p) was changed from tyrosine (Y) to methionine (M) [57]. M13k07 as well as M13-mini are derivatives of the M13 wild-type bacteriophage. In the case of M13k07, the genus of reproduction in the DNA was alternated using the reproductive genome section of another helper page (P15A) as well as a kanamycin resistance [119]. The genome change results in a higher effective particle length compared

to fd wild-type virus. M13-mini is produced by replacing the respective region of the genome with another helper-phage plasmid (pSB4434) and additional kanamycin and chloramphenicol resistance [120]. Despite the longer genome, the change in DNA causes the phage to encode for a virus roughly a third the size of fd wild-type. All of these phages grow in the XL-1 blue strain of E.-coli, except for Pf1 virus, which is a Pseudomonas Aeruginosa phage.

Roughly 90 mg of virus can be harvested from 6 l infected Luria-Bertani broth. After growth to saturation, the virus particles were cleaned from the remainders of their host bacteria by multiple centrifugation steps at $3x10^4$ g for 2 h and subsequent ultra-centrifugation at $1x10^5$ g for 12 h. In the case of M13-mini, the resulting virus pellet held a significant amount of spherically collapsed particles, see figure 3.1. The spherical content can be compared to the collapsed coat proteins reported by Griffith et al. [121]. Most certainly, the collapsed virus coat protein emerges after expelling of the core DNA, see figure 3.2, where an assembly of core DNA together with the collapsed coat protein could be detected by AFM. In order to purify the rod-like species alone, suspensions in pure deionized water were prepared at a concentration deep in the nematic state. The phase separation of spheres and rods took on average 36 h, after which the pure rod-like phase could be separated.

After the final purification step, all species were suspended in water with 20 mM/l Trizma base to create a colloidal suspension with high stability over long timescales. The viruses have negative surface net-charge in a pH neutral environment which leads to this colloidal stability. To achieve pH neutrality, the necessary amount of concentrated HCl was added to the suspension. Since the Trizma base ions are weakly bound to the virus surface at an ionic strength of 10 mM resulting from the use of Trizma base alone, their interaction can be lowered, thus assuring a hard-core interaction potential. This is achieved by adding 90 mM/l sodium chloride, giving an ionic strength of 100 mM at pH 8.3.

After purification by ultra-centrifugation, a fraction of fdY21M was suspended in phosphate buffer and coated with end functionalized monodisperse 8 kDA Polyethylen Glycol (PEG) in a grafting-to procedure based on click chemistry [122]. The functionalized material was carefully cleansed from buffer and PEG residuals by repeated centrifugation and re-dispersion. Additionally, a fraction of fdY21M was suspended in 20 mM/l Trizma buffer with only 10 mM/l of salt. Both, the PEG coated virus in 100 mM buffer, as well as the bare fdY21M suspended in 20 mM buffer should possess the same effective particle thickness [70] of roughly 17 nm, see table 3.1.

To allow for an investigation of the systems using SANS, the water of all suspensions was fully replaced by Deuterium Dioxide. Additionally, fd wild-type virus as well as fdY21M were suspended in a mixture of glycerol and 100 mM

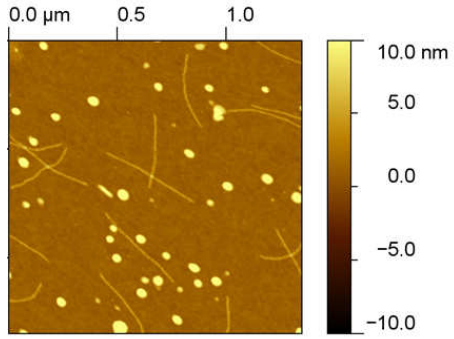

Figure 3.1: AFM image of M13-mini ($L = 0.33$ μm, $L_p = 2.8$ μm) on polyallylamine. The scale bar on the right shows the detected object thickness.

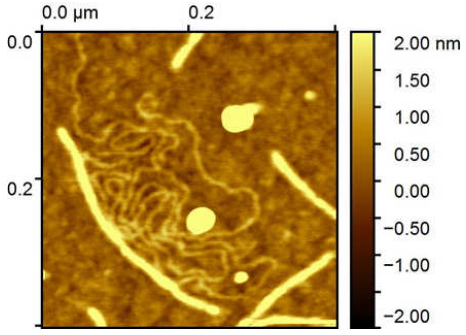

Figure 3.2: AFM image of expelled core DNA of M13-mini plus collapsed coat protein on polyallylamine, the scale bar on the right shows the detected object thickness.

Trizma buffer (Merck KGaA, Darmstadt, Germany). This was achieved by dispersing the pelleted viruses after ultra-centrifugation in a small amount of Trizma buffer resulting in a highly viscous slurry. Under continuous shaking, pure glycerol (Merck KGaA, Darmstadt, Germany) was added to this slurry until a concentration of 86.03 m% for the fd wild-type medium and 86.01 m% for the fdY21M medium was reached. The glycerol to Trizma buffer ratio was chosen to minimize the uptake of air humidity.

For the measurement of suspension concentration, a UV-Vis spectrophotometer,

Table 3.1: Materials

material	**length** μm	L_p [70] μm	**ionic strength** mM	$d_{\mathbf{eff}}$ [24] nm
fd	0.88	2.8±0.7	100	10.5
fdY21M	0.91	9.9±1.6	100	10.5
			10	17
fdY21M peg			100	17
M13k07	1.2	2.8±0.7	100	10.5
M13-mini	0.33	2.8±0.7	100	10.5
Pf1	2.1	2.8±0.7	100	10.5

Varian Cary 50 (Agilent, California, USA), was used. After subtraction of the sample background induced by the Trizma buffer, absorption spectra were measured between wavelengths of 240-300 nm where the virus coat protein characteristic is located. The absorption spectrum has a local minimum at 244 nm and a local maximum at 269 nm. In the case of a pure sample, the ratio between peak value and minimum value should be 1.04. For calculation of the suspension concentration, only the peak value is of interest. Using the absorption coefficients, listed in table 3.2, the concentrations can be calculated.

All colloidal suspensions were prepared at the isotropic binodal point, φ_I, and subsequently diluted to concentrations of roughly 75, 50, 25 and 10% of φ_I.

Isotropic binodal points, φ_I, are estimated for all systems by birefringence studies. The virus systems in 100 mM ionic strength buffers are concentrated such that the suspensions are nematic. Then, the suspensions are carefully diluted into the biphasic gap. We wait until phase separation is complete, using glass capillaries of 20 mm diameter, placed between crossed polarizers. Phase separation results in a liquid with a certain nematic and a certain isotropic fraction. We subsequently collect the isotropic fraction and determine its concentration. In table 3.2, the resulting scaled isotropic binodal points are listed.

Atomic force microscopy (AFM) was performed using an Agilent 5500 system (Keysight Technologies, Santa Rosa, USA) equipped with MSNL-F cantilevers (f=125-160 kHz, k=0.6-1.4 N/m; Bruker, Camarillo, USA) with an average tip radius of 2-12 nm. Samples were prepared by applying 400 μl of 1000-fold diluted virus suspensions to 1x1 cm SiO_2 plates, coated with polyallylamin, comparable with the stamp preparation procedure reported by van Grinsven et al. [124]. After a 10 min settling time, the excess fluid is largely removed by the dry room air. The surface coating, thereby, provides a small contact angle between liquid and probe surface, such that no flow gradient is induced by the

Table 3.2: Virus coat protein absorption coefficients and estimated scaled isotropic binodal points.

virus	**absorption coefficient** ml/mg cm	$L\varphi_I/d_{\text{eff}}$
fd	3.84 [70]	4.61
fdY21M	3.63 [70]	3.4
fdY21M peg	3.63	4.63
M13k07	3.84	5.62
M13-mini	3.84	3.7
Pf1	2.25 [123]	8.37

drying procedure. This is different from the drying procedure on aminosilane coatings, showing a slightly higher hydrophobicity compared to polyallylamine. Samples can be subsequently scanned for a few times, before the virus coating protein is falling apart.

3.2 Measurements and Methods

3.2.1 Rheology

Rheological measurements of steady and start-up shear flow were carried out in a strain controlled ARES-LS rheometer (TA Instruments, New Castle, USA) equipped with a Couette cell of 1 mm gap size and 34 mm outer diameter. All measurements were carried out at 22^oC. The measurement range was chosen from 0.0001-1000 s^{-1} for all samples. Depending on the sample, the lowest measurable shear-rate was adjusted according to the lower torque limit of the device. In case of steady shear measurements, also transient shear stress curves were measured, see figure 3.3. The steady state stress was evaluated from the final plateau values of the stress, Σ_{steady}, which was typically reached after 2-4 strain units, depending on the sample.

Small amplitude oscillatory shear (SAOS) measurements are difficult to perform for water based virus suspensions due to the low torque these systems induce in the quasi-linear response regime. Therefore, all reported data were obtained for glycerol/Trizma buffer mixtures. The enhanced torque due to this suspending medium allows for the use of a different sample environment. All SAOS measurements were carried out in the strain controlled ARES LS rheometer equipped with a 25 mm diameter cone-plate geometry with 1^o cone angle. The cone-plate geometry was equipped with a solvent trap to prevent evaporation.

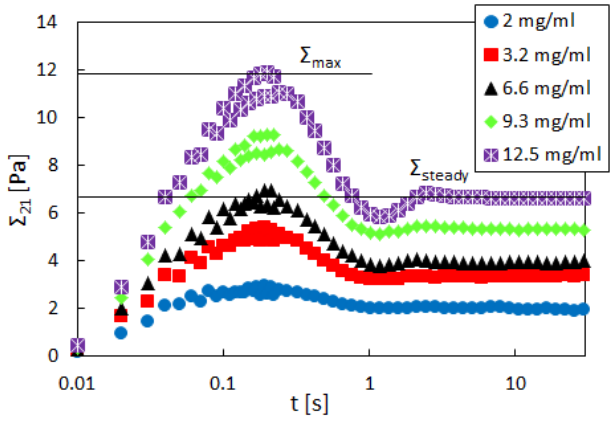

Figure 3.3: Stress at a shear-rate of 10 s^{-1} as a function of time for fdY21M virus ($L = 0.92$ μm, $L_p = 9.9$ μm) in a glycerol based buffer at different concentrations. The two horizontal lines mark the overshoot and steady stress values.

The measurement temperature was 22^{o}C. Pre-shear at a shear-rate of 100 s^{-1} was applied for 5 min to erase any possible effects from sample loading. The sample rested for 100 min after this procedure to assure equilibration. Strain amplitude sweeps were carried out at 1 rad/s ranging from 0.05-200% strain. From this window, it was always possible to deduce the linear response regime as well as the lower torque limit at the given frequency. The usual strain amplitude chosen for frequency sweeps was 10% and the frequency range was 0.0001-100 rad/s. Usually, the torque limit of frequency sweeps was reached at around 0.01 rad/s, depending on the sample concentration.

Uniaxial extensional rheometry was performed in a HAAKE CaBER-1 extensional rheometer (Thermo Haake GmbH, Karlsruhe, Germany). The drive unit of the device was used to control the position and separation velocity. Two circular plates with a diameter of 4 mm were used. For the diameter evolution under extensional flow, a high speed camera was used (Photron Fastcam SA-2, Photron, San Diego USA). The measurement temperature was set to 22^{o}C via the room temperature control circuit. The fluid drop was extended rapidly by applying a sudden change in plate separation from initially 2 mm to a value of 6 mm. The minimum filament radius $R_{\min}$ initially evolves over time according to:

$$R_{\min}(t) = R_1 - \frac{\sigma(2X-1)}{6\eta_e}t \quad , \tag{3.1}$$

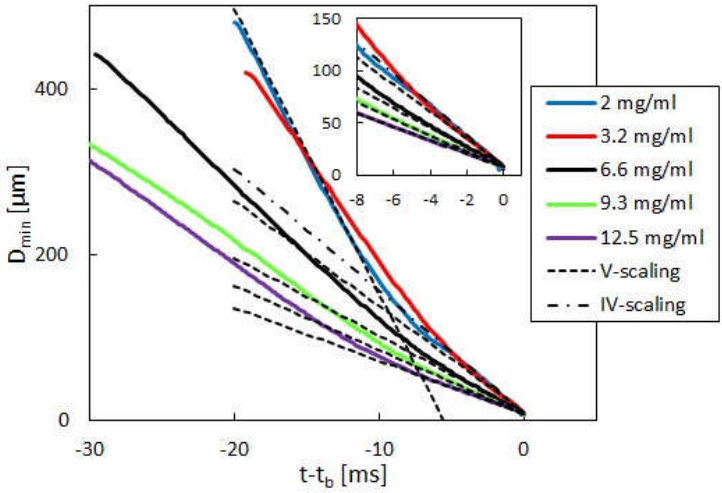

Figure 3.4: Filament diameter versus time before the time of filament rupture, $t_b = 0$, for different concentrations of fdY21M ($L = 0.92$ μm, $L_p = 9.9$ μm) in glycerol/Trizma buffer. Dotted lines are scaled with $X = 0.7127$ (V-scaling), dash-dotted lines with $X = 0.5912$ (IV-scaling). The inset shows the end of filament lifetime.

where $\sigma = 63$ mN/m was the surface tension of all suspensions independent of the virus content, measured by the pendant drop method, $X = 0.7127$ is a correction factor due to slight derivations of the filament geometry from ideal cylindrical shape [125, 126], and R_1 is the initial radius. At the end of the filament lifetime, the correction factor changes to a value of $X = 0.5912$ [127, 128]. Only in the case of the lowest measured concentration, the second scaling factor had to be used, see figure 3.4.

In figure 3.4, the filament diameter is plotted against the relative measurement time, before the time of filament breakup, t_b. The extension rate is

$$\dot{\epsilon} = \frac{2}{D}\frac{dD_{\min}}{dt} \quad , \tag{3.2}$$

with the current filament diameter D.

3.2.2 Rheo-SANS

Rheo-SANS measurements were performed at the SINQ spallation source at the Paul Scherrer Institute in Villigen, Switzerland, the Institute Laue-Langevin

in Grenoble, France, as well as the Heinz-Maier Leibnitz Zentrum in Garching, Germany. An Anton Paar MCR 501 rheometer (Anton Paar, Graz, Austra) was mounted in the beam-lines SANS-1 in Villigen and KWS-2 in Garching. Both measurement geometries were composed of a quartz glass Couette cell with the same geometry as the Couette cell used in the ARES-LS as well as an inner quartz glass cylinder. Since the MCR 501 is a stress controlled rheometer, all measurements were repeated for control purposes using the ARES-LS rheometer. The incident beam probes the sample geometry in the flow-vorticity plane during simultaneous recording of the stress signal. In Grenoble, the flow-gradient plane could be probed by placing a shear cell [1] into the D22 large dynamic range small angle diffractometer. As the shear cell was equipped with a state-of-the-art gearbox transducer and a brush-less ec-motor for continuous movement, it was feasible to measure at extremely low shear-rates in this geometry, $\dot{\gamma} = 10^{-5}$ s.

All rheo-SANS measurements were performed at 22^oC with a detector distance of 6 m and a thermal wavelength of the neutrons of 1.3±0.1 nm, except for gap scans, where the neutron wavelength was adjusted to 0.6±0.08 nm. A detector distance of 3 m was also used in order to measure the thickness of the rods. The aperture size in Garching and Villigen was 2.5x2.5 cm. In Grenoble, an aperture size of 1.5x0.9 cm was used and switched to a size of 1.5x0.3 cm in the case of gap scans in the vorticity direction. A scattering vector range from 3.2x10^{-2}-4.6x10^{-2} $Å^{-1}$ was used for the intensity calculations along the azimuthal angle. In figure 3.5, the evaluation of azimuthal intensity profiles, used for further analysis, is plotted for two chosen q-ranges. Since no difference between the two q-ranges (I) and (II) could be found for any measurement, we chose to evaluate the indicated range (II) since it was less prone to intensity fluctuations very close to the edges of the beam-stop than the lower q-range (I).

The inset of figure 3.5 displays two exemplary intensity profiles $I(\theta)$ as a function of the azimuthal angle θ which describes the flow-vorticity plane of orientational ordering of rods in a Couette cell geometry. Similar to this, intensity profiles $I(\phi)$ can be plotted as a function of the planar angle ϕ describing the flow-gradient plane. Assuming that the two intensity distributions are equivalent to the orientational distribution functions $\psi(\alpha)$, where α stands for either the azimuthal or the planar angle, one can deduce the full orientational ordering tensor $\mathbf{S}$ during flow by combination of the two measurements with incident beams in either the gradient or the vorticity direction of the cell.

Under the assumption of a Maier-Saupe [129] orientational distribution, one can describe these intensity profiles using second order Legendre polynomials $P_2(\alpha - \alpha_{\max}) = (3\cos(\alpha - \alpha_{\max})^2 - 1)/2$:

$$\psi(\alpha) = I_0 \exp[KP_2(\alpha - \alpha_{\max}) - 1] \quad , \tag{3.3}$$

[1] doi: 10.5291/ILL-DATA.9-10-1475

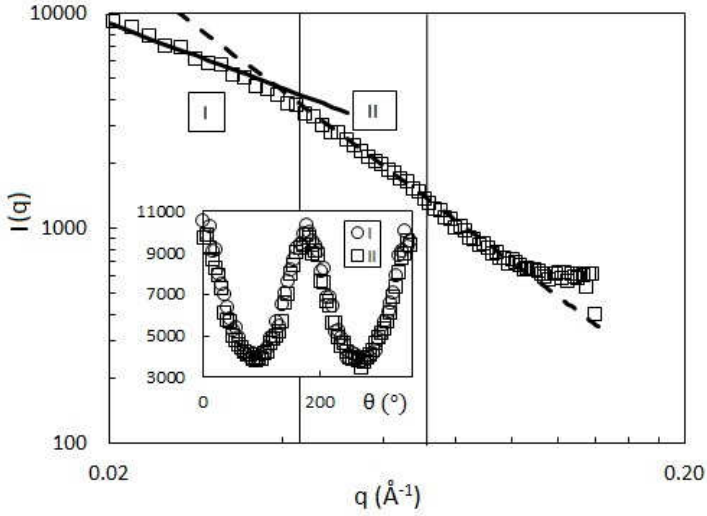

Figure 3.5: Intensity versus scattering angle for fd wild-type virus ($L = 0.88$ μm, $L_p = 2.8$ μm) at a concentration of 15 mg/ml in Deuterium Dioxide with an ionic strength of 100 mM. The full line indicates q^{-1} dependence and the dashed line q^{-2}. The inset shows the azimuthal intensity profiles evaluated in the two indicated zones (I) and (II) of the scattering vector.

where $\alpha_{\max}$ is the angle between the director and the direction of fluid flow, I_0 is the intensity amplitude and K describes the width of the intensity profile [130]. Earlier studies employing these assumptions have proven that the orientational distribution is well described by this function [131, 32]. The average order parameter, $\langle P_2(\alpha)\rangle$, can be calculated by fitting the measured intensity profiles with the given functions, and taking the average of $P_2(\alpha)$ over the thus obtained distribution function:

$$\langle P_2(\alpha)\rangle = \frac{\int_0^1 d\cos(\alpha)\psi(\alpha)P_2(\alpha - \alpha_{\max})}{\int_0^1 d\cos(\alpha)\psi(\alpha)} \quad . \tag{3.4}$$

The order parameters in the flow-gradient and flow-vorticity plane are directly proportional to the largest eigenvalue of $\mathbf{S}$, λ_1, projected into the respective planes $\langle P_2(\alpha)\rangle = (3\lambda_1(\alpha) - 1)/2$. The traceless orientational ordering tensor, $\mathbf{Q} = (3\mathbf{S} - \mathbf{I})$, needs to be defined in order to perform a transition from the reference frame of the measurement to the frame of flow. By using a rotation

matrix:

$$\mathbf{R}^{(0,\theta)} = \begin{pmatrix} \cos\theta & \sin\theta & 0 \\ -\sin\theta & \cos\theta & 0 \\ 0 & 0 & 1 \end{pmatrix} \quad , \tag{3.5}$$

the relation between the two tensors can be rewritten as

$$\mathbf{S} = \left(\mathbf{R}^{(0,\theta)}\right)^T \tilde{\boldsymbol{Q}} \mathbf{R}^{(0,\theta)} \quad , \tag{3.6}$$

where the orientational ordering tensor in the laboratory reference frame is $\tilde{\boldsymbol{Q}} = (2\mathbf{Q} + \mathbf{I})/3$. From the measurements, we can deduce that $\phi_{\max} = 0$ at all times, giving us the opportunity to define the tensor $\mathbf{Q}$:

$$\begin{aligned} Q_{33} &= \lambda_1(\theta) \quad , \\ Q_{22} &= \mathcal{T} - \frac{1}{2}\lambda_1(\theta) \quad , \\ Q_{11} &= -\mathcal{T} - \frac{1}{2}\lambda_1(\theta) \quad . \end{aligned} \tag{3.7}$$

Here, $\mathcal{T}$ quantifies the biaxiality of the distribution, defined as

$$\mathcal{T} = \frac{1}{2(2 - \lambda_1(\theta) - \lambda_1(\phi))} \left[\lambda_1(\theta)\lambda_1(\phi) - \lambda_1^2(\theta)\right] \quad . \tag{3.8}$$

Throughout the thesis, the order parameter in flow-vorticity direction,$\langle P_2 \rangle(\theta)$, is shown, if not indicated otherwise.

3.2.3 Flow profiling

Flow-heterodyne dynamic light scattering (flow-HDLS) was performed using the setup available at the Institute of Complex Systems-3 in Forschungszentrum Jülich, Jülich, Germany [132]. A quartz Couette-flow cell similar to the two cells described above, but with a 1.5 mm gap width and an outer cylinder diameter of 47 mm, was mounted into the split light beam of a Kr-laser (wavelength=647 nm, I=100 mW; Spectra Physics, Santa Clara, USA). A frontal lens is located on a movable platform controlled by a linear EC motor, allowing for a gap scan of the cell in gradient direction.

Flow-HDLS is characterized by two incident laser beams with scattering vectors:

$$\begin{aligned} \mathbf{q}_1 &= \mathbf{k}_1 - \mathbf{k}_f \quad , \\ \mathbf{q}_2 &= \mathbf{k}_2 - \mathbf{k}_f \quad , \end{aligned}$$

where $\mathbf{k}_1$ and $\mathbf{k}_2$ are the wave vectors of the incident beam and $\mathbf{k}_f$ is the wave vector of scattered light at the detector, see, e.g., the books by Durst [133] or Drain [134]. The Doppler shifts of these two scattering vectors are:

$$\omega_1 = \mathbf{q}_1 \cdot \mathbf{v} \quad ,$$

$$\omega_2 = \mathbf{q}_2 \cdot \mathbf{v} \quad ,$$

where $\mathbf{v}$ is the fluid velocity. The measured frequency, $\omega = \omega_1 - \omega_2$, is independent of the wave vector at the detector. This frequency is directly proportional to the Doppler frequency, t_{osc}, and thus directly proportional to the velocity:

$$t_{\mathrm{osc}} = \omega/2\pi = \frac{2n\sin(\theta_n/2)}{\lambda}|\mathbf{v}|\cos\beta \quad , \tag{3.9}$$

where θ is the angle between the wave vectors of the incident beams inside the sample volume, β the angle between $\mathbf{k}_1 - \mathbf{k}_2$ and $\mathbf{v}$, and n is the refractive index of the medium. In our case, we will assume $\cos\beta = 1$.

Within the crossover region of the two incident laser beams, the experimental intensity correlation function, $g_2(\tau)$, can be measured as a function of the lag time, τ, given exemplary by the red symbols in figure 3.6.

Over the scattering volume, the correlation function generally decreases in amplitude. The decrease is caused by the relative motion of particles in the measurement volume which can have several reasons, e.g., diffusion of particles and the velocity gradient. This decrease is not captured in equation 3.9. For the velocity measurement itself, only the oscillating component of the intensity function is of interest here since this is the only component depending on the velocity, see equation 3.9. In order to obtain a better fit to the measured correlation function, however, a more complex form can be derived [135], capturing among other things also the loss of intensity along the scattering volume:

$$g_2(\tau) = A + B\exp\left[-\frac{\tau}{t_{\mathrm{lin}}} - \left(\frac{\tau}{t_{\mathrm{sqr}}}\right)^2\right]\left\{C + \exp\left[-\frac{\tau}{t_{\mathrm{fluct}}}\right]^2\cos\left(\frac{2\pi\tau}{t_{\mathrm{osc}}}\right)\right\} \quad , \tag{3.10}$$

where t_{lin}, t_{sqr}, and t_{fluct} mark the physically motivated fitting parameters for the case of a flow situation of higher complexity (fluctuations with a lifetime of t_{fluct}, for example, arise only in turbulent flow fields), A is the baseline, B the amplitude and C the modulation. From the cosine term, the velocity of the fluid can be calculated using equation 3.9.

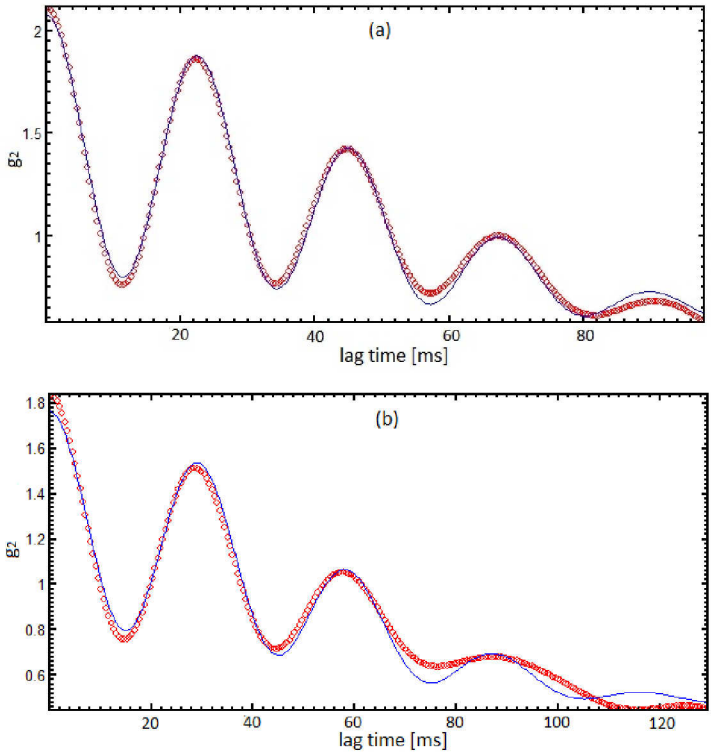

Figure 3.6: Intensity correlation function over lag time for fdY21M ($L = 0.92$ μm, $L_p = 9.9$ μm) at a concentration of 9.3 mg/ml suspended in water with an ionic strength of 100 mM, measured under continuous shear flow at $\dot{\gamma} = 10$ s^{-1}. The blue line shows the used fitting function, equation 3.10. The measurement locus is (a) the middle, (b) the outer wall of the Couette cell.

Figure 3.6 shows the fitted function from equation 3.10 (blue curve). The fitting function is in good agreement with the measured function in figure 3.6(a), except for higher lag times. Since the important aspect of the fitting function is the correct capturing of the wavelength, the velocity calculation from this exemplary curve can be regarded as correct. Since the outer cylinder of the shear cell stands still while the inner cylinder rotates, the intensity correlation function shows less oscillations at the outer wall, as shown in figure 3.6(b), thus, slightly higher errors in the velocity calculation occur. Nonetheless, except for locations very close to either wall, enough oscillations for a thorough calculation of the velocity were measured.

Chapter 4

Ideal rods

4.1 Introduction

The understanding of dilute suspensions of rods is profound, due to a long history of theoretical work [71, 75, 136, 82] accompanied by experimental investigations [137, 138] which are in good agreement. It is understood that in dilute suspensions, the rods tumble in shear flow. The observed rheological behavior of nematic liquid-crystalline suspensions [139, 140, 141, 142, 34, 143, 144, 38] is more complex, as kayaking, wagging, tumbling, and flow-alignment can occur, depending on the circumstances. Understanding this plethora of effects on a theoretical basis, however, has been accomplished in large parts [129, 87, 145, 86]. Between dilute and nematic suspensions, lies a range of concentrations we like to call semi-dilute, in the sense that the particles overlap considerably, $\varphi \gg \varphi^*$. This region is governed by comparatively simple shear thinning [146] and the theoretical understanding should be straight forward, given that both dilute and nematic suspensions are described well by the existing theory. The interaction of particles in this regime, however, is quite complex due to the caging of particles [147, 148, 114, 149] and an analytical solution of the governing Fokker-Planck equation is only feasible using strongly restricting assumptions, see chapter 2. This leads to the inevitable use of the tube model in order to make quantitative predictions of rheological constants and functions for industrially relevant systems, which are highly desirable. In this part of the thesis, we assess the need for the tube model to describe semi-dilute suspensions of ideal rods. It is shown that the tube model is needed to understand the measured zero shear viscosity, but at higher shear-rates, dilation of the tube and a shear-mediated inter-particle potential are needed to describe the behavior.

The newly developed non-equilibrium pair correlation function is tested and we find a good agreement with the measured viscosity curves but underestimate the orientational ordering.

The SAOS response of the ideal rod, reported in section 4.3.1, reveals signatures of the rotational diffusion coefficient as well as the characteristic time of particle undulation. The relatively short time of undulation, however, seems to play a negligible role for the steady state shear flow behavior, reported in section 4.3.2, which is dominated by shear thinning and concomitant orientational ordering of rods in the direction of flow. This concentration dependent behavior is sufficiently described by the critical slowing down of the collective particle dynamics towards the IN transition. In section 4.3.3, the elongational viscosity is measured. A strong increase of the Trouton ratio with increasing particle concentration is reported. Due to the strong shear thinning behavior, we finally test for shear banding in the ideal rod-like system, see section 4.4, but no shear banding transition is found.

4.2 Material

The ideal rod-like colloidal suspension is composed of fdY21M in a 100 mM Trizma base buffer solution. Due to the relatively small Debye double layer around the rods in this buffer, see for example [122], the effective thickness of the virus in suspension is ~ 10.5 nm [70]. This gives an effective aspect ratio of ~ 87. Together with its persistence length of roughly 10 times the contour length, it meets all theoretical requirements on ideality regarding morphological aspects. According to Onsager theory [41], the isotropic binodal point of the ideal rod is located at $\varphi_I = 3.29 d_{\text{eff}}/L$. FdY21M undergoes this phase transition exactly at this scaled concentration, as was shown by Barry et al. [70] and in this thesis, see table 3.2. This makes fdY21M ideally suited for rheological investigations on ideal rods and allows for a comparison to theoretical descriptions of the ideal rod behavior under flow. All investigated suspensions are as concentrated as $\varphi = 280\varphi^*$ and higher.

4.3 Linear and nonlinear rheology

4.3.1 SAOS

The concentration dependent shear flow behavior of the ideal rod, fdY21M, in the linear viscoelastic (LVE) response regime is studied using SAOS. As described in chapter 3, such a measurement is not feasible in water. Therefore, all measurements comprise fdY21M in glycerol/Trizma buffer mixtures. In such a buffer, the ionic strength is $\sim$ 10 mM, resulting in an effective thickness of 17 nm [24]. This shifts the experimentally estimated isotropic binodal from $\varphi_I \simeq 0.045$ to $\sim$0.026 and the corresponding concentrations from $\sim$16.3 mg/ml to $\sim$9.3 mg/ml. In order to stay in the dilute to semidilute concentration regime, therefore, the highest measured concentration was chosen at 9.1 mg/ml, rather close to the isotropic binodal point.

Figure 4.1 shows the storage modulus, $G'(\omega)$, and loss modulus, $G''(\omega)$, as a function of frequency for all measured concentrations inside the semidilute concentration regime. It is obvious that the viscous part of the LVE response, $G''(\omega)$, is higher than the elastic part ,$G'(\omega)$, for all accessible frequencies at lower concentrations, see figures 4.1(a), (b), and (c). At higher concentrations, shown in figures 4.1(d) and (e), the elastic contribution becomes more important, resulting in a crossing over of the two corresponding curves. Two crossover points emerge: one around a relaxation time $\tau_{\text{low}}^{-1} \simeq 0.1\ \text{s}^{-1}$ and the other at $\tau_{\text{high}}^{-1} \simeq 1\ \text{s}^{-1}$. At the highest concentration, figure 4.1(e), the lower crossover point is shifted to lower values, while the higher crossover point is shifted to higher values compared to the lower concentration, shown in figure 4.1(d). Despite these characteristics, all curves for corresponding moduli at different concentrations seem to be of similar shape, gaining in magnitude with increasing concentration.

The overall LVE response of ideal rods can be divided into three regions: a low frequency (long time) region, which is barely covered by the measurements, since the torque limit is reached already around $\omega \approx 0.01\ \text{s}^{-1}$, a mid-frequency region, and a high frequency (short time) region. In the high frequency region, the loss moduli seem to have a constant slope of 1, independent of concentration. In the mid frequency range, the curve flattens. In the low frequency domain, the curve seems to become steeper again. The slope of $G''(\omega)$ in the low frequency regime equals the zero shear viscosity of rods $\eta_0 = \lim_{\dot{\gamma}\to 0} G''(\omega)/\omega$. Since the regime cannot be identified clearly, the zero shear viscosity is not measurable for the system comprised of the glycerol/Trizma buffer.

These curve characteristics can be interpreted, in the framework of the theory of Morse [80, 111, 112]. The thin lines in figure 4.1 show results for the complex

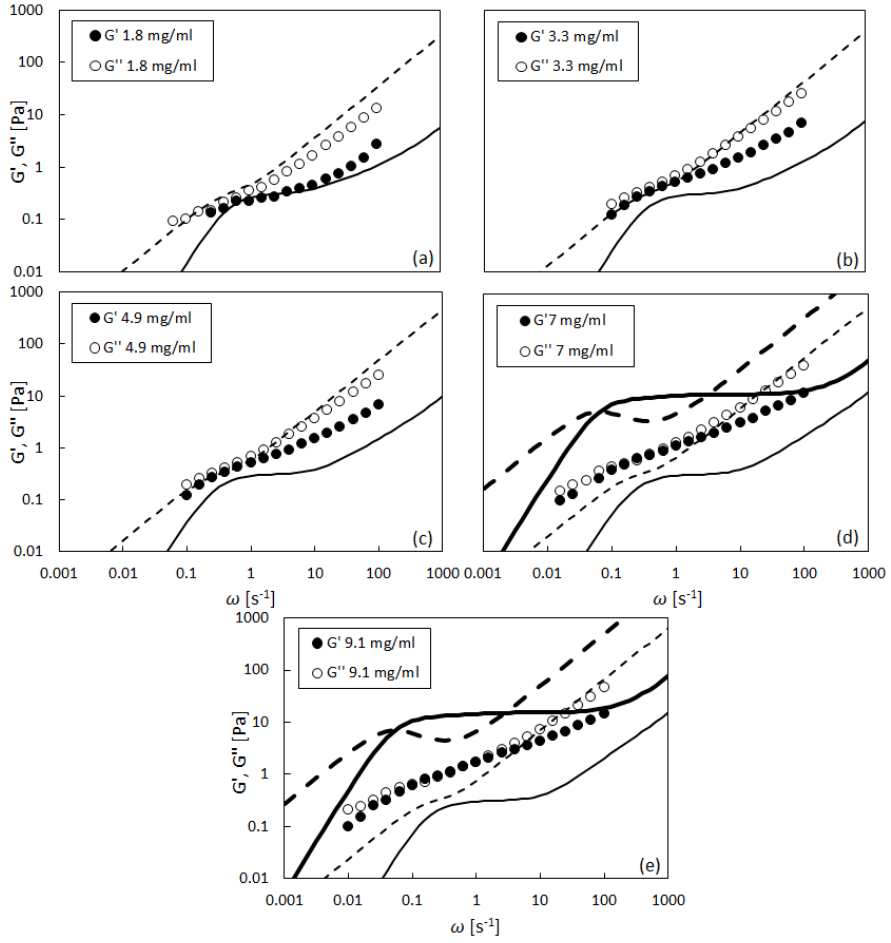

Figure 4.1: Dynamic moduli vs. frequency of fdY21M (L=0.91 μm, $L_p = 9.9$ μm) for several concentrations in the semidilute concentration regime. The lines are theoretical predictions by Morse for the storage (full lines) and loss modulus (dashed lines) in the dilute (thin) and semidilute (thick) concentration regime.

moduli of a dilute rod-like particle suspension calculated from Morse theory. The theory has both the stiffness of the particles as well as the particle aspect ratio as input parameters. At the lowest measured concentration, figure 4.1(a), the theoretical prediction of the loss modulus agrees only quantitatively with the

experiments, while the prediction of the storage modulus is in good agreement to the measurement only in the low and mid frequency regime. At higher frequencies, the measured curve diverges from the prediction.

At higher concentrations, figures 4.1(b) and (c), an even larger deviation of the measurement from the theoretical prediction can be identified, as the curves of $G'(\omega)$ begin to touch those of $G''(\omega)$ in a certain point. Here, we call two curves touching, if the values for G' and G'' at the same frequency are located within the error bars of each other. This feature is not covered by Morse theory, since the curve characteristics of the theory change strongly from low to high concentrations inside the semidilute concentration regime.

At even higher concentrations, figures 4.1(d) and (e), both moduli curves move towards the Morse prediction for the concentrated regime, represented by the thick lines, and start to cross. The measured curve for G'' does not display a non-monotonic functionality as predicted by the theory. Nonetheless, the theory allows for an interpretation of the two crossover points. Comparing with figure 2.2(b), we can interpret the two crossover points as the important relaxation times of the rod-like particle. The lower frequency crossover point can be interpreted as $\tau_{\text{low}}^{-1} = \tau_r^{-1}$ and the higher one as $\tau_{\text{high}}^{-1} = \tau_{\text{flex}}^{-1}$. The theory further predicts the existence of a relaxation time of particle undulations at a length scale much smaller than the particle contour length,τ_e, located at the onset of equal slopes of the two moduli curves at high frequencies. From figures 4.1(b), (c), and (d), also this relaxation time can be estimated as $\tau_e^{-1} \simeq 100\ \text{s}^{-1}$, seemingly independent of the sample concentration. From this value, one can calculate the undulation length, $L_e \sim L_p(\tilde{\rho}L^2)^{-2/5} \simeq 0.9\ \mu\text{m}$, where $\tilde{\rho}$ is the contour length per unit volume, since the fast undulation time is given as $\tau_e \sim L_e^4/D_r L_p$.

It is surprising that the relaxation time for particle undulation, τ_{flex}, is clearly visible, see figures 4.1(d) and (e), given the immense persistence length of fdY21M, $L_p \approx 10L$. Despite the fact that the theoretically predicted elastic plateau region of $G'(\omega)$ does not occur, this speaks for a non-negligible particle bending during flow. Hence, the ideal virus is not fully stiff, if probed at the relevant timescales.

The finite flexibility of fdY21M is also apparent from AFM pictures, see figure 4.2. The ideal virus can obviously bend, maybe due to capillary forces and the proximity to the substrate, being even able to form hair-pins [150] in the dried state close to the polyallylamine surface used for the AFM probes. Despite this obvious flexibility of the phage in the apparent equilibrium state, AFM probes taken with the slightly more hydrophobic substrate coating material aminosilane, inducing a coffee-ring effect [151] and thus a biaxial elongational flow, see figure 4.3, display large fractions of perfectly straight rods. The flow

inducing the coffee-ring effect is seemingly strong enough to order all phages and to straighten all detectable viruses. For LVE measurements at long times, therefore, the viruses can most probably still be regarded as ideal. On shorter timescales, the bending modes seem to play a non-negligible role.

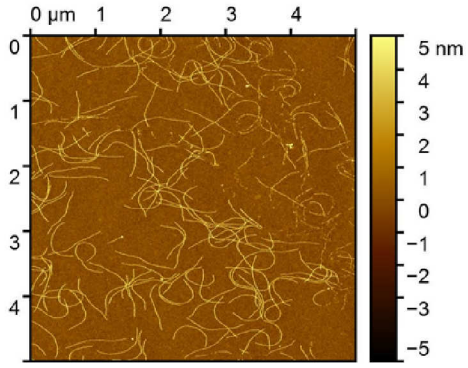

Figure 4.2: AFM picture of fdY21M (L=0.91 μm, L_p = 9.9 μm) virus on polyallylamine substrate. The scale bar on the right shows the object thickness.

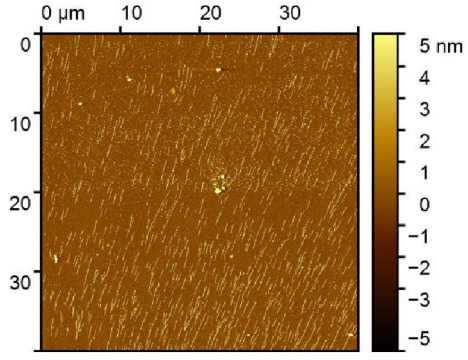

Figure 4.3: AFM picture of fdY21M (L=0.91 μm, L_p = 9.9 μm) virus on aminosilane substrate. The scale bar on the right shows the object thickness.

4.3.2 Steady state shear flow

The nonlinear steady state shear flow behavior of fdY21M is studied by means of step rate tests, where the material is subjected to a constant shear-rate and the shear stress is measured over time. Figure 3.3 shows step rate tests for different concentrations of fdY21M dispersed in glycerol/Trizma buffer at a shear-rate of 10 s^{-1}. The outcome of step rate tests performed in a water based buffer are similar. The curves show an overshoot stress at short times of ~ 0.04 s which relaxes completely after approximately 1 s, followed by a stress plateau. For the calculation of steady state viscosities, the constant long-time shear stress values are averaged and divided by the shear-rate.

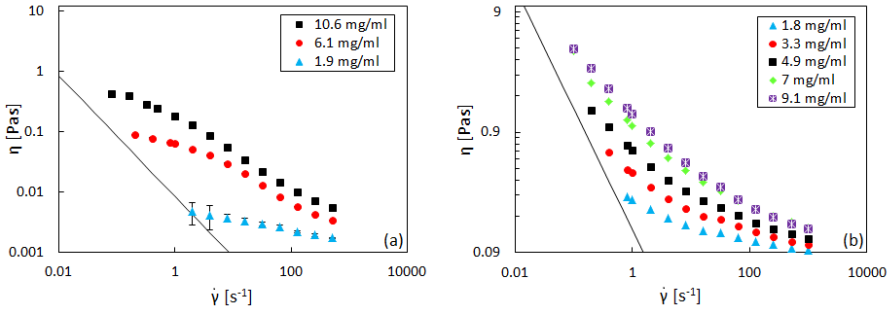

Figure 4.4: Shear viscosity as a function of shear-rate fro different concentrations of fdY21M (L=0.91 μm, $L_p = 9.9$ μm) virus in aqueous (a) and glycerol-based (b) buffers. The lines mark the torque limit of the rheometer. Error bars for higher concentrations in (a) and all concentrations in (b) are vanishingly small.

The nonlinear steady shear viscosity curves for different concentrations of fdY21M dispersed in the watery buffer (a) as well as in the glycerol based buffer (b) are shown in figure 4.4. Obviously, the steady state shear flow of fdY21M in the dilute to semidilute concentration regime is governed by shear thinning. While the onset of a Newtonian plateau, supposedly located at very low shear-rates, is adumbrated for the higher concentration samples in the water-based buffer, see figure 4.4(a), the viscosity curves in glycerol display shear thinning at every measurable shear-rate, compare to figure 4.4(b). Due to the nature of the suspension, one could expect a terminal plateau region $\lim_{\dot{\gamma}\to\infty} \eta(\dot{\gamma}) \to \eta_s$ of the viscosity curves, comparable to the low shear-rate Newtonian plateau. For the measurable shear-rate range, however, neither are detectable, since the inertial limit of the device is reached at 1000 s^{-1}. Despite this fact, the viscosity curves in glycerol, see figure 4.4(b), seem to be closer

to the terminal region then those in water. The reason for this is the slowing down of rotational diffusion caused by the high viscosity of the suspending medium. Together, the two buffers reveal the whole measurable rheological behavior of rod-like colloids under steady shear flow in the dilute to semi-dilute concentration regime.

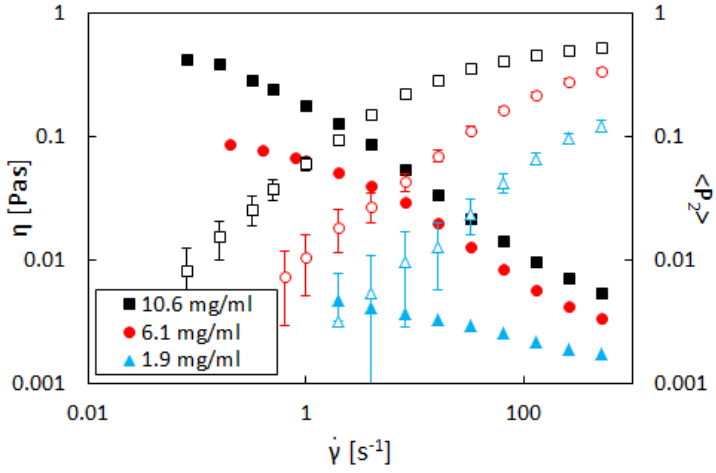

Figure 4.5: Order parameter and shear viscosity as a function of the shear-rate for different concentrations of fdY21M (L=0.91 μm, $L_p = 9.9$ μm) in an aqueous buffer. For the error bars of the viscosity, see figure 4.4.

An interesting aspect is the change of shape of viscosity curves, comparing higher and lower concentrations in the water based buffer, see figure 4.4(a). Although nearly the same concentration of fdY21M was measured in the glycerol-based buffer, the curves in figure 4.4(b) are of similar shape. In general, a similarity in curve-shape assures that the microscopic phenomenon underlying shear thinning is unique. A loss of this aspect on the other hand suggest a more complicated microscopic reason for this macroscopically observable phenomenon. To understand the rheological results, therefore, the structure must be probed.

The nonlinear shear flow behavior of rods is governed by flow-alignment of the molecules and concomitant shear thinning. Figure 4.5 shows the order parameter $\langle P_2 \rangle$ as well as the viscosity as a function of the applied shear-rate. We observe that the orientational ordering of rods increases significantly with increasing shear-rate, leading to strong shear thinning of the sample. The highest order parameter reached under the maximum shear-rate not only differs significantly

from unity, but seems to be concentration dependent. The highest observed orientational ordering thereby decreases with decreasing particle content.

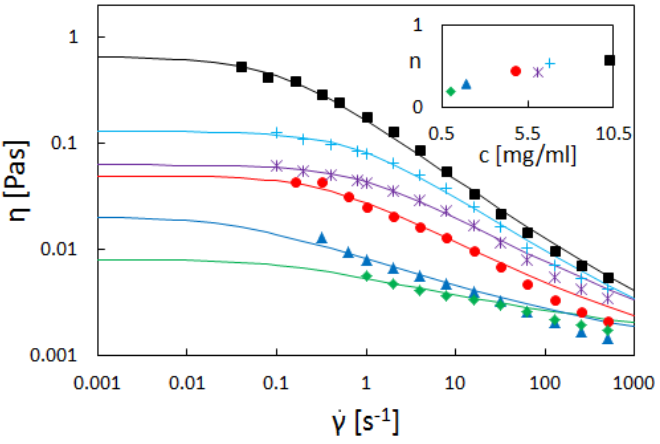

Figure 4.6: Viscosity as a function of shear-rate for different concentrations of fdY21M (L=0.91 μm, L_p = 9.9 μm) in an aqueous buffer, compared to a fit of equation 4.1 using different shear thinning parameters, n, and curve widths, $a = \{10, 1.3, 2.9, 1.3, 27.6, 10\}$ ordered from the highest to the lowest concentration. Inset: Shear thinning parameters as a function of concentration.

Interestingly, the order parameter curve for the lowest concentration does not show a different shape than the other two curves measured for the higher concentrations. Similarity of curve shape of the orientational ordering curves is therefore given for all concentrations, see also figure 4.7. This fact, together with the similarity of shape of shear viscosity curves in worm-like micellar systems was exploited to deduce a scaling procedure for the flow/orientation diagrams of rod-like objects [63]. In the worm-like micellar system, the similarity of curve shape pointed in the direction of a unique underlying phenomenon behind shear thinning being fully governed by the orientational ordering. As a result, a master curve could be drawn by scaling the viscosity with the apparent zero shear viscosity and plotting it as a function of the order parameter [63]. In this way, the zero-shear viscosity, despite not being a measurable quantity, emerged from this scaling procedure. Although worm-like micelles are different from the ideal rod-like system in several ways, we follow this procedure. In the case of the ideal rod, which should be even better suited for such an approach than the worm-like micelles, we learn, however, that the scaling does not lead to a perfect master curve, see figure 4.7. For the scaling of the viscosity in

figure 4.7(b), the highest measured viscosities were taken as an estimate for η_0 for each concentration.

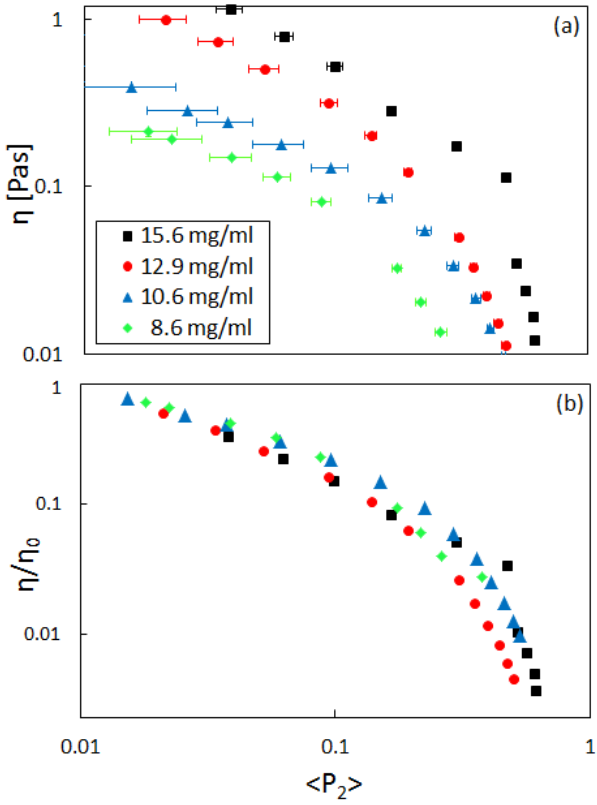

Figure 4.7: (a) Viscosity and (b) relative viscosity as a function of the order parameter for different concentrations of fdY21M (L=0.91 μm, $L_p = 9.9$ μm) in an aqueous solvent. Error bars of the viscosity are negligibly small.

Since the similarity of curve shape of the viscosity curves is lost at low concentrations, no master curve including dilute and semidilute rod-like suspensions can be drawn. Nonetheless, the approach seems to work for the highly concentrated regime, where the zero shear viscosity can be deduced from this scaling procedure under the assumption that the single particle contribution to this quantity is negligible and only the collective behavior is of importance. The reason for the deviation of curve shape for lower concentrations, however, remains unclear. To deduce the zero shear viscosity for the low concentrations,

the Carreau [152] constitutive equation,

$$\eta - \eta_s = (\eta_0 - \eta_s)/(1 + a\dot{\gamma})^n \quad , \tag{4.1}$$

with one parameter determined by $a = Pe/\dot{\gamma}$ and a free exponent, n, is used to fit the measured flow curves, see the inset in figure 4.6. The high concentration zero shear viscosities from this fitting procedure match with those obtained by scaling.

Since the collective response of orientational ordering causes shear thinning, the full measurement results from figure 4.5 can be plotted as a function of the effective Peclet number, $Pe_{\text{eff}} = \dot{\gamma}/D_r^{\text{coll}}$, instead of the shear-rate. Figure 4.8 shows the master curve of orientational ordering and concomitant shear thinning for all concentrations of fdY21M. The Peclet number is scaled with the collective rotational diffusion coefficient, $D_r^{\text{coll}} = D_r(1 - \varphi/\varphi_{IN})$. This is similar to equation 2.62, except that we allow D_r to be concentration dependent.

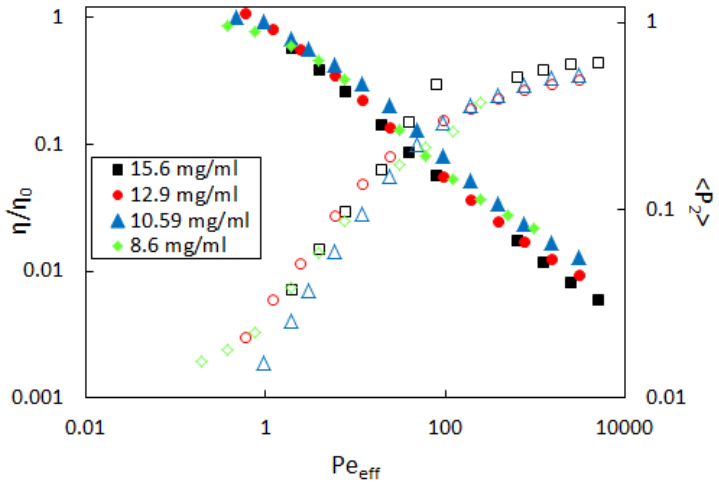
1
0.1
0.01
0.001
η/η0
15.6 mg/ml
12.9 mg/ml
10.59 mg/ml
8.6 mg/ml
0.01
1
100
10000
Pe_eff
1
0.1
0.01
<P2>

Figure 4.8: Order parameter (open symbols) and scaled shear viscosity (full symbols) as a function of effective Peclet number for different concentrations of fdY21M (L=0.91 μm, $L_p = 9.9$ μm) in an aqueous buffer.

We find that $\varphi_{IN} = 4.3$, somewhat higher than the theoretically predicted equilibrium transition. D_r is plotted in figure 4.9, together with the corresponding values for η_0. The line in figure 4.9 is a prediction of the zero shear viscosity using the revised Dhont-Briels theory, equation 2.76. In

principle, both quantities should be related via equation 2.74. In the following chapter, we will confirm this relation using rods of different contour length.

While the theoretical prediction is in very good agreement with the apparent zero shear viscosities at higher volume fractions, it underestimates the values found for lower concentrations. This points in the direction of a reduced rotational diffusivity of particles even at rather low concentrations, where the predicted values for $\overline{D}_r$ approach D_r^0. In other words, the rotational diffusivity is not free for all measured concentrations, but constrained according to the tube model.

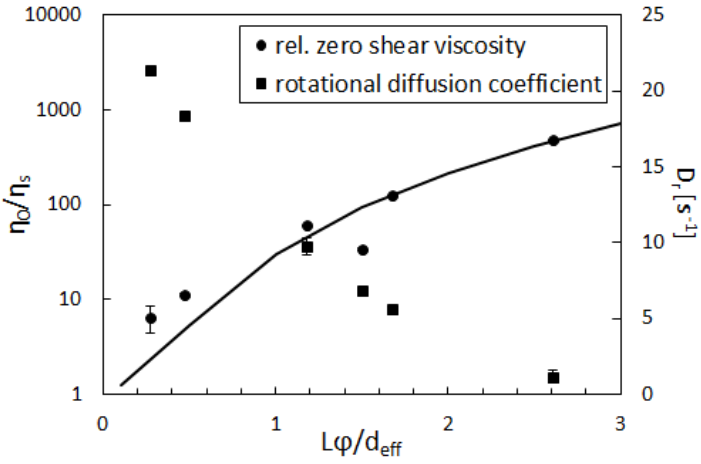

Figure 4.9: Scaled zero shear viscosity and fitted rotational diffusion as a function of scaled volume fraction for fdY21M (L=0.91 μm, $L_p = 9.9$ μm) in an aqueous buffer. The line is a prediction from the revised Dhont-Briels theory, using the tube model, equation 2.76.

So far, we highlighted the orientational ordering of rods in the flow-vorticity plane, figures 4.8 and 4.9. In general, we cannot assume that the orientational ordering of rods in gradient and vorticity direction is identical. On the contrary, the flow in a Couette geometry should hardly permit transmission of momentum in the vorticity direction, but most momentum transfer of the fluid should take place in gradient direction. This is a theoretical result, following from the identical symmetry of the elastic part of the stress tensor and the orientational ordering tensor, equation 2.58. This would cause the orientational ordering tensor to be biaxial with a higher ordering in the gradient direction as compared to the vorticity direction, thus a negative biaxiality according to our definition, see equation 3.8. In figure 4.10(b), the order parameters in the flow-gradient

plane, $\langle P_2 \rangle(\phi)$, and in the flow-vorticity plane, $\langle P_2 \rangle(\theta)$, are shown as a function of the effective Peclet number. We cannot identify large differences between the two order parameters. This is reflected in the small amplitude of the biaxiality, shown in figure 4.10(a). The close similarity of both orientational ordering curves points in the direction that the momentum transfer in the rod suspension is evenly distributed between gradient and vorticity direction. The reason for this could be the quasi-uniaxial nature of the stiff constituent particles. If this was the reason for the observed flat biaxiality, the theoretical prediction by Dhont and Briels should predict no biaxiality, since it assumes perfectly thin, uniaxial rods. This is not the case, as indicated by the lines in figure 4.10. It is, thus, surprising that the ordering of fdY21M in gradient and vorticity direction is almost identical. Nonetheless, two important details should be discussed. First, we observe a sign change of the biaxiality, $\mathcal{T}$, around $Pe_{\text{eff}} \approx 5$, indicating a higher momentum transfer in vorticity direction as compared to the momentum direction in this regime. Second, at high Peclet numbers, the biaxiality seems to increase strongly, reaching values almost as high as the theoretically predicted final value. Neither of these characteristics is theoretically predicted. We conclude from this observation, that it is not generally true that the symmetry of the elastic part of the stress tensor is equal to that of the orientational ordering tensor. This is, if ever, only correct for high applied shear-rates. In the low and intermediate shear-rate regime, the collective dynamics of rods do not follow the symmetry conditions of the applied field.

Theoretical predictions of the shear dependent viscosity and the order parameter can also be compared directly to the measured data. Figure 4.11 shows the relative viscosity and orientational ordering for fdY21M at 10.6 mg/ml, compared to Dhont-Briels theory using different rotational diffusion coefficients. The dash-dotted line is the original Dhont-Briels theory, combined with the rotational diffusion coefficient of a free rod, D_r^0 [87, 86], see equation 2.25. Although the original theory does predict an increase in order parameter connected to shear-thinning behavior, it is not in good agreement with the measured data since the onset shear-rate for shear thinning is too high and the zero shear viscosity is too low.

When the tube model is taken into account, assuming an isotropic rod distribution, the rotational diffusion is severely decreased as compared to the free particle motility, see equation 2.70. This leads to a correct prediction of the onset shear-rate for shear thinning as well as the correct zero shear viscosity, compare also to figure 4.9. Nonetheless, larger deviations from the measurement at low as well as high shear-rates can be found. If the assumption of isotropic surrounding is dropped, the rotational diffusivity is allowed to depend on the orientational ordering: $\langle D_r \rangle = \langle D_r \rangle(S)$, see equation 2.72. This leads to a

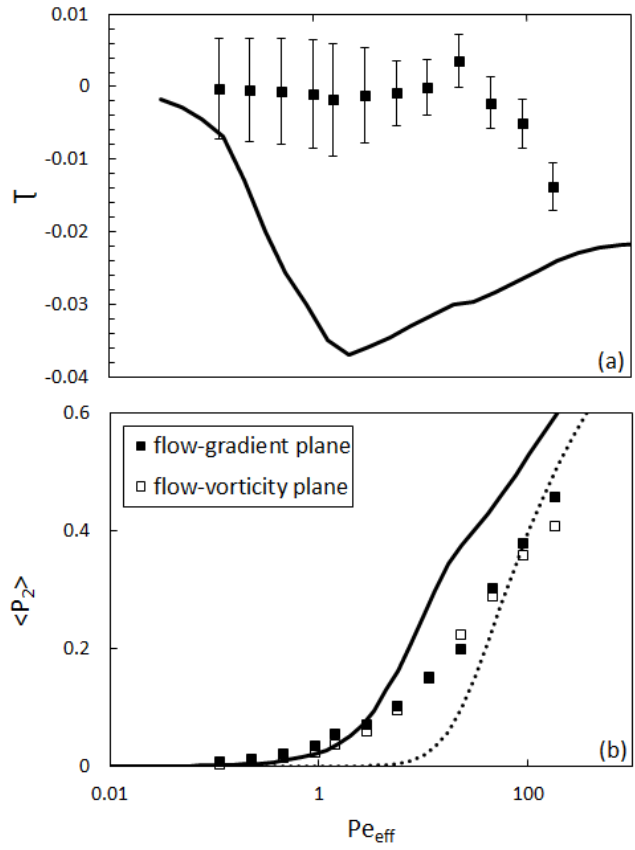

Figure 4.10: (a) Biaxiality and (b) order parameter in gradient and vorticity direction as a function of the effective Peclet number for fdY21M (L=0.91 μm, $L_p = 9.9$ μm) at a concentration of 10.6 mg/ml in an aqueous buffer. The curve in (a) shows a prediction from Dhont-Briels theory, equation 2.59. The curves in (b) show the theoretical order parameters in gradient (full line) and vorticity (dotted line) direction. Error bars in (b) are omitted for reasons of readability.

slightly better agreement between the theoretical prediction and the measured data, see the full lines in figure 4.11. However, discrepancies between theory and measurement remain. If the pair correlation function, used in equations 2.31 and 2.53, is changed from the Onsager [41] equilibrium pair correlation function, $g^0 = \exp[-\beta\mathcal{V}]$, to a first order shear-rate dependent approximation of the non-equilibrium pair correlation function, $g \approx g^0(1 + Peg^1)$, the resulting theoretical

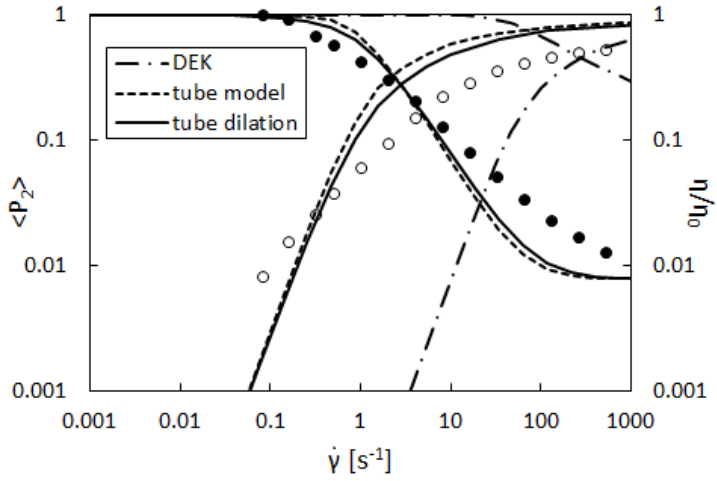

Figure 4.11: Reduced viscosity (full symbols) and order parameter (open symbols) as a function of shear-rate for fdY21M (L=0.91 μm, $L_p = 9.9$ μm) at 10.6 mg/ml in an aqueous buffer. The lines are predictions from Dhont-Briels theory using different rotational diffusion coefficients: equation 2.25 (dash-dotted), equation 2.70 (full), and equation 2.72 (dashed). For the error bars, see figures 4.4, and 4.5.

prediction is in much better agreement with the measurement results of the viscosity, see figure 4.12. As described in section 2.8, this change in the pair correlation function requires an estimate of C^0. Here, $C^0 = -0.2$ was used, indicating that the impact of shear flow on the pair correlation function is relatively small with a deviation of 20% from the equilibrium pcf at a Peclet number of $Pe = 1$. However, at the same time, the estimated order parameter at high shear-rates drops significantly. While Dhont-Briels theory together with shear induced tube dilation overestimates this value, the improvement on the theory underestimates it. It is, therefore, possible to make a different choice of C^0, trying to fit both the viscosity and the order parameter at high shear-rates with the smallest possible error. This procedure, however, will not contribute to the understanding of the non-equilibrium thermodynamics of rods and, thus, will not be shown in this work.

Comparison to Dhont-Briels theory shows that the particle dynamics play a key role in understanding the non-equilibrium behavior of rod-like particle suspensions. The measurement even suggests that the effect of tube dilation

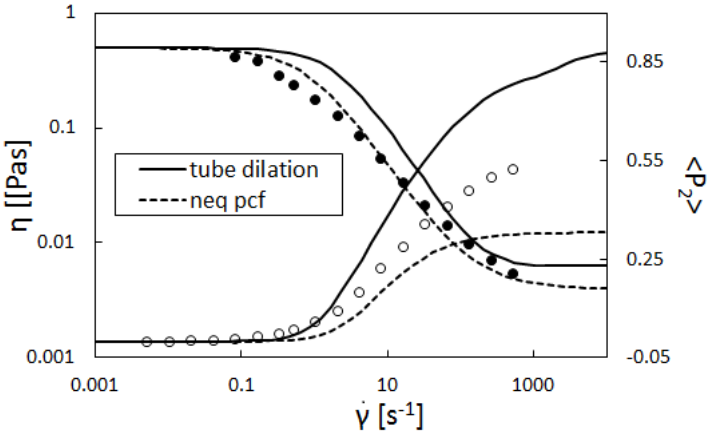

Figure 4.12: Reduced viscosity (full symbols) and order parameter (open symbols) as a function of shear-rate for fdY21M (L=0.91 μm, L_p = 9.9 μm) at 10.6 mg/ml in an aqueous buffer. The lines are predictions from Dhont-Briels theory using different pair correlation functions: equation 2.59 (full), and equation 2.90 with $C^0 = -0.2$ (dashed).

could be stronger than predicted. This means that the mean value of the rotational diffusion coefficient used in the calculation might not be an ideal measure for relaxation of molecules at high shear-rates. Instead, rotational relaxation should probably become almost free at high shear-rates. This, however, seems to be compensated in large part by the use of a shear-rate dependent pair correlation function. This result can be understood in terms of the excluded volume of rods. The excluded volume between particles decreases with increasing shear-rate. This effect should be accounted for by using higher virials in the Fokker-Planck equation 2.80, but can also be partly accounted for by using the non-equilibrium pair correlation function, see equation 2.90. However, certain discrepancies between experiment and theory remain due to the assumptions taken. The road to a non-equilibrium pair correlation function with less assumptions is given in section 2.8, but the resulting equations were not solved analytically at the given time.

4.3.3 Uniaxial elongational flow

The behavior of rod-like particle suspensions under uniaxial elongational flow is probed by capillary breakup extensional rheometry. Since this measurement technique requires filament stability, resulting from a relatively high viscosity of the sample, glycerol/Trizma buffers are used.

While orientational ordering in shear flow approaches steady state values for sufficiently long times, this is not the case for high-extension-rate extensional viscosities as found in many industrial applications, where the time-scale of the processing step during which extension occurs is shorter than the time needed for equilibration [153, 154]. This leads not only to a significant difference between achievable orientational ordering in shear and elongational flows [155], but also to a change in the Trouton ratio, which is defined by the ratio of the elongational viscosity and the shear viscosity, η_e/η. Figure 4.13 shows the elongational viscosity in comparison the shear viscosity as a function of the square root of the second invariant of the rate of deformation tensor, $\Pi_2 = \sqrt{|\Pi_{2D}|} = \dot{\gamma} = \sqrt{3}\dot{\epsilon}$, for different concentrations. From one single measurement, two points can be deduced, since the extension rate is a function of the capillary diameter, see equation 3.2. The first points are calculated at the onset of the final filament thinning regime, see figure 3.4, where a cylindrical filament is formed. The second point is taken just before filament rupture. Since the elongational viscosity is calculated from the surface tension, which is assumed to be shear-rate independent, the value for this quantity is independent of the filament thickness and, therefore, constant over the measured rates, as indicated by the lines connecting the hollow markers.

In comparison to the measurement under steady shear, it is obvious that the values of the extensional viscosity are located in a rate region shortly before a terminal plateau for the shear viscosity is reached. Therefore, a concentration and rate dependent Trouton ratio can be calculated. For Newtonian liquids, the Trouton ratio is 3. For the case of rods, Trouton ratios between 3 and 12 can be found, depending on the concentration of the sample.

Similar to the zero shear viscosity, the elongational viscosity increases strongly with increasing concentration. Figure 4.14 shows the elongational viscosity as a function of the relative volume fraction. Both, the theory by Batchelor [91], and by Shaqfeh and Fredrickson [82], agree well with the measurement results. This agreement, however, is only reached by using the hydrodynamic particle aspect ratio L/d_{HD} as a fitting parameter. The effective hydrodynamic thickness, d_{HD}, of rods in the glycerol/Trizma buffer is estimated as $L/d_{\mathrm{HD}} = 42$, as indicated in the legend of figure 4.14. The estimated hydrodynamic thickness found by curve fitting agrees with measured values from the literature [156].

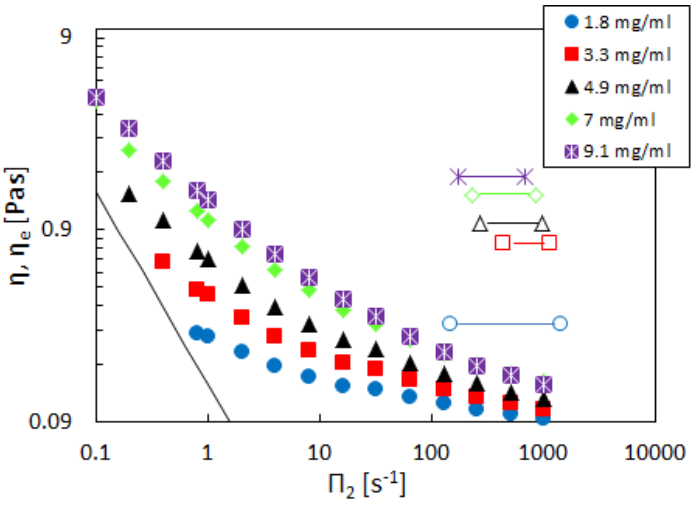

Figure 4.13: Shear (full symbols) and elongational (hollow symbols) viscosity as a function of Π_2 for different concentrations of fdY21M (L=0.91 μm, $L_p = 9.9$ μm) in a glycerol-based buffer. The thin inclined line indicates the torque limit of the rheometer. The error bars are vanishingly small.

The large concentration dependence of the elongational viscosity is interesting, given the fact that at these high rates, the differences between shear viscosities are almost vanishingly small. A full explanation cannot be given without the measurement of orientation under elongational flow. However, it should be remarked that the excluded volume could play a very important role in this high extension rate regime, if this quantity plays a similarly important role as in the simpler steady shear case.

4.4 Rheology near the IN transition

Sufficiently close to the upper isotropic-to-nematic spinodal point, the collective rotational diffusion of rods, $D_r^{\text{coll}} = D_r^0(1 - \varphi L/4d)$, goes to zero, as established in chapter 2 and experimentally shown in section 4.3.2, figure 4.9. As the flow orients the particles strongly, see, e.g., figure 4.5, shear alignment values at high shear-rates could reach nematic levels in the vicinity of the isotropic-nematic phase transition. Additionally, the IN spinodal depends on the shear-rate [87, 78, 157, 83, 84, 85, 158, 86, 38]. In a projection of the free energy surface

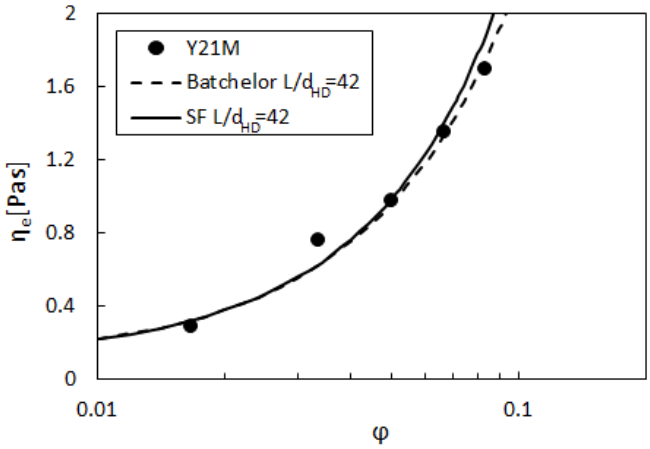

Figure 4.14: Elongational viscosity as a function of volume fraction, $\varphi = (\pi/4)dL^2\nu$, for fdY21M (L=0.91 μm, $L_p = 9.9$ μm) in a glycerol-based buffer. The lines are theoretical predictions, equations 2.26 (dashed), and 2.27 (full), for the given aspect ratios indicated in the legend.

of rod-like suspensions into the shear-rate/concentration plane, the isotropic-nematic spinodal line can be visualized as a function of the two variables $f_{IN} = f_{IN}(\varphi, \dot{\gamma})$. In order to induce a phase transition by enhancing the shear-rate, therefore, the derivative $\partial f_{IN}/\partial\varphi$ would have to be negative over a certain range of $\dot{\gamma}$.

If this were the case, an instability of flow along the velocity gradient direction would be expected, called gradient shear banding instability (GSBI). The instability, thereby, arises from a phase transition induced only in a certain part of the gap of the Couette cell where the flow rate has a magnitude corresponding to $\partial f_{IN}/\partial\varphi < 0$. Since the liquid in parts of the gap would change its phase, the actual shear-rate would change abruptly at a certain position along the gradient direction. Therefore, a GSBI might be detected experimentally by probing the velocity profile of the liquid along the gradient direction. Due to the difference in shear-rates, the velocity profile then shows different slopes in different parts of the channel with a certain transition regime between them. The transition regime could be called the phase boundary layer. Another option of detecting a GSBI is conducting steady-state shear flow and measuring the shear stress as a function of shear-rate. The slope of the curve is called the shear thinning parameter, m, defined by the relation $\Sigma_{21} = k\dot{\gamma}^m$. We remark that we call both the exponent in this power-law, m, as well as the exponent

in the Carreau equation, n, shear thinning parameter, since they are directly proportional to each other with $n = m - 1$. It has been reported for manifold systems that a shear thinning parameter $m \ll 1$ indicates a flow instability [159, 160, 161, 162]. Therefore, a locally strong shear thinning behavior points in the direction of an instability. To characterize a GSBI fully, a combination of both measurements is ideal.

An additional factor that influences the flow behavior of rod-like viruses near a phase boundary is the salt content of the buffer. Since the Debye double layer thickness around the virus increases with decreasing salt content [70], the IN spinodal point also shifts to lower volume fractions. Limited experiments on rods exist, however, where the spinodal line is probed as a function of salt content [163], although experiments on xanthan gum [159] and wormlike micelles [164] both show a strong dependence on the salt concentration. Therefore, also the salt content of the Trizma buffer is varied in this experimental investigation. Three buffers with ionic strengths of 100, 20, and 1 mM are used for this purpose. The Debye double layer thickness varies for all ionic strengths, yielding effective virus thicknesses of 10.5, 18, and 25 nm [70].

Figure 4.14 shows the steady state shear behavior for three concentrations of fdY21M in a 100 mM ionic strength Trizma buffer. Three regions can be distinguished: In the low and high shear-rate regimes, the system shows an increasing shear stress with increasing shear-rate with a constant slope, m. In the intermediate shear-rate region, the slope changes to lower values. The shaded area marks this region. Here, the probability for shear banding is the largest. As explained above, the concentration plays a key role. Indeed, only for concentrations sufficiently close to the isotropic binodal , the curves flatten significantly in this regime. Here, the highest probed concentration is $\varphi = 0.97\varphi_I$, where the experimentally measured value for φ_I, reported in table 3.2, was used. According to theoretical investigations [83, 84, 85, 158, 86], this is close enough to the isotropic nematic spinodal line to detetct a GSBI. However, the value for m is not low enough for suspensions in this high ionic strength buffer to be suspicious for a GSBI to occur. For other systems, values between $m = 0.1 - 0.038$ have been reported in the case of shear banding [165, 161]. Here, the steepest shear thinning region is characterized by $m = 0.43$ which is expected to be too high for the occurrence of a GSBI.

Figure 4.16 shows the shear stress as a function of shear-rate for varied salt content of the fdY21M suspension at concentrations sufficiently close to the isotropic binodal point. Table 4.1 lists the different concentrations in dependence of the isotropic binodal point. Figure 4.16 indicates that the value of the shear thinning parameter in the intermediate shear-rate regime is lowest for an intermediate salt content of 20 mM. Since a value of $m = 0.36$ is found for the lowest ionic strength buffer, this system is not likely to undergo gradient

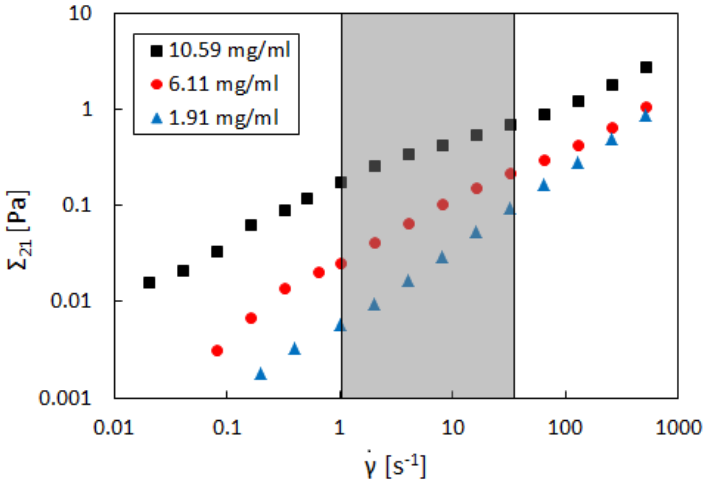

Figure 4.15: Shear stress as a function of shear-rate for three different concentrations of fdY21M (L=0.91 μm, L_p = 9.9 μm) in 100 mM Trizma buffer. The shaded area marks the regions of lowest shear thinning parameter. The error bars are vanishingly small.

shear banding in either buffer. Only for very low salt content, where the rods effectively form a glass, instabilities were reported [66, 166, 167].

Table 4.1: Ionic strength, effective thickness, concentration, and shear thinning parameter in the shaded area of figure 4.16 relative to the experimentally estimated isotropic binodal for different samples of fdY21M (L=0.91 μm, L_p = 9.9 μm).

ionic strength mM	$d_{\mathbf{eff}}$ [24] nm	$(L\varphi/d)/(L\varphi/d)_I$	m
100	10.5	0.97	0.45
20	18	0.98	0.36
1	60	0.99	0.42

To probe for a GSBI directly, fdY21M in a 20 mM Trizma buffer close to the IN transition is investigated using flow-LDV. All shear-rates in the interesting intermediate shear-rate regime, indicated in figure 4.16, are probed. Figure 4.17 shows some exemplaric velocity profiles, $v(y/y_0)/v_0$, where v_0 is the velocity of the moving inner wall and the coordinate y points in the gradient direction

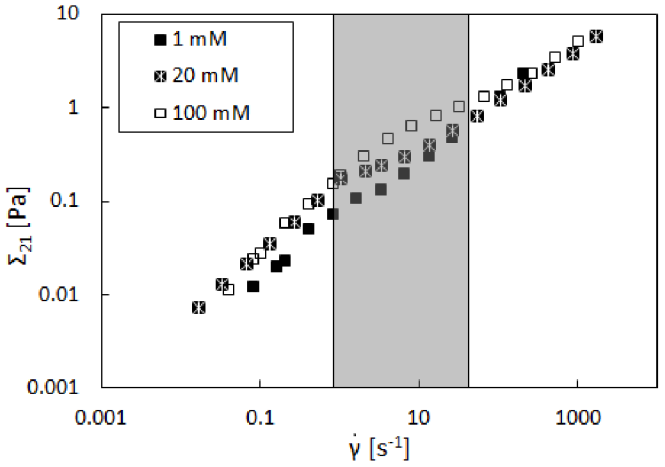

Figure 4.16: Shear stress as a function of shear-rate for fdY21M (L=0.91 μm, $L_p = 9.9$ μm) in aqueous buffers of three different ionic strengths, sufficiently close to the experimental isotropic binodal. The shaded area marks the regions of lowest shear thinning parameter. The error bars are vanishingly small.

and is normalized by the inner wall position of the Couette cell, y_0. Despite the low value of the shear thinning parameter compared to samples of different ionic strength, no significant change in gradients can be observed for any of the experiments carried out. A slight deviation of the line, marking the power law behavior expected for the reported shear coefficients, can be detected. Except for this small deviation at a shear-rate of 4 s^{-1}, which vanishes for larger shear-rates, the velocity profiles show no signs of shear banding, as expected. This means that we never reach the IN spinodal line, $\partial f_{IN}/\partial\varphi$, for fdY21M at all probed ionic strengths, shear-rates and concentrations. A detailed investigation of the spinodal line for different salt content under shear, however, remains for future investigations. The problem we encounter here is that we cannot approach the spinodal, $\varphi_{IN} = 4.3 d_{\text{eff}}/L$, by force, since the system becomes unstable at concentrations above the binodal, $\varphi_I = 3.4 d_{\text{eff}}/L$.

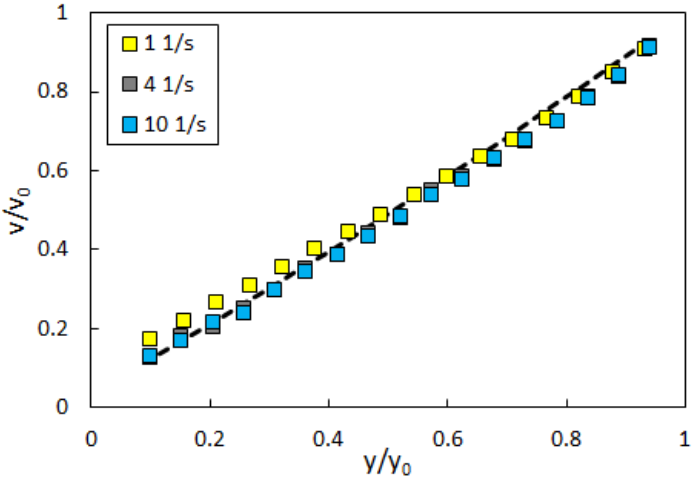

Figure 4.17: Velocity profiles of fdY21M (L=0.91 μm, L_p = 9.9 μm) in an aqueous 20 mM Trizma buffer close to the experimentally estimated isotropic spinodal for different shear-rates. The line marks a power law with a shear thinning parameter m=0.36. The error bars are vanishingly small.

4.5 Summary

The linear and non-linear response of ideal colloidal rods to shear flow as well as extensional flow was investigated. Interestingly, the non-linear response could be reasoned on the base of an extended version of Dhont-Briels theory, employing the tube model for highly concentrated dispersions, at $\varphi = 280\varphi^*$ and higher. For these dispersions also a master curve could be constructed for both the scaled viscosity and the orientational ordering, as measured by SANS, yielding the zero shear viscosity as well as the collective rotational diffusion coefficient and the isotropic-to-nematic spinodal point. However, the prefactor for the rotational self-diffusion was much lower than the diffusion at infinite dilution. In the next chapter, we will show how this factor can be determined experimentally by studying the response of rods of varying length. On the contrary, the linear response compared well to the theory by Morse only at low concentrations. With increasing concentration, the moduli were overestimated by this theory. As this theory works well for much longer filaments [65], it suggests that the rods were not long enough to render a sufficiently entangled system.

This is also reflected in the very moderate shear thinning of this system, even at the highest possible concentration in the isotropic phase.

The extensional viscosity, where entanglement does not play a role, was found to be in good agreement with purely hydrodynamic theory.

Chapter 5

Non-ideal rods

5.1 Introduction

In the previous chapter, we described the rheological response of an ideal colloidal rod from the linear to the very non-linear regime. On the basis of an extended version of the available theory, it was possible to describe the shear-thinning process. We also learned that there still is a signature of the flexibility of the rod, even though the persistence length is ten times longer than the contour length. Moreover, the contour length is neither sufficient to cause a strong shear-thinning nor high moduli in dynamic tests. The tube model predicts an extremely strong rod-length dependence of the rotational diffusion [168] and, therefore, of the zero shear viscosity, see equation 2.71. Thus, it would be interesting to study the effect of length, making use of the accessible library of filamentous viruses. However, in this library only the contour length changes and thus also the ratio L_p/L. Hence, the first objective of this chapter is to study the effect of flexibility and length at the same time, by comparing the rheological response of dispersions with two viruses of similar length but different bending rigidity, k_BTL_p, sections 5.2 and 5.3.1, and of viruses with the same persistence length but varying contour length, sections 5.3.2 and 5.3.3. This will enable us to test the predicted length dependence of the tube model. With that we will also be able to do predictions for the many complex fluids containing rod-like particles as encountered in biology and industry. Such systems, among which are F-actin [50, 51, 169], DNA [170, 171, 172, 173], and carbon nanotubes [45, 46, 47], are known for their very polydisperse length distributions. As we will show that, indeed, the length dependence of the zero shear viscosity, and with that the length dependence of the shear-thinning behavior, is extremely strong,

this also means that the tails of the length distribution of such systems might significantly influence the rheological response. Using well-defined bidisperse mixtures of rods with different length, we derive mixing rules that can be applied to polydisperse systems, see section 5.6. In section 5.5, the dynamics of rod-like colloids after cessation of shear flow are discussed as an addition to the linear rheology. Finally, the influence of flexibility and length on the rheology in the vicinity of the IN phase transition and its potential influence on flow instabilities is presented in section 5.7.

5.2 Effect of flexibility on the dynamic rheological response

In section 4.3.1, it is shown that the ideal rod, fdY21M, displays a significant influence of the flexibility on the LVE behavior. Specifically, the relaxation time of particle undulation, τ_{flex}, as a function of concentration could be measured. The SAOS response of the ideal rod, thereby, showed an emerging elastic region at intermediate reciprocal times, but no elastic plateau. To identify the effect of flexibility on the relaxation time spectrum, we make use of our library of rod-like viruses and compare two species which are similar in length, $L \approx 0.9$ μm, but differ strongly in their persistence length, namely 9.1 μm for the ideal rod fdY21M, and 2.1 μm for the flexible fd wild-type virus. Both species are suspended in glycerol/Trizma buffers at different concentrations and the dynamics of rods are probed by SAOS.

In figure 5.1, the LVE behavior of both systems is compared. We remark that the data on fdY21M were already shown in chapter 4. Figure 5.1(a) shows the complex moduli of fd wild-type at the lowest measured concentration. The loss modulus predicted by Morse theory [80, 111, 112] is in good agreement with the measurements, as it is for the stiffer fdY21M virus that was discussed in the previous chapter. The loss modulus is higher than the elastic modulus for all accessible frequencies. The first influence of particle flexibility on the LVE behavior is indicated by the differences between theory and measurement regarding the storage modulus curve at this low concentration. The measured storage and loss moduli show an almost constant slope over the given frequency range. This stands in marked difference to the measured storage modulus of the stiff system, displaying a curved region at intermediate frequencies. Also, the high frequency upturn of the storage modulus curve, for estimation see figure 5.4, is found at lower frequencies for the more flexible virus as compared to the stiff one, compare figures 5.1(a) and (b). The theoretical description seems correctly predict the storage modulus of the stiff virus at intermediate and low frequencies, while it is not in good agreement with the measurements on

the flexible phage. Since the theory should fully account for flexibility influences on the LVE behavior, this discrepancy cannot be explained from rheological data alone. Our hypothesis is that entangled rodlike systems have a certain tube heterogeneity. The rods diffuse according to the tube model only until they reach a dead end, where the parallel diffusion is strongly restricted. At such a locus, the rod rotates without further positional movement until the surrounding has rearranged in a way that the nearest adjacent tube can be reached. Then, the rod diffuses according to the tube model again. In this way, the rotational diffusivities in those two situations differ strongly, such that rotational diffusivities exist which are partly "smeared" with the undulation time. Evidence for this can be found in fluorescence microscopy studies for viruses of different morphology [174]. This could explain also, why no elastic plateau region is found in our experimental study, but only a hardly visible crossing over of the moduli curves.

To illustrate the flexibility dependence of the storage modulus, the theoretical prediction with different particle persistence lengths is shown, figure 5.1(a). The persistence length of fd wild-type, calculated from microscopy experiments [70], is 2.8 ± 0.7 μm. Therefore, the theoretical curves for 2.1 μm (black curve), 3.5 μm (blue curve) are shown and compared to the theoretical prediction for the stiff virus, having a persistence length of 9.1 μm (red curve). It is obvious that no differences between the theoretical predictions are found in the low to intermediate frequency range. The only deviations are found in the high frequency range, where the measurement range of the device terminates. Nonetheless, we identify the measured upturn of the storage modulus curve for lower persistence lengths, compare the blue and red curves in figure 5.1(a).

Since the description of the stiff phage is reasonable, the discrepancy for the flexible rod can be identified as a weakness of the theoretical description. Apparently, the enhanced flexibility of the fd wild-type leads to a completely monotonic increase of the storage modulus with increasing frequency, displaying no indications for any characteristic time in the measurable range of frequencies.

This, however, changes strongly with enhancing the concentration, see figure 5.1(c). While Morse theory for dilute systems under-predicts the magnitude of the storage modulus, as discussed already in section 4.3.1, the curve form of the storage modulus of fd wild-type displays the predicted changes in slopes located at the characteristic time of rotational diffusion, compare to figure 2.2. Since the storage and loss modulus curves touch in this point, the rotational relaxation time can be identified by the measurement. As indicated in figure 5.1(c), the rotational relaxation times of both rods are similar. The calculated value of D_r for fdY21M is 0.22 s^{-1} and the value for fd wild-type is 0.23 s^{-1}, being roughly a factor 2 lower than the measured values found from the touching points of these curves.

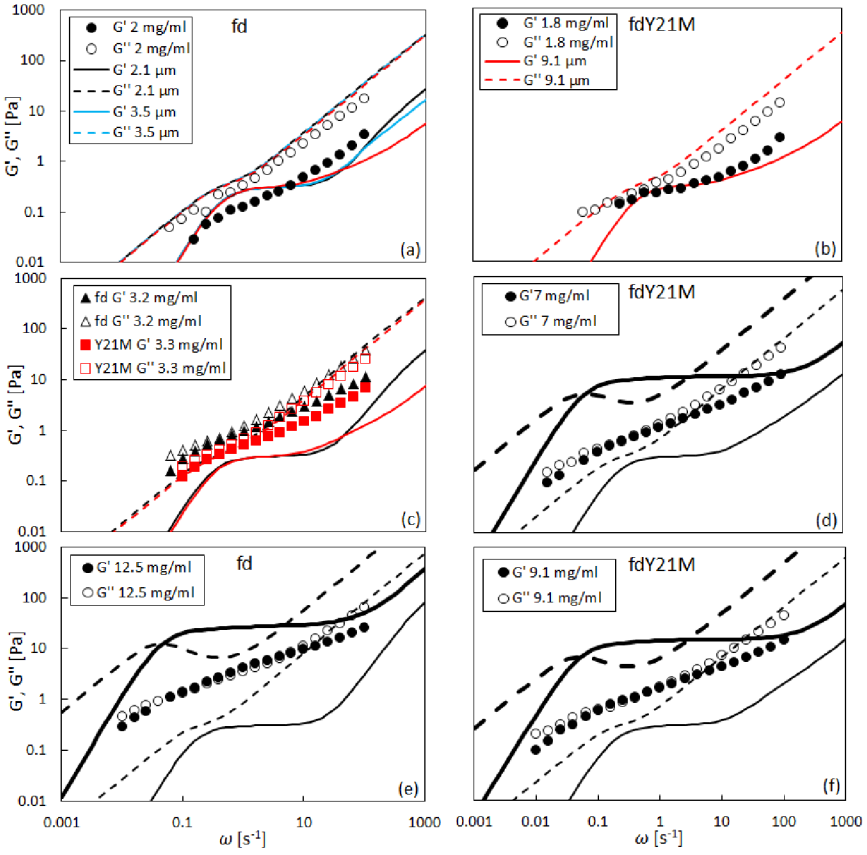

Figure 5.1: Complex moduli as a function of frequency for (a) and (e): fd wild-type ((L=0.88 μm, $L_p = 2.8$ μm)), (b), (d) and (f): fdY21M (L=0.91 μm, $L_p = 9.9$ μm) and (c) both viruses at different concentrations. The lines in (d), (e), and (f) are predictions from Morse theory in the dilute (thin lines) and semidilute (thick lines) concentration regime. The lines in (a), (b), and (c) are predictions from Morse theory for dilute systems for different persistence lengths. The red line in (a) is identical to the red line in (b). Error bars are vanishingly small.

At higher concentrations, two crossover points can be found for both systems, marking the rotational relaxation time and the relaxation time of chain undulation, see the illustration in section 2.9(b). From a comparison of figures 5.1(e) and (f), it becomes clear that the elastic region of fd wild-type is significantly wider than that of fdY21M. Also, the slope of the storage modulus between the two characteristic times is slightly lower for the more flexible virus than it is for the stiff system. An enhanced particle flexibility, therefore, broadens the elastic region and shifts the relaxation time of chain undulation to smaller values.

To clarify this effect of particle flexibility on the LVE behavior, the touching (open symbols) and crossover points (closed symbols) for both systems are compared in figure 5.2. The touching points and lower frequency crossover points indicate the rotational diffusion coefficients for both rods as a function of concentration. The increase of the associated relaxation time with increasing concentration is predicted by Morse in accordance with the tube model. The measurement suggests that despite the difference of experiment and theory in terms of magnitudes of those crossover points, the concentration dependence is similar. For either rod-like system, seemingly independent of the stiffness, the rotational diffusion coefficient decreases with increasing concentration varying roughly between 0.06 and 0.4 s^{-1}. The concentration dependence of τ_r points in the direction that the rotational diffusion measured by the lower frequency crossover points is indeed reasonably characterized by $\overline{D}_r = D_r^0(\nu L^3)^{-2}$, see the lines and full symbols in figure 5.3.

As indicated for the ideal rod, fdY21M, in section 4.3.1, no single relaxation time characterizing the full LVE behavior of rods exists. Instead, a relaxation time spectrum must be considered. Additionally, the flexibility of the rods adds to the "smearing" of relaxation times. As predicted by Odijk [104] for the isotropic as well as the nematic phase [175] in equilibrium, rod flexibility changes the characteristic time-scales. Odijk, in particular, developed a criterion for identifying particles which diffuse according to the tube model and particles which are more mobile due to constraint release caused by their flexibility. The second case will be referred to as Odijk regime here. Since the isotropic network in the quasi-linear response regime is comparable to that in equilibrium, the Odijk criterion applies to our measurements. For a given tube diameter, D_{tube}, the flexibility of the particle starts to play a role if $D_{\mathrm{tube}} < L < D_{\mathrm{tube}}^{2/3} L_p^{1/3}$. The tube diameter can be approximated by the mesh size of the rod network, $D_{\mathrm{tube}} \sim \nu L^2$. By comparison to the criterion, both systems, fd wild-type as well as fdY21M, are not in the Odijk regime, as their deflection lengths, $D_{\mathrm{tube}}^{2/3} L_p^{1/3} \approx 1.8 \pm 0.35$ μm for fd and 6.4 ± 0.4 μm for fdY21M, are significantly larger than their contour lengths. Therefore, the rotational diffusivity of both systems can be fully characterized by the rotational diffusion coefficients measured via

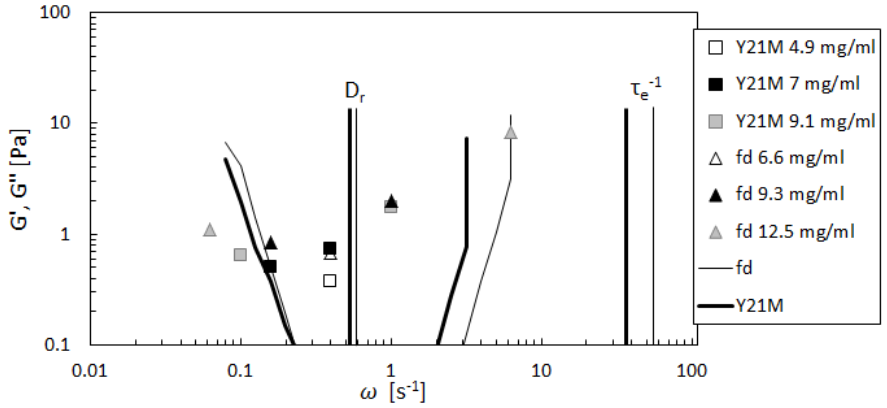

Figure 5.2: Touching (open symbols) and crossover points (closed symbols) of storage and loss modulus as a function of frequency for fd wild-type (L=0.88 μm, L_p = 2.8 μm) and fdY21M (L=0.91 μm, L_p = 9.9 μm) at different concentrations. The curves are predictions from Morse theory. The vertical lines in the middle indicate the theoretical rotational relaxation time from equation 2.70 for a concentration of $L\varphi/d = 2.6$, the vertical lines on the right show the reciprocal undulation time for short chain segments at the same concentration.

SAOS. Only in the case of rods with higher flexibility than those compared here, constraint release becomes important, as it was shown for carbon nanotubes [107].

Thus, flexibility mainly manifests itself at shorter timescales, where SAOS probes the particle undulation. The higher frequency crossover points in figure 5.2 reveal a significant difference between the two rod-like systems. The relaxation time of particle undulation significantly decreases with decreasing persistence length. This behavior was qualitatively predicted by Morse, but the measurements show that the widening of the elastic plateau region with increasing flexibility is more drastic than predicted. The values of τ_{flex} are between 1.1 and 2.5 s for different concentrations of the stiff mutant virus, fdY21M, while the range broadens strongly in the low frequency direction for different concentrations of fd wild-type, varying between 0.15 and 2.5 s, see higher frequency crossover points in figure 5.2.

An additional measurable relaxation time is that of particle undulation with a wave length significantly smaller than the contour length, τ_e, which marks the onset of equal slopes of $G'(\omega)$ and $G''(\omega)$, see figure 2.2. Although the

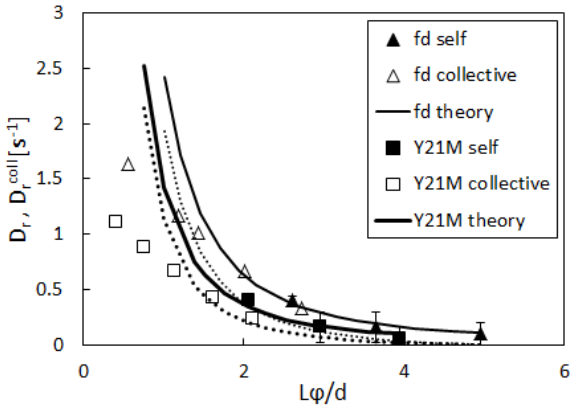

Figure 5.3: Measured rotational diffusion coefficients from crossover points (full symbols) versus scaled volume fraction for fd wild-type (L=0.88 μm, $L_p = 2.8$ μm) and fdY21M (L=0.91 μm, $L_p = 9.9$ μm) compared to collective rotational diffusion coefficients from scaling (open symbols). The full curves indicate the theoretical rotational diffusion coefficients, $\overline{D}_r$, from equation 2.70, the dotted curves show the theoretical collective rotational diffusion coefficient, from equation 2.62.

measurable frequency range terminates mostly only two or three points after this characteristic time, it can be deduced for most concentrations of both systems, see figure 5.4. From the difference in the shortest relaxation time, see figure 5.2, one can deduce the tube diameter via Morse theory. The tube diameter of fd wild-type is $D_{\text{tube}} \approx 0.3$ μm and for fdY21M one has $D_{\text{tube}} \approx 0.9$ μm, thus roughly confirming the difference in persistence length between the two rods.

5.3 Shear flow response

In this section, we apply our knowledge from chapter 4, namely that, due to our ignorance of higher order virials in the Fokker-Planck equation for rods, the tube model is needed to describe the observed zero shear viscosity and strong shear-thinning of our systems. By tailoring the length of rods, we are able to identify the prefactor, c, of the rotational diffusion coefficient, $\overline{D}_r$, in the tube model. This enables us to make quantitative predictions for many types of rod-like systems using equation 2.73. According to our knowledge, such an

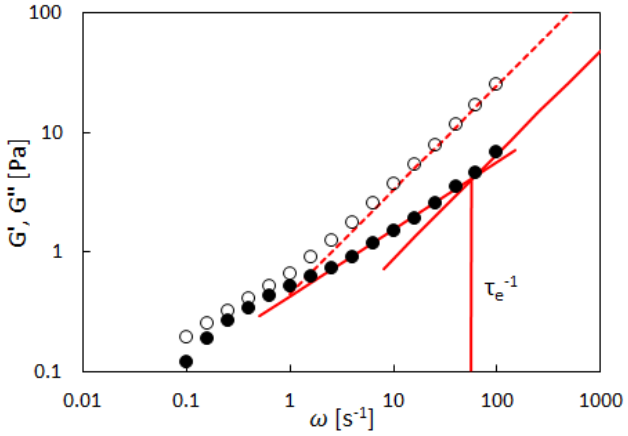

Figure 5.4: Illustration of the estimation for τ_e for fd virus (L=0.88 μm, $L_p = 2.8$ μm) at a concentration of 3.2 mg/ml in a glycerol buffer. The red lines are linear fits to the respective regions of the moduli curves. At the onset of equal slopes for G' and G'', the characteristic time of undulation with a wavelength shorter than the contour length, τ_e, is located.

experimental identification has not been accomplished before and is of high relevance also for industrial purposes.

The rod length of bacteriophages can be changed by bio-engineering, but a simultaneously L/L_p changes. This becomes obvious from table 3.1, where all material morphologies are listed: Despite the identical persistence lengths of fd wild-type, M13k07, Pf1, and M13-mini, the engineered change in length of course alters L/L_p. As L/L_p changes from M13-mini, $L/L_p \approx 0.11$, to Pf1, $L/L_p \approx 0.7$, the importance of constraint release processes in the rotational diffusion in equilibrium increases according to Odijk [104, 107]. Using Odijk's criterion, we can identify that all rods, except of Pf1 should diffuse according to the tube model. As Pf1 is in the Odijk regime, thus, constraint release becomes important. Under shear flow, tube dilation takes place, as indirectly demonstrated in chapter 4. This affects the Odijk criterion in the sense that the characteristic length scale changes from the tube size, D_{tube}, to the mean inter-particle distance, which depends on $\langle P_2 \rangle$ [175]. As we do not know the theoretical interdependence of these quantities, we need to test for the effect of bending rigidity, $L_P k_B T$, on the rheological behavior of rods to disentangle the effects of length and stiffness. For this reason, we compare again fd wild-type (L=0.88 μm, $L_p = 2.8$ μm) and fdY21M (L=0.91 μm, $L_p = 9.9$ μm) to study

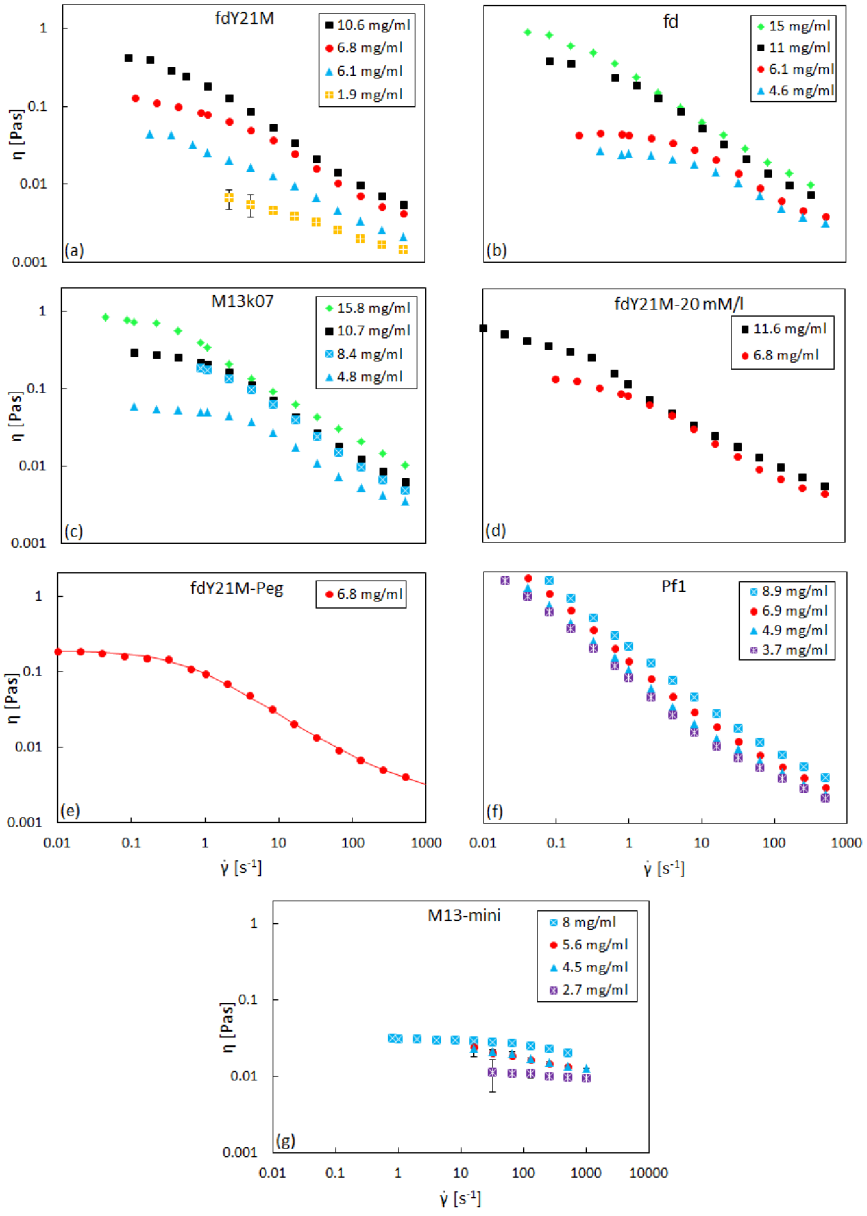

Figure 5.5: Viscosity as a function of shear-rate for different concentrations of (a) fd (L=0.88 μm, $L_p = 2.8$ μm), (b) fdY21M (L=0.91 μm, $L_p = 9.9$ μm), (c) M13k07 (L=1.2 μm, $L_p = 2.8$ μm), (d) fdY21M in 20 mM buffer, (e) peg-coated fdY21M, (f) Pf1 (L=1.96 μm, $L_p = 2.8$ μm), and (g) M13-mini (L=0.33 μm, $L_p = 2.8$ μm). The line in (e) is a fit with the Carreau model with $m = 0.66$ and $a = 2$.

the effect of flexibility on the shear flow behavior.

With this result in mind, we proceed to identify the length dependence of the nonlinear viscosity. The study reveals clear influences of flexibility and length on the behavior of particles under shear flow. Figure 5.5 shows the shear-thinning behavior as a function of concentration for all used bacteriophages. Similar concentrations are marked with the same color markers. Obviously, the shear-thinning behavior is general and none of the rods show peculiarities in their viscosity curves. From a comparison of figures 5.5(a) and (b), however, a difference in the measurable shear-rate range can be found. This difference is attributed to the disparity in torque certain systems induce on the rheometer. If the torque is too low, the transient flow behavior seemingly does not display a steady state, instead the measured torque decreases to 0 after the usual overshoot, shown in figure 3.3. This is due to the fact that the inbuilt torque sensor of the ARES-LS rheometer filters out the signal if its magnitude is comparable to that of the expected noise. Therefore, the low shear-rate data of certain systems have been discarded.

From a comparison of figures 5.5(a) and (f), it becomes clear that the zero shear viscosity can be measured for certain systems, while other systems are shear-thinning already at very low shear-rates. It is indicated that the length of the particle plays the most important role. While the zero shear viscosity is not measurable for the high aspect ratio rod, Pf1, see figure 5.5(f), it is measurable for the shortest rod, M13-mini, at highest concentration, see figure 5.5(g). Using the Carreau model, see red line in figure 5.5(c), we are nonetheless able to extract zero shear viscosities for all systems. In section 5.3.2, we show how to deduce the zero shear viscosity of all samples.

Furthermore, a difference in the shear-thinning parameter, n, can be found: the slope of the viscosity curve in the intermediate and high shear-rate regime seems to become steeper with increasing length. This is further analyzed in section 5.3.3.

5.3.1 Effect of stiffness on the nonlinear rheological response

Before we proceed with testing the effect of particle length on the shear-thinning behavior of rods, we need to identify the effect of particle flexibility, using the fd wild-type (L=0.88 μm, $L_p = 2.8$ μm) and the fdY21M (L=0.91 μm, $L_p = 9.9$ μm) virus suspended in aqueous Trizma buffer as well as glycerol/Trizma buffer, for which the bending rigidity, k_BTL_p, is strongly different, see figure 5.6. Clearly, the zero shear viscosity of the more flexible fd wild-type is lower than that of fdY21M. This seems not surprising since, due to its stiffness, the fdY21M should be able to form a more effective tube in the semidilute concentration

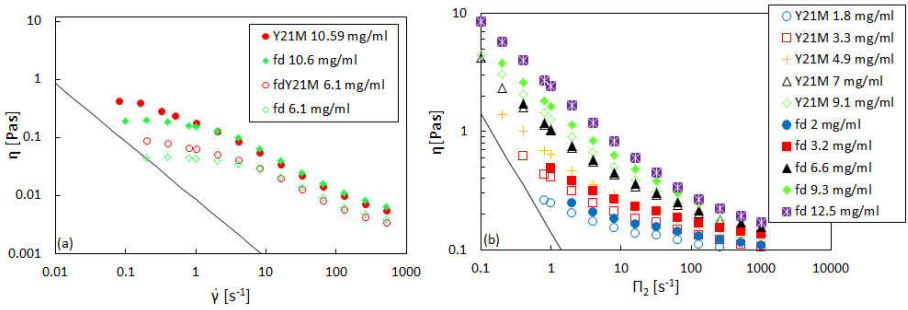

Figure 5.6: Viscosity as a function of shear-rate for two concentrations of fd wild-type (L=0.88 μm, $L_p = 2.8$ μm) and fdY21M (L=0.91 μm, $L_p = 9.9$ μm) in (a) aqueous Trizma buffer and (b) glycerol/Trizma buffer. Error bars are negligibly small.

regime, see [104]. The dynamic data confirm this assertion, see section 5.2. As the rotational dynamics of both rods are reasonably described by the tube model, the differences in the rotational diffusion coefficients, however, should be marginal. Nonetheless, our data suggest that the flexible species explores its tube more effectively than the stiffer species, thus reducing the stress at low shear-rates more effectively than the stiffer rod. An effect which we want to call constraint release here in accordance with the literature [176].

A further influence of particle flexibility can be observed in the intermediate to high shear-rate regime, where both systems undergo shear-thinning. Here, the curves of the two viruses cross over and the stiffer rod undergoes a slightly stronger shear-thinning than the flexible rod. This cannot be explained by tube dilation alone. If the effect of constraint release continued to be of importance at higher shear-rates, the non-linear viscosity of the flexible rod should be lower than that of the stiff rod.Therefore, we propose that our flexible particles undergo a morphological transition during flow. It was shown that semi-flexible rods like fd wild-type could form hairpins under steady shear flow, using actin, for which the persistence length is on the same order as the contour length [150]. This leads to a stronger reduction in viscosity for the stiff virus compared to its flexible counterpart, since the orientational ordering of hair-pin like objects is different from that of straight rods. This becomes even more evident from figure 5.6(b), where the rotational diffusion of both systems is strongly decreased due to the suspending medium. The differences in viscosity in the high shear-rate regime are of the same nature but seem to be even more pronounced compared to the watery system.

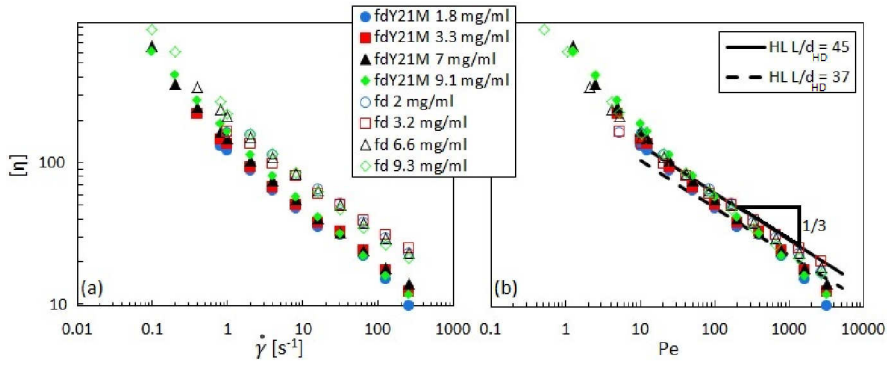

Figure 5.7: (a) Viscosity as a function of shear-rate and (b) Intrinsic viscosity as a function of the bare Peclet number, $Pe = \dot{\gamma}/D_r^0$, for fd (L=0.88 μm, L_p = 2.8 μm) and fdY21m (L=0.91 μm, L_p = 9.9 μm) virus at different concentrations in a glycerol-based buffer. The line shows the slope predicted by the theory of Hinch and Leal, equation 2.28, for the indicated hydrodynamic aspect ratios. Error bars are negligibly small.

In the high shear-rate regime, the theory by Hinch and Leal [75] predicts a certain slope of the viscosity curve. In figure 5.7, the shear viscosity data of fd virus and fdY21M suspended in a glycerol based buffer are shown. The scaling procedure for both, the viscosity, and the shear-rate, leads to a master curve for the two samples. The prediction by Hinch and Leal, comprising only hydrodynamic interactions of the rods, is in good agreement with the measurements in the high-shear-rate regime. The hydrodynamic radii of both systems can be deduced by fitting the theoretical curve to the experimental outcome. We find hydrodynamic aspect ratios of 45 for fd and 37 for fdY21M. Given the well known lengths of both systems, hydrodynamic thicknesses of 19.6 nm for fd and 24.6 nm for fdY21M can be found, significantly larger than the bare diameter of 6.6 nm. This can be attributed to hydrodynamic interactions decaying over a distance of roughly two particle diameters for aligned rods [156] in addition with a potentially large solvation layer of glycerol. In section 5.3.5, we show that this might also be related with the formation of hairpins for the flexible rods.

In summary, the flexibility does affect the zero shear viscosity as well as the infinite shear viscosity, but in opposite ways. Thus, when the length dependence is discussed in the next sections, this effect should be taken into account,

although it is relatively small. As for now, there is no theory available that quantitatively describes this effect.

5.3.2 Zero shear viscosity and morphological effects

From the raw data shown in figure 5.5, we can obtain the zero shear viscosity, following the two complementary procedures outlined in section 4.3.2. Either, we fit the Carreau model to the viscosity curve if the zero shear viscosity plateau can be measured, see, e.g., figure 5.5(e), or we use the Förster method [63], shifting the viscosity-orientational ordering curves by an apparent zero shear viscosity to create a concentration-independent master curve, see figure 5.8, in case the zero shear viscosity cannot be measured. With the use of both methods, the zero shear viscosities of all samples can be estimated.

The zero shear viscosity of rod-like colloids has the inverse particle length dependence of the rotational diffusion coefficient, see equation 2.76. In figure 5.9, the scaled zero shear viscosity is plotted as a function of the scaled volume fraction for different viruses. A monotonic increase of η_0 with increasing volume fraction is observed. In addition, a strong length dependence is observed, as theoretically predicted by the tube model, see equation 2.76.

The theoretical prediction fits the measurements well, except for small discrepancies in the low concentration regime. This is a clear indication that the tube model is capable of correctly predicting the strong length dependence of the rotational diffusion of rods with different morphologies. In general, a global fit of the measured data can be obtained with a prefactor of of $c = 2.7\text{x}10^3$ for $\overline{D}_r$, almost a factor 2 higher than the numerical prediction by Teraoka et al. [2]. In order to include morphological characteristics in the shown theoretical prediction, the prefactor, c, can be fitted to the individual curves with minimum standard deviations. The result of this operation is shown in figure 5.20(b), where the prefactor of the rotational diffusion coefficient is plotted as a function of effective particle stiffness. We can state that all rods are slender, as c is not thickness dependent. A small increase in c is found if we compare the prefactor of fd (third point from the left in figure 5.9(b)) with that of fdY21M (third point from the right in figure 5.9(b)), which could be interpreted as a hint that more flexible polymers are effectively experiencing a weaker entanglement than stiff rods do. This is physically intuitive, since a particle bending away from a geometric constraint can pass the constraint eventually, while a stiff particle cannot do so. An exception of the length dependence are the very short rodlike phages, which seem to diffuse very ineffectively despite their short contour length. One possible explanation for this observation is that the M13-mini system has not been cleaned from the reported DNA residuals, but only from

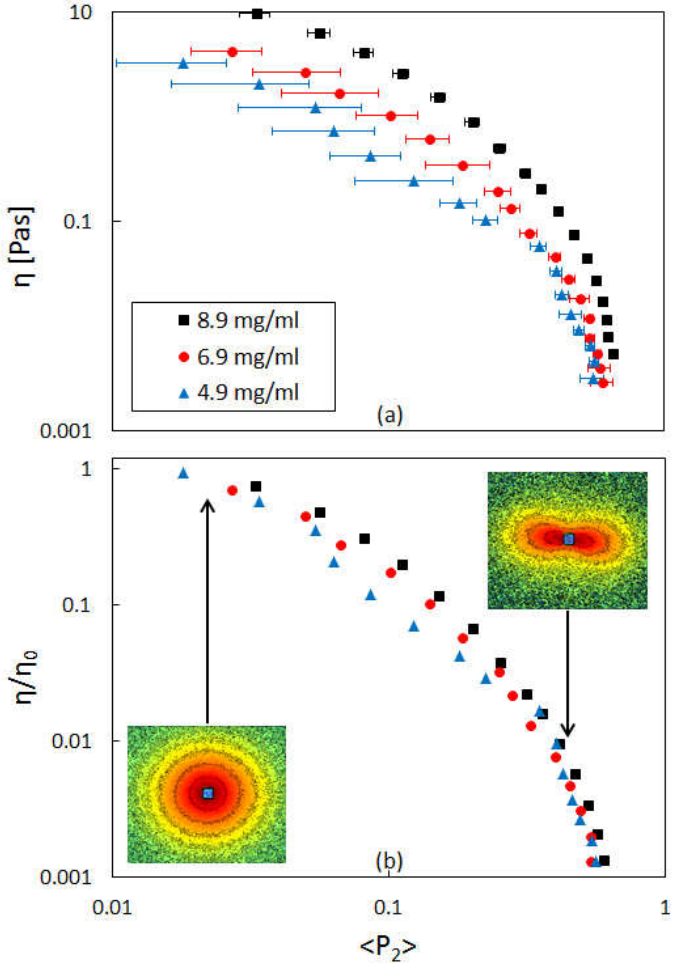

Figure 5.8: (a) Viscosity as a function of order parameter and (b) Scaled viscosity as a function of order parameter for Pf1 virus (L=1.96 μm, $L_p = 2.8$ μm) at different concentrations. The insets show scattering patterns at a shear-rate of 0.01 s^{-1} (lower inset) and 100 s^{-1} (higher inset).

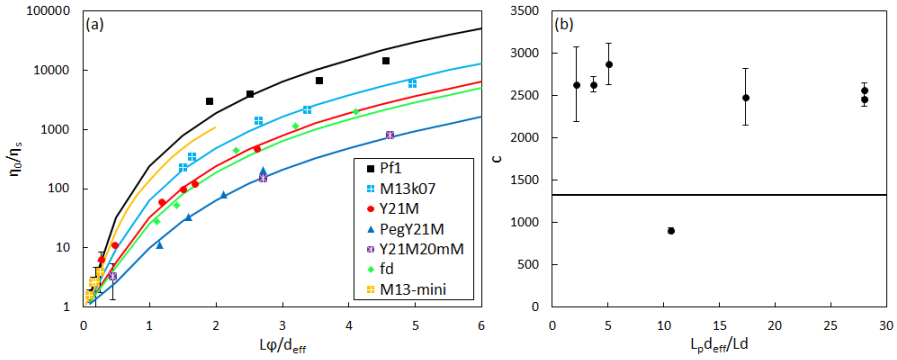

Figure 5.9: (a) Zero shear viscosity as a function of volume fraction for rods of different morphology. Lines represent the theoretical prediction, equation 2.76, with the prefactors, c, shown in (b). (b) Prefactor of the rotational diffusion coefficient as a function of L_p/L scaled with the effective particle thickness. The straight line in (b) represents a theoretical prediction by Teraoka et al. [2].

the spherically collapsed coat protein. So far, the measurements for M13-mini could not be repeated due to the instability of the phages.

5.3.3 Effects of length and thickness on the nonlinear rheological response

After clarification of the stiffness influences and the morphology dependent zero shear viscosity of rodlike colloids, the influences of length and thickness on the shear-thinning behavior can be discussed.

In figure 5.10, the shear-thinning behavior of all rod-like species used in this study are shown and compared at similar concentrations (compare to the overview of measurements in figure 5.5). It is obvious that, bearing in mind the influence of stiffness discussed earlier, the length of rods plays a significant role. As expected, an increase in contour length leads to an increase in the zero shear viscosity. For Pf1, which is by far the longest rod, the zero shear viscosity is not measurable but from the scaling procedure outlined in section 5.3.2, we know that it has much higher values than that of any other species. The shortest rod, M13-mini, on the other hand shows a comparatively small zero shear viscosity. Since flexibility counteracts the influence of length, the shear-thinning behavior of fdY21M and M13k07 is almost identical, despite the larger length of the latter

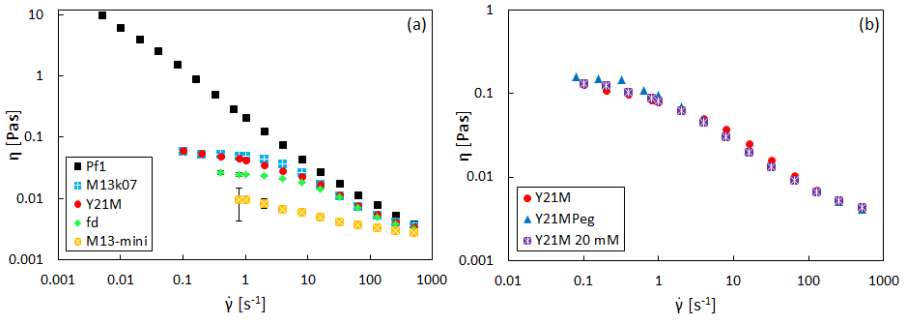

Figure 5.10: Viscosity as a function of shear-rate for (a): fd (L=0.88 μm, L_p = 2.8 μm), fdY21M (L=0.91 μm, L_p = 9.9 μm), M13k07 (L=1.2 μm, L_p = 2.8 μm), M13-mini (L=0.33 μm, L_p = 2.8 μm), and Pf1 (L=1.96 μm, L_p = 2.8 μm) at 4.8 mg/ml in an aqueous buffer and (b) fdY21M (d = 6.6 nm) and its thicker derivatives (d = 17 nm) at 6.8 mg/ml in the same buffer.

species. Only at intermediate shear-rates, M13k07 shows a higher viscosity compared to the shorter rod. This, again, points in the direction of excluded volume playing a decisive role in the intermediate to high shear-rate regime. Since the more flexible rod M13k07 takes up a higher volume fraction before the enhanced tube dilation mechanism due to its 20% larger length acts, the viscosity at these shear-rates remains slightly higher than that of the the stiffer rod fdY21M.

In contrast to the zero shear viscosity, the shear-thinning parameter decreases with increasing contour length, as briefly mentioned before section 5.3.1. Both quantities, as extracted from figure 5.10, are shown as a function of contour length in figure 5.16. While m decreases monotonically, the zero shear viscosity of the ideal rod, of course, does not follow the trend observed for the viruses with identical persistence lengths. Generally, however, an increase in contour length increases the zero shear viscosity, as discussed before. With an aspect ratio of 187, the long virus Pf1 has by far the lowest shear-thinning coefficient. For coefficients in this range, shear banding becomes likely. Therefore, we test for gradient shear banding in section 5.7.

Figure 5.10(b) highlights the influence of thickness on the flow behavior under steady state shear. The zero shear viscosity of both thicker samples is higher than that of the bare fdY21M, while the curves cross at intermediate shear-rates such that the viscosity of the thicker samples is lower than that of the bare virus in this regime. At even higher shear-rates, the viscosities of all three samples

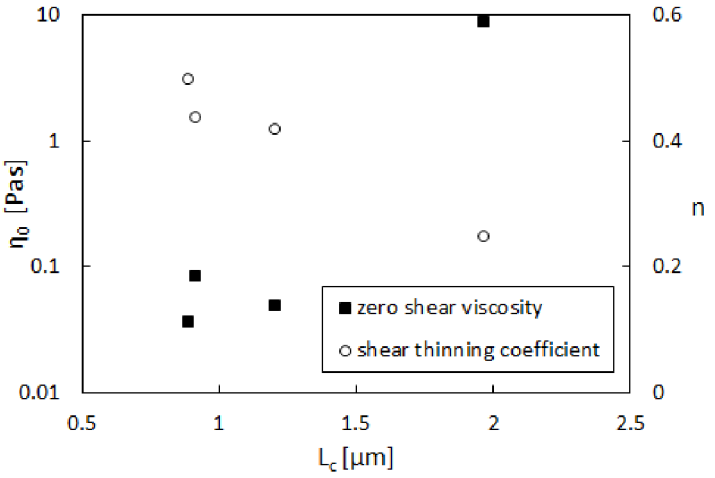

Figure 5.11: Zero shear viscosity and shear-thinning parameter as a function of contour length for fd (L=0.88 μm, L_p = 2.8 μm), fdY21M (L=0.91 μm, L_p = 9.9 μm), M13k07 (L=1.2 μm, L_p = 2.8 μm), and Pf1 (L=1.96 μm, L_p = 2.8 μm) in an aqueous buffer with a concentration of 4.8 mg/ml. Error bars are vanishingly small.

are identical. Differences between the shear-thinning behavior of viruses with different thicknesses are exceedingly small as compared to the effect of the rod length predicted by the tube model. Hence, all systems are in the slender rod limit. For aspect ratios such as those of our viruses, between $54 \leq L/d_{\text{eff}} \leq 87$, we propose that the thickness influence on the rheological behavior can be neglected.

5.3.4 Scaling and comparison

To show the importance of the collective slowing down of particle dynamics towards the IN transition, as predicted by Dhont and Briels, we scale down the shear-rate using the effective Peclet number, $Pe_{\text{eff}} = \dot{\gamma}/\overline{D}_r(1 - \varphi L/4d)$. This reflects the balance between Brownian motion and shear flow and shows that the flow behavior is independent of the volume fraction of rods. For every species, the viscosity curves for different concentrations of the suspension can be shifted to a single master-curve using this scaling. In figure 5.3, we compare the resulting collective rotational diffusivities with the rotational self-diffusion

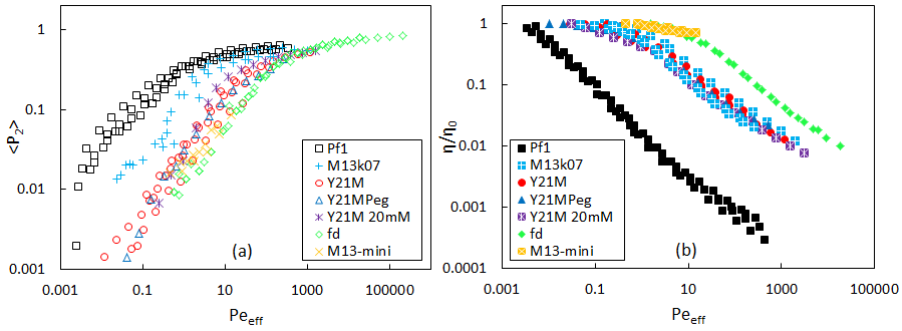

Figure 5.12: (a) Order parameter and (b) scaled shear viscosity as a function of effective Peclet number for all virus systems and all concentrations (different concentrations of the same species are plotted with identical markers). Error bars are omitted for reasons of readability.

coefficients obtained from SAOS. Similar values of both quantities are found for intermediate concentrations. Additionally, we can use the theoretically calculated rotational self-diffusion coefficients, $\overline{D}_r$, evaluating equation 2.70 with the prefactor $c = 2.7\text{x}10^3$, and use the scaling to find the upper isotropic-to-nematic spinodal points, φ_{IN}, for all systems. Table 5.1 list all experimental values for the isotropic binodals, φ_I, as well as the spinodals, φ_{IN}. The result for fd wild-type is in accordance with measurements by Ripoll et al. [**?**].

As illustrated by the ideal rod in figure 4.8, the shear-thinning behavior is caused first and foremost by orientational ordering of the rods. The steepest increase of orientational ordering could be expected at a Peclet number of 1, where rotational diffusion is overcome by shear induced flow alignment. The morphology, however, has a significant effect on the onset of shear-thinning. As presented in figure 5.12(a), the longer bacteriophages, Pf1 and M13k07, start to orient already around a Peclet number of 0.1, while the smallest rods, M13-mini, start orienting around a Peclet number of 5. One can, therefore, conclude that an increase in length decreases the onset Peclet number of shear-thinning.

In figure 5.12(b), it is seen that the curves for phages of different thickness display identical onset of shear-thinning. This is interesting, since, on the one hand, the zero shear viscosities of these species are different due to the decrease in tube diameter with increasing thickness. On the other hand, the shear-thinning of the thicker viruses is slightly stronger than the shear-thinning of the thinner virus, see figure 5.10(b). Those two aspects combined, again,

reflect the influence of tube dilation on the flow behavior.

Table 5.1: Scaled isotropic binodals from birefringence measurements and upper isotropic-to-nematic spinodal points from scaling the viscosities and order parameters in figure 5.12.

virus	$L\varphi_I/d_{\text{eff}}$	$L\varphi_{IN}/d_{\text{eff}}$
fd	4.61	5.8
fdY21M	3.4	4.3
fdY21M peg	4.63	6.5
M13k07	5.62	6.5
M13-mini	3.7	4.9
Pf1	8.37	9.8

The fact that the curves of fd virus and fdY21M in figure 5.12 do not overlap exemplifies the influence of flexibility on the shear-thinning behavior. This is also seen from the overlapping of fdY21M and M13k07 in figure 5.10(b). One can conclude that increasing flexibility increases the onset Peclet number of shear-thinning. Length and flexibility, therefore, are two counter-playing influences on the shear-thinning behavior of rods. This is also reflected in the zero shear viscosities of the different species by comparison of figures 5.5 and 5.10(a), as discussed above.

Since all species experience the same moderate orientational ordering with concomitant strong shear-thinning, the theoretical prediction suffers from the same discrepancies as illustrated for the ideal rod in figure 4.12. However, despite the neglect of flexibility, the theoretical approach, using equation 2.90, covers the length dependence of the shear-thinning behavior well, see figure 5.13[1]. Also the prediction of the order parameter agrees better with the measured values for longer particles as compared to shorter ones. An important aspect is the inclusion of shear-induced tube dilation, equation 2.72, which enables us to almost fully understand the shear-thinning behavior of rodlike particles.

5.3.5 Effect of particle stiffness on the biaxiality of the orientational ordering tensor

As for now, all order parameters shown in chapter 5 are measured in the flow-vorticity plane. Similar to the orientational ordering of the ideal virus, presented in section 4.3.2, also the orientational ordering of non-ideal rods should be biaxial.

[1] It is important to remember that the scaling of the shear-rate with the collective rotational diffusion coefficient from equation 2.62 leads to a single master curve, independent of the concentration of particles, for both the theoretical predictions as well as the measured data.

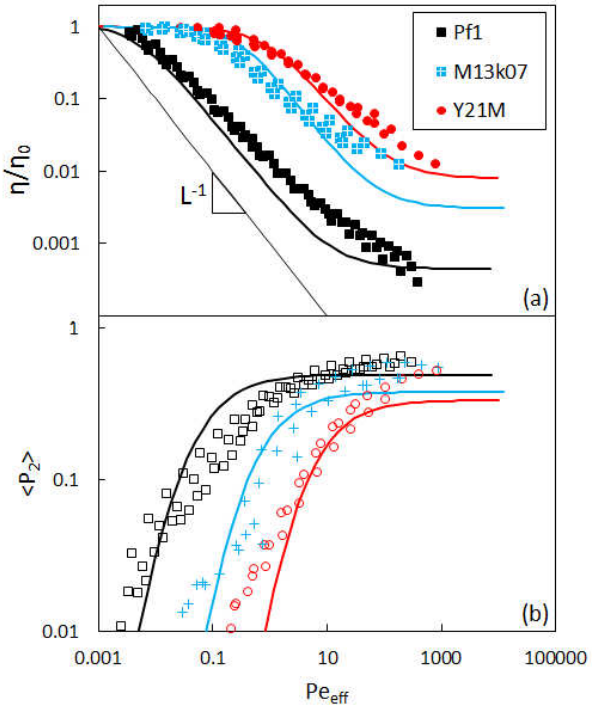

Figure 5.13: (a) Scaled shear viscosity and (b) order parameter as a function of effective Peclet number for: Pf1 ($L = 1.96$ μm), M13k07 ($L = 1.2$ μm), and fdY21M ($L = 0.91$ μm), at all measured concentrations (plotted with identical markers). The lines are predictions from the newly developed theory, equation 2.90, using $\langle D_r \rangle$ from equation 2.72 with the experimental prefactor $c = 2700$. The thin line displays an L^{-1} dependence of the nonlinear viscosity, indicative of shear banding. Error bars are omitted for reasons of readability.

The biaxiality, $\mathcal{T}$, results from the identical symmetries of the stress tensor in planar Couette flow and the orientational ordering tensor and was predicted by Dhont-Briels theory even for ideal, uniaxial rods. Measurements for the ideal rod, fdY21M, suggest on the contrary that the orientational ordering in gradient and vorticity direction is almost identical at low and intermediate shear-rates, showing even the inverse symmetry of the stress tensor at an effective Peclet number of 5. Only at high Peclet numbers, the theoretically predicted symmetry conditions seem to apply. In this section, we focus on the effect of particle flexibility on the biaxiality.

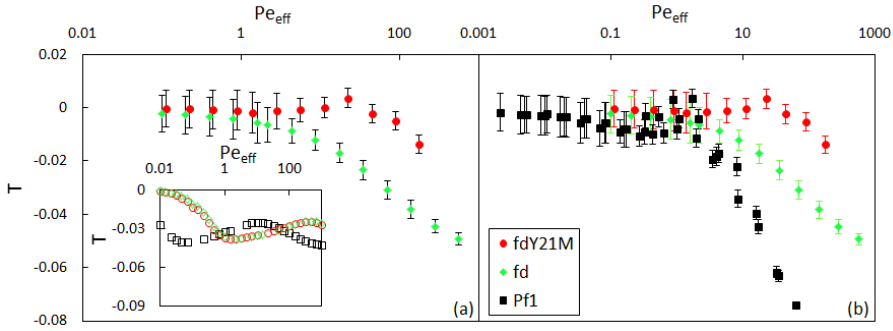

Figure 5.14: Biaxiality as a function of the effective Peclet number for (a) fdY21M (L=0.91 μm, $L_p = 9.9$ μm) at a concentration of 12.6 mg/ml and fd (L=0.88 μm, $L_p = 2.8$ μm) at a concentration of 20 mg/ml and (b) fdY21M and fd at the same concentrations as in (a) and Pf1 virus at 8.9, 6.9, and 4.9 mg/ml, all with identical symbols. The inset in (a) shows theoretical predictions from equation 2.59 at the same concentrations as the measurements in (b).

Figure 5.14(a) compares the biaxiality of the ideal virus, fdY21M, and the flexible, but similarly long fd virus, both at high concentrations. In contrast to our observations for ideal rods, the biaxiality of fd virus is an ever increasing function of the effective Peclet number. Thus, also no sign reversal of $\mathcal{T}$ at intermediate Peclet numbers is found. This points in the direction of a different stress relaxation behavior of the two species, resulting from different conformations under shear flow. At high shear-rates, the flexible system is strongly biaxial with a biaxiality which is even higher than predicted, compare the maximum value of $\mathcal{T}$ for fd in figure 5.14(b) with that of the inset. This could be an indication that the flexible systems not only does not follow the symmetry of the flow field, but furthermore undergoes a structural change at high Peclet numbers. We assume that the achieved state is a bent conformation of rods, called hairpins. Due to the form of the hairpin and the experimentally observed orientational ordering of hairpins in shear flow [150, 177], the orientational ordering of strongly bent rods in the gradient direction becomes significantly higher compared to that in the vorticity direction. The orientational ordering of rods and hairpins is schematically shown in figure 5.15. An even stronger biaxiality at high shear-rates is observed for the very long and Pf1 virus, see figure 5.14(b). As the behavior stands in marked contrast to the theoretical prediction, see the inset of figure 5.14(a), we conclude that also in the case of Pf1, hairpin formation takes place under shear flow. Interestingly, Pf1 shows a sign change of the biaxiality around $Pe_{\text{eff}} \approx 1$, similar to the ideal rod, fdY21M, but

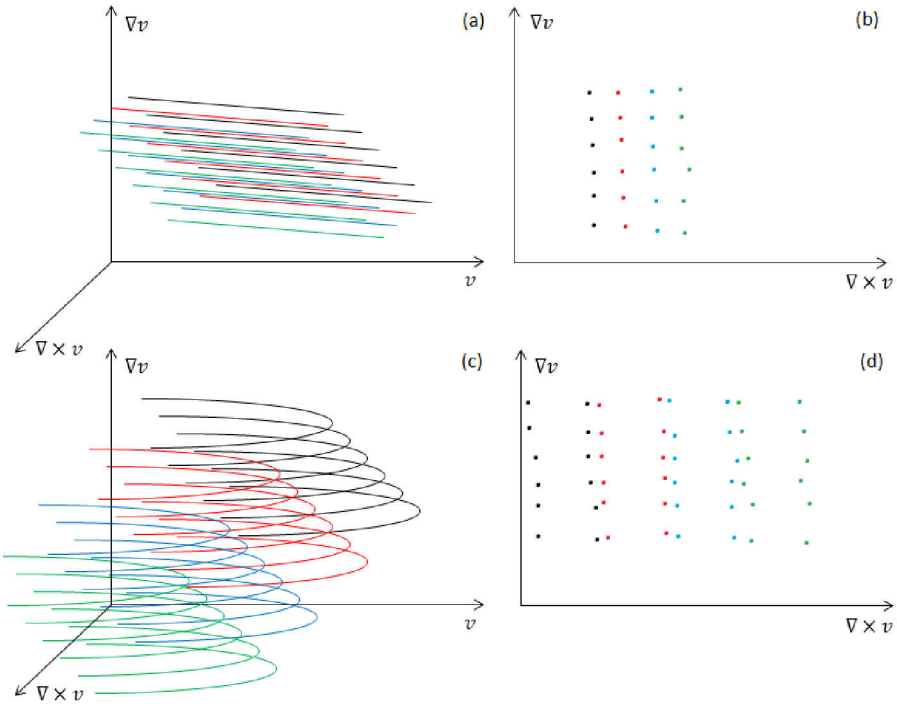

Figure 5.15: Schematic orientational ordering of ideal rods (a) and (b) as compared to hairpins (c) and (d) in the experimental reference frame.

at lower shear-rates. As for now, no clear interpretation of the non-monotonic curve forms can be given. However, we interpret the results in the following way: We conclude from our experiments that the observed high biaxialities in flexible systems originate from morphological changes of the constituent particles. This assertion could be supported by laser confocal microscopy studies of viruses in shear flow, similar to those of F-actin [150]. A limiting factor for the feasibility of such measurements, however, is the relatively small size of the viruses.

5.4 Effects of stiffness on the extensional viscosity

Using capillary breakup extensional rheometry, the apparent extensional viscosity of both fd wild-type (L=0.88 μm, L_p = 2.8 μm) and fdY21M

(L=0.91 μm, L_p = 9.9 μm) was measured. Figure 5.16 shows a comparison between the shear and extensional viscosity as a function of the square root of the second invariant of the rate of deformation tensor, $\sqrt{|\mathrm{II}_{2D}|} = \dot{\gamma} = \sqrt{3}\dot{\epsilon}$, for both of these systems suspended in a glycerol based buffer.

It is obvious that the rod with the higher bending rigidity, fdY21M, has a higher elongational viscosity than its flexible counterpart, fd, at all measured concentrations. This is the opposite of what is observed for the shear viscosity and it probably can be attributed to the particle conformation in the different flow fields. While an applied shear field allows for flexible rods to assume a strongly bent, so-called, hairpin structure [?, 150], this is not as likely in an extensional field, as theoretically predicted, among others, by Morse [?] and confirmed by experiments on actin [178]. A hint for for full stretching of flexible particles in a biaxial elongational flow field is shown in in the AFM pictures, see figures 4.2 and 4.3. Although this observation is not in-situ, the differences between the rheological responses could be explained if the flexible rods indeed get stretched in elongational flow and form hairpins in shear flow. Hairpin formation in shear flow is a phenomenon leading to a complicated stress release of the sample, permitting less shear-thinning as compared to a stiff system, but simultaneously promoting strain softening. In section 5.3.5, we give evidence that, indeed, flexible systems are prone to hairpin formation.

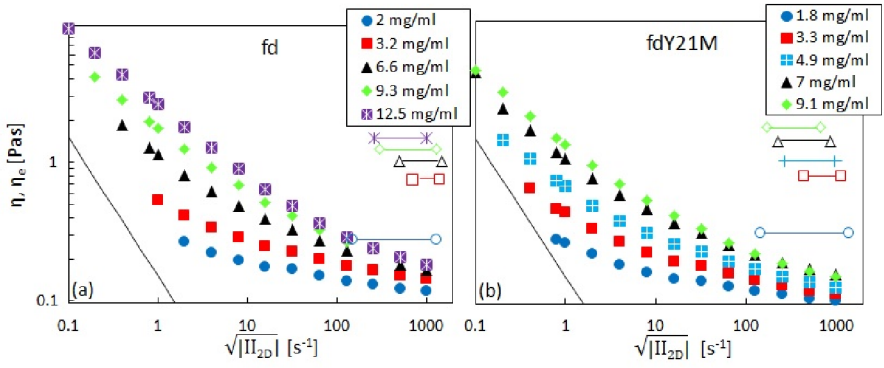

Figure 5.16: Shear (full symbols) and elongational viscosity (open symbols) as a function of the square root of the second invariant of the rate of deformation tensor for (a) fd (L=0.88 μm, L_p = 2.8 μm) and (b) fdY21M (L=0.91 μm, L_p = 9.9 μm) at different concentrations in a glycerol-based buffer. The thin inclined line marks the torque limit of the rheometer. Error bars are negligibly small.

While the zero shear viscosity of the stiff fdY21M virus is higher than that of

its flexible counterpart, fd, the conformational change during steady shear flow leads to a stronger shear-thinning of the flexible species, while in extensional flow, the conformation of both rods is straightened. Still, the initially stiffer rods seem to order even more than the flexible ones, leading to a higher extensional viscosity of the stiff system in the high extension rate regime probed by CaBER.

A comparison of the elongational viscosities of the two systems as a function of concentration is shown in figure 5.27. In comparison with the theories of Batchelor [74] and Shaqfeh and Fredrickson [82], hydrodynamic diameters of 25.1 nm for fd and 21.7 nm for fdY21M can be found. Thus, the hydrodynamic radius of the stiff rods under extensional flow is roughly the same as that obtained from steady shear data, while that of fd wild type is larger.

The overshoot viscosity, obtained from the overshoot stress, see figure 3.3, follows the same trend as the elongational viscosity, see figure 5.17(b). This points in the direction that, indeed, the response to the two flow fields is drastically different in terms of the molecule dynamics. Here, additional rheo-SANS measurements would be required to shed light on the orientational ordering during the stress overshoot as well as under elongational flow.

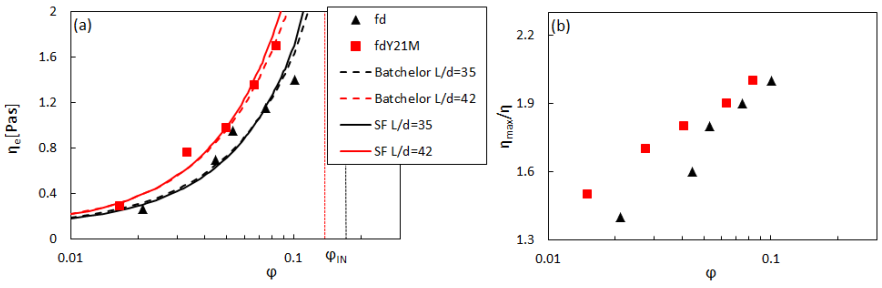

Figure 5.17: (a) Elongational viscosity and (b) scaled overshoot viscosity as a function of the relative volume fraction of particles for fd (L=0.88 μm, L_p = 2.8 μm) and fdY21M (L=0.91 μm, L_p = 9.9 μm) virus in a glycerol-based buffer. Lines are predictions from the theory of Batchelor (dashed) and Shaqfeh and Fredricksen (full) with the given hydrodynamic aspect ratios. The vertical lines mark the isotropic spinodal points for both samples. Error bars are negligibly small.

The Trouton ratio as a function of the square root of the second invariant of the rate of strain tensor is shown in figure 5.18. Despite the small normal stress differences (usually not measurable in our rheometer setup), we obtain relatively large Trouton ratios for both samples, comparable to those for e.g. polystyrene

solutions with similar concentrations [179]. The Trouton ratios of the stiffer system are especially pronounced due to the high elongational viscosities.

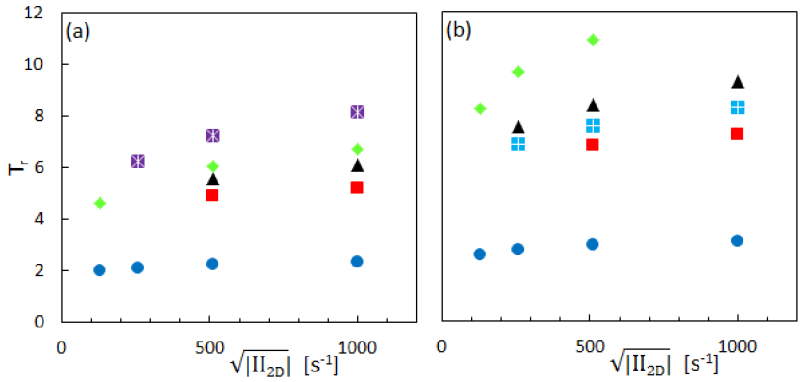

Figure 5.18: Trouton ratio as a function of the square root of the second invariant of the rate of deformation tensor for different concentrations of (a) fd (L=0.88 μm, $L_p = 2.8$ μm) and (b) fdY21M (L=0.91 μm, $L_p = 9.9$ μm) in a glycerol-based buffer. Legend, see figure 5.16. Error bars are negligibly small.

5.5 Relaxation after cessation of flow

As mentioned in sections 2.7 and 5.3.4, the dynamics of rods in equilibrium and shear flow are not the same. In particular, tube dilation starts to play a significant role. The influence of tube dilation can be studied by cessation of flow experiments, where the relaxation of the orientational ordering after cessation of a pre shear-rate,$\dot{\gamma}_{\text{pre}}$, is followed. In such an experiment, we can freely choose $\dot{\gamma}_{\text{pre}}$, for which we know from preceding measurements that the corresponding equilibrium order parameter is low, such that the tube is not dilated. Subsequently, we use higher values of $\dot{\gamma}_{\text{pre}}$, such that the tube becomes dilated. In this section, we focus on the relaxation dynamics of Pf1 at relatively high concentrations because the effect of dilation is expected to be strong, while the relaxation dynamics are expected to be slow, due to the length of Pf1, such that it can be followed by rheo-SANS. The relaxation of the order parameter of the flexible Pf1 virus with time after cessation of flow with a very low applied shear-rate is shown in figure 5.19.

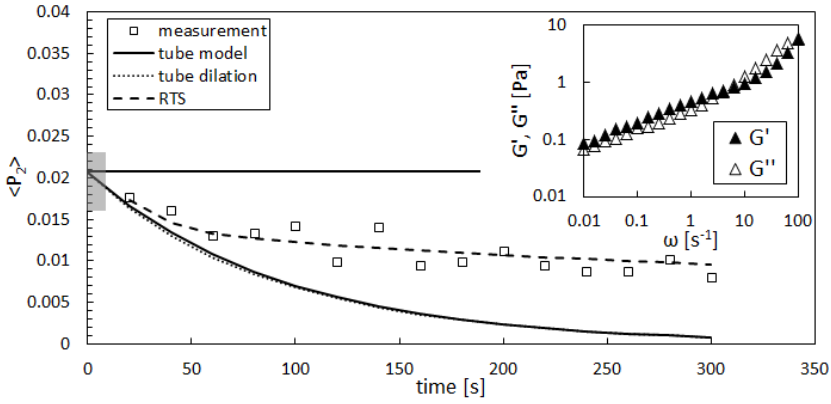

Figure 5.19: Order parameter versus time for Pf1 virus (L=1.96 μm, L_p = 2.8 μm) at a concentration of 8.8 mg/ml in an aqueous buffer after cessation of shear from $\dot{\gamma}_{\mathrm{pre}} = 10^{-3}$ s^{-1}. The horizontal line indicates the value of $\langle P_2 \rangle$ at constant shear and the shaded area at the ordinate its standard deviation. Theoretical predictions differ in the diffusion coefficient: $D_r^{\mathrm{coll}} \sim \overline{D}_r$ (full), $D_r^{\mathrm{coll}} \sim \langle D_r \rangle$ (dotted). The stretch-dashed line shows a fit involving an assumed relaxation time spectrum (RTS), equation 5.1. Inset: Complex moduli of Pf1 vs. frequency at a concentration of 8.8 mg/ml in the same buffer.

We identify a significant discrepancy between the measurement and the theoretical predictions using just one single rotational diffusion coefficient. The full curve corresponds to relaxation with a strongly hindered diffusion coefficient $D_r^{\mathrm{coll}} = \overline{D}_r \left(1 - L\varphi/5d\right) = cD_r^0 \left(1 - L\varphi/5d\right) \left(\nu L^3\right)^{-2}$ and the dashed line corresponds to a relaxation with a prefactor $\langle D_r \rangle$ for D_r^{coll}, depending on the orientational ordering tensor at a given time. Both processes are modeled with an exponential decrease of the order parameter: $\langle P_2 \rangle(t) = \langle P_2 \rangle(0) \exp\left[-6D_r^{\mathrm{coll}} t\right]$ [168, 180]. The value $\langle P_2 \rangle(0)$ is indicated by the horizontal line. It is seen that the predicted relaxation with either diffusion coefficient is much faster compared to the observation. The situation, however, reverses for higher applied shear-rates and corresponding higher initial orientational ordering, as shown in figure 5.20:

The theoretical prediction including tube dilation, dashed lines in figure 5.20, is found a little closer to the measurement than the prediction involving $\overline{D}_r$, but still differs strongly from the observed behavior. This can be taken as an indication that shear induced tube dilation plays a much more significant role than assumed theoretically. In figure 5.19, corresponding to cessation

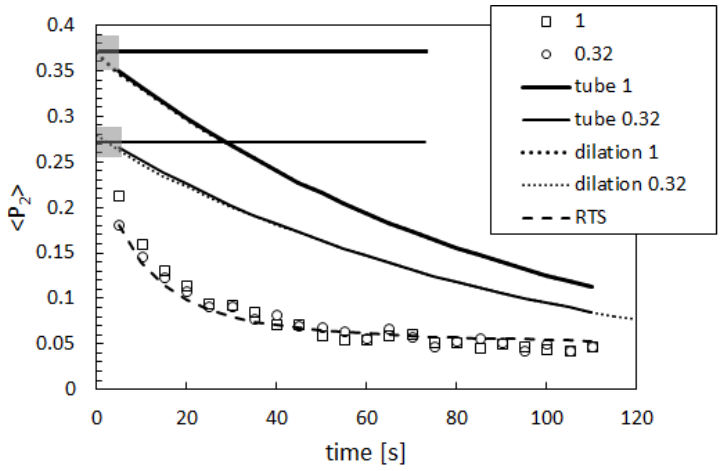

Figure 5.20: Order parameter versus time for Pf1 virus (L=1.96 μm, L_p = 2.8 μm) at a concentration of 8.8 mg/ml in an aqueous buffer after cessation of shear from $\dot{\gamma}_{\rm pre} = 1$ and $\dot{\gamma}_{\rm pre} = 0.32$ s^{-1}. The straight lines indicate the values of $\langle P_2 \rangle$ at constant shear and the shaded areas their standard deviations. Theoretical predictions differ in the diffusion coefficient: $D_r^{\rm coll} \sim \overline{D}_r$ (full), $D_r^{\rm coll} \sim \langle D_r \rangle$ (dotted). The stretched-dashed line shows a fit of equation 5.1.

of flow after very low shear, the tube is hardly dilated, while in figure 5.20, corresponding to intermediate shear-rates, the tube is strongly dilated. One can observe that the two measured curves in figure 5.20 show almost identical relaxation behavior, although corresponding to different values of $\langle P_2 \rangle(0)$. This indicates that tube dilation already sets in at relatively low shear-rates and for shear-rates for which it starts to play an important role, the tube is effectively destroyed by the prior shear flow.

In addition to the theoretical predictions using just one single relaxation time, the stretched-dashed lines in figures 5.19 and 5.20 show a theoretical prediction assuming an underlying relaxation time spectrum, in the spirit of the theory of Morse, see equation 5.1. The inset of figure 5.19 shows the characteristically wide elastic region appearing in linear viscoelastic measurements due to the relatively short characteristic time of particle undulation, $\tau_{\rm flex}$, of these phages. As compared to, e.g., fd virus, $\tau_{\rm flex}$ of Pf1 virus is roughly halved, corresponding to an increase of the width of the elastic region of roughly a decade in direction of higher frequencies. The reason for assuming a spectrum of relaxation times becomes obvious from figure 5.21, where the content of figure 5.19 is plotted in a

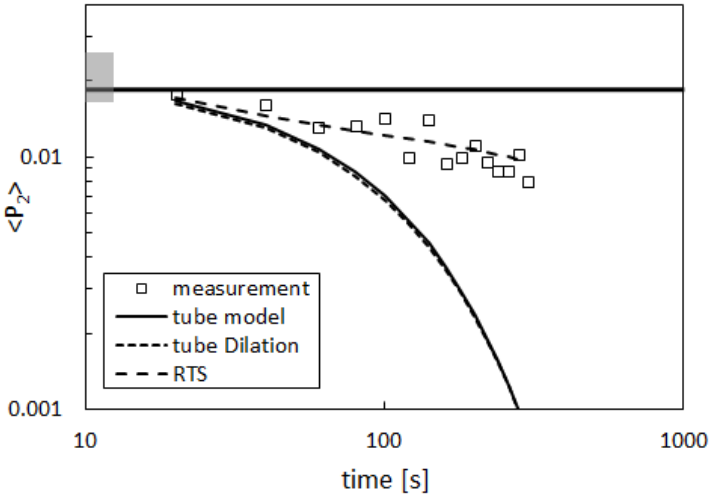

Figure 5.21: Logarithmized order parameter versus time for Pf1 virus (L=1.96 μm, L_p = 2.8 μm) at a concentration of 8.8 mg/ml in an aqueous buffer after cessation of shear from $\dot{\gamma}_{\text{pre}} = 10^{-3}$ s^{-1}. The straight line indicates the value of $\langle P_2 \rangle$ at constant shear and the shaded area its standard deviation. Theoretical predictions differ in the diffusion coefficient: $D_r^{\text{coll}} \sim \overline{D}_r$ (full), $D_r^{\text{coll}} \sim \langle D_r \rangle$ (dotted). The stretch-dashed line shows a fit of equation 5.1.

double logarithmic fashion. Clearly, the prediction using a single relaxation time diverges strongly from the measurement, similar to the case of polymers, seen, e.g., in figure 5 of reference [181]. This suggests that the addition of multiple relaxation times with similar exponential behavior is needed for reproducing the observed relaxation curve. In particular, one could construct a RTS for rodlike polymers in the same manner as for flexible polymers, such that:

$$\langle P_2 \rangle(t) = \frac{1}{N} \langle P_2 \rangle(0) \sum_{i=1}^{N} \langle P_2 \rangle_i \exp\left[-t/\tau_i\right] \quad . \tag{5.1}$$

Here, however, as opposed to the usual definition, the RTS is composed of orientational order parameters, such that a set of order parameters and relaxation times, $\{\langle P_2 \rangle_i, \tau_i\}$, is taken into account instead of a set of relaxation strengths g_i and their corresponding times. The resulting RTS for Pf1 without tube dilation is shown in figure 5.22(a), where a total number of 5 relaxation modes was used. For a better data visualization and different from the times

shown in figure 2.2(b), the relaxation time of normal diffusion, $\tau_{\parallel}$, has been used here as well, such that $\tau_{\mathrm{end}} > \tau_{\mathrm{r}} > \tau_{\mathrm{flex}} > \tau_{\mathrm{e}} > \tau_{\parallel}$.

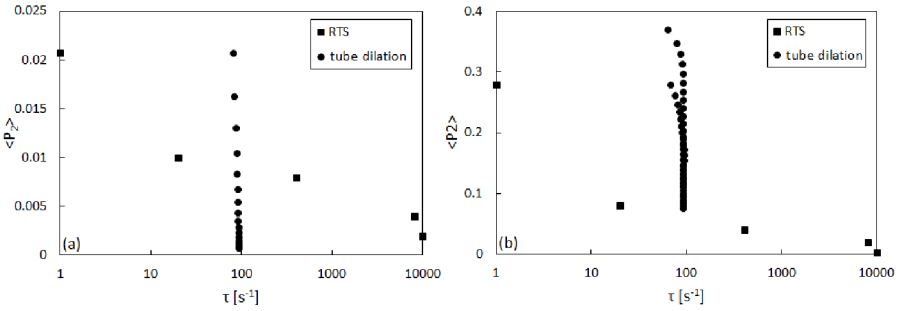

Figure 5.22: (a) Relaxation time spectrum of Pf1 (L=1.96 μm, $L_p = 2.8$ μm) at a concentration of 8.8 mg/ml in an aqueous buffer from equation 5.1 for $\dot{\gamma}_{\mathrm{pre}} = 0.001\ \mathrm{s}^{-1}$. Dots show the distribution of relaxation times for $D_r^{\mathrm{coll}} \sim \langle D_r \rangle$ (tube dilation). (b) RTS for $\dot{\gamma}_{\mathrm{pre}} = 0.32$ and $\dot{\gamma}_{\mathrm{pre}} = 1\ \mathrm{s}^{-1}$ from equation 5.1. The broader dotted RTS corresponds to $\dot{\gamma}_{\mathrm{pre}} = 1\ \mathrm{s}^{-1}$, the narrow one to $\dot{\gamma}_{\mathrm{pre}} = 0.32\ \mathrm{s}^{-1}$.

It is seen that the theoretical prediction using tube dilation also leads to a relaxation time spectrum. However, this spectrum is very narrow compared to the RTS inferred from the measurement. Since the applied shear-rate prior to cessation of flow for the experiment shown in figure 5.19 is low, one can assume that shear-induced tube dilation does not play a significant role. Therefore, the spreading of relaxation times can be compared to the observed relaxation times in linear rheometric experiments. For very short times, one can identify a region with relatively steep decrease of ordering which seems to cross over to a region of almost constant $\langle P_2 \rangle$. At long times, the reduction of ordering becomes stronger again. The shortest observable timescale in figure 5.22(a) could correspond to the ultra-short time unconstrained relaxation of particle undulations with a wavelength much smaller than the particle contour length inside the tube. At intermediate times, undulations inside the strongly confining tube are used to reduce the orientational ordering. At long times, the rotational diffusion is still reduced compared to the short time diffusion, but due to reptation and subsequent rotation, a decrease in orientational ordering can be achieved. We indicate this using a comparison to the RTS of the dilated sample, shown in figure 5.22(b). The dilated sample shows a slightly broader region of strong orientational equilibration at short relaxation times. The distortion of the tube due to the higher value of $\dot{\gamma}_{\mathrm{pre}}$ could lead to the fact that the reduction of

orientation via undulation plays a negligible role in the overall diffusion process. Therefore, the plateau region of the RTS disappears.

In summary, for modest and strong shear flows, tube dilation is exemplified as the main phenomenon determining the non-equilibrium dynamics of rods. This underlines the conclusions drawn in section 5.3.4. In order to gain further insight into the signatures of tube dilation, however, studies of the dynamics of rods under shear flow in a real time experiment, such as confocal laser microscopy, would be needed. Only for very weak flows, the full RTS plays a role for the particle dynamics.

5.6 Rheology of polydisperse suspensions

Naturally, all rodlike polymer suspensions possess a certain degree of polydispersity with only a few exceptions, such as the viruses used in this work. Also, most industrially used rod-like systems are polydisperse. In order to understand the effect of polydispersity on the shear-thinning behavior, one has to develop mixing rules for the rheometric quantities. Before developing a mixing rule, we used our library of rods to find the prefactor, c, of the rotational diffusion coefficient in the tube model, $\overline{D}_r = cD_r^0 \left(\nu L^3\right)^{-2}$, in section 5.3.2. Here, we apply our knowledge to make a quantitative prediction for a bidisperse system of rods, where only two species of different length are present in the mixture. This is a proper starting point for the development of a mixing rule for polydisperse systems. Here, Pf1 virus (L=1.96 μm, $L_p = 2.8$ μm) is mixed with fd virus (L=0.88 μm, $L_p = 2.8$ μm). It is shown in figure 5.13 that the shear viscosity of both species is well-understood. For this reason, the mixture may be used as a benchmark system for polydisperse semiflexible polymers for which $L < L_p$.

5.6.1 Zero shear viscosity of bidisperse samples

The two species are mixed according to their volume fractions: $\varphi^{(m)} = \varphi^{(fd)}(1-\rho) + \varphi^{(pf1)}\rho$, such that the overall volume fraction of rods in the suspension remains constant. Then, steady shear is applied to the systems. The chosen concentration of rods, thereby, needs to be high enough to assure that the zero shear viscosity can be estimated from the measured data via the Carreau fitting approach. This requires enough torque for a measurable signal at low shear-rates. In figure 5.23, the zero shear viscosities of the mixtures are plotted as a function of the relative volume fraction, $\rho = (\varphi^{(m)} - \varphi^{(fd)}/(\varphi^{(pf1)} - \varphi^{(fd)})$.

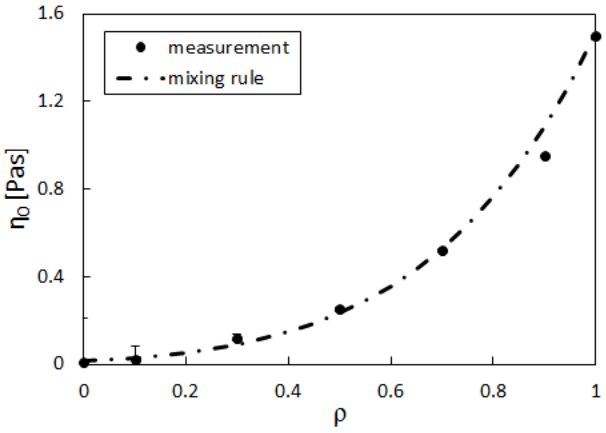

Figure 5.23: Zero shear viscosity as a function of relative volume fraction for bidisperse mixtures of fd (L=0.88 μm, $L_p = 2.8$ μm) and Pf1 (L=1.96 μm, $L_p = 2.8$ μm) in an aqueous buffer at a fixed concentration of 4.2 mg/ml. The line represents the developed mixing rule.

The mixing rule for the zero shear viscosity, following from this linear mixing rule of the volume fraction, characterized by the relation $\varphi \sim L$, see section 2.10, is highly nonlinear due to the nonlinear length dependence of the tube model. Assuming that there is no morphology specific interaction between the rods, we can simply assume that the mean length of particles in the system defines the mean rotational diffusion coefficient in the tube model, $\overline{D}_r \sim \left(L^{(m)}\right)^{-6}$, as well as the mean free rotational diffusion coefficient, $D_r^0 \sim \left(L^{(m)}\right)^{-3}$. Including this in the definition of the zero shear viscosity, equation 2.76, we derived the following mixing rule for the description of the zero shear viscosity of the mixture, see section 2.10:

$$\eta_0 = \eta_s \left[1 + \frac{\pi}{90\ln(L^{(m)}/d)}\nu(L^{(m)})^3 + \frac{\pi}{30c\ln(L^{(m)}/d)}\left(\nu(L^{(m)})^3\right)^3\right] \quad ,$$

where the average length of species in the mixture is $L^{(m)} = L^{(fd)}(1-\rho) + L^{(pf1)}\rho$ and the average particle length is $\rho = (L^{(m)} - L^{(fd)}/(L^{(pf1)} - L^{(fd)}) = (\varphi^{(m)} - \varphi^{(fd)}/(\varphi^{(pf1)} - \varphi^{(fd)})$. The mixing rule represents the measured data in figure 5.23 quite well, using a prefactor of $c = c^{(pf1)} = 2630$ for the diffusion coefficient of Pf1, obtained from the fitting procedure outlined in section 5.3.2. Since the dominant species, so the species with higher zero shear viscosity, is the Pf1 bacteriophage, the prefactor is chosen accordingly. The absolute value of c

being smaller than the previously estimated 2700 for an ideal, stiff rod reflects the fact that both species are flexible to a certain extent, although $L < L_p$. Since the Pf1 bacteriophage is two times longer than fd, it seems clear that the stress relaxation mechanism of the mixture is dominated by the dynamics of the longer species. However, it is interesting to note that apparently no tube dilation due to the smaller virus takes place. This can be inferred from the fact that the simple linear mixing rules, included in the description of the zero shear viscosity, lead to a reasonably good agreement with the measurement. Nonetheless, it is thinkable that a mixture of a high aspect ratio rod with a comparatively very low aspect ratio rod displays signs of tube dilation due to the length disparity. Here, no such effects are measured.

5.6.2 Effects of bidispersity on the shear-thinning behavior

Since the effect of length on the shear-thinning behavior of rods is clearly visible from figure 5.13, and we gained understanding of the zero shear viscosity and shear-thinning process, all the ingredients are available to study the effect of polydispersity on the shear-thinning behavior as well. This is of great practical use as most rod-like systems, from industry as well as in nature, are polydisperse. In figure 5.24, the viscosity curves of the different mixtures of the long and flexible rod, Pf1, with the short and flexible rod, fd, are shown. The zero shear viscosity plateau is cut off in this figure in order to fit the curves with a power law, $\eta = k\dot{\gamma}^n$, where $n = 1 - m$ and k is a constant. This allows us to display the effect of polydispersity on the shear-thinning behavior. The inset of figure 5.24 displays the shear-thinning parameter, n, as a function of the relative volume fraction of the mixture, $\rho = (L^{(m)} - L^{(fd)}/(L^{(pf1)} - L^{(fd)})$. The shear-thinning parameter can be equivalently obtained by fitting the viscosity curves in the shear-thinning region with the Carreau equation: $\eta = \eta_s + (\eta_0 - \eta_s)/(1 + a\dot{\gamma})^n$.

The power-law fit is used to quantify the newly developed theory, using equation 2.90 combined with 2.92. The inset of figure 5.24 shows that the shear-thinning coefficient increases non-linearly with the relative volume fraction. For completeness, we mention here that the curve can be described by the relation $n^{(m)} = n^{(fd)} + k\rho^{\alpha}$, with $k = 0.3$ and a slope of $\alpha = 0.6$, displayed as the line in the inset of figure 5.24. This could be used for a further investigation of the seemingly nonlinear nature of the shear-thinning process in bidisperse mixtures of rods. Nonetheless, it should be emphasized that the data in the inset of figure 5.24 could be compared with a linear mixing rule for n as well, since the non-linearity with an exponent $\alpha = 0.6$ is not strong. This renders the choice of an appropriate mixing rule difficult. We would assume, however, that there is a fundamental difference between the linear mixing rule for the zero shear viscosity and the near-linear mixing rule for the shear-thinning coefficient, since

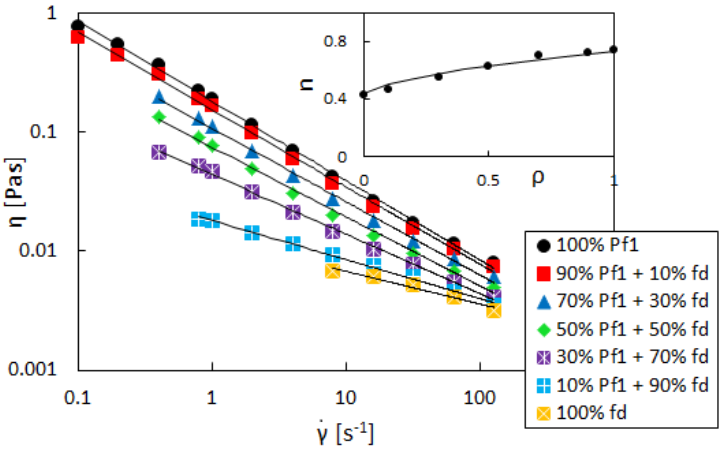

Figure 5.24: Viscosity in the shear-thinning regime as a function of shear-rate for bidisperse mixtures of fd (L=0.88 μm, $L_p = 2.8$ μm) and Pf1 (L=1.96 μm, $L_p = 2.8$ μm) in an aqueous buffer at a fixed concentration of 4.2 mg/ml. The lines are power-law fits with an exponent, m, given in the inset, and prefactors $k = \{0.18, 0.15, 0.1, 0.07, 0.04, 0.02, 0.01\}$ from top to bottom. Inset: Shear-thinning parameter of the mixture as a function of the relative volume fraction. The line shows a power law for m with exponent $\alpha = 0.6$, and prefactor $k = 0.3$. Error bars are omitted for reasons of readability.

tube dilation plays an important role for the non-equilibrium diffusivity of rods in general.

The slight non-linearity of the estimated mixing rule for the shear-thinning coefficients can be made obvious by comparing the results of equation 2.90, combined with 2.92, to the measurements of the nonlinear viscosity, see figure 5.25. Here, we used again the prefactor $c = 2600$ for the rotational diffusion coefficients of both rods.

From the comparison of the spacing between measured curves and the spacing between theoretical curves, the nonlinearity spotted before becomes evident. Especially, the shear-thinning of the samples holding 30 and 50% Pf1 is much stronger than predicted by the linear mixing rule. Also, curves holding higher percentages of Pf1 are more densely spaced compared to the theoretical lines. Despite some discrepancies between the theoretical prediction and the viscosity curves of Pf1, it is obvious that the shear-thinning behavior of a rod-like system is strongly influenced by the relative abundance of two different species. It

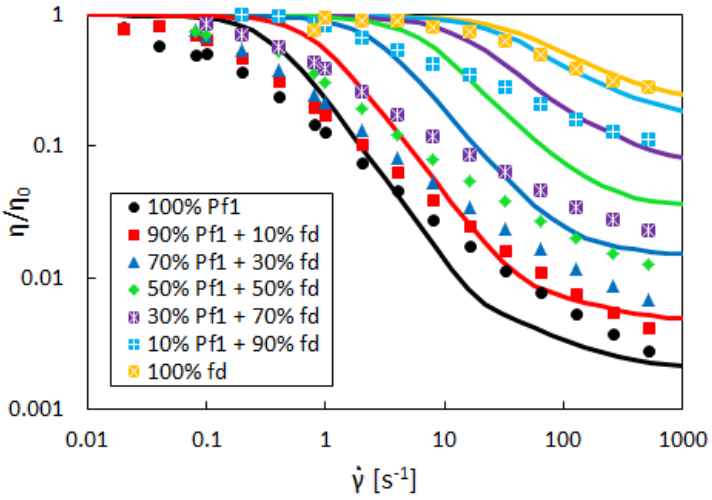

Figure 5.25: Shear viscosity as a function of shear-rate for bidisperse mixtures of fd (L=0.88 μm, $L_p = 2.8$ μm) and Pf1 (L=1.96 μm, $L_p = 2.8$ μm) in an aqueous buffer at a fixed concentration of 4.2 mg/ml. The lines are predictions from equation 2.59, using the linear mixing rule, equation 2.92, in $\langle D_r \rangle$ with a prefactor $c = 2630$. Error bars are omitted for reasons of readability.

seems reasonable, that the particle-interaction under flow changes due to the bidispersity. Here, we assumed that the particle interaction of a bidisperse mixture of rods is equivalent to the interaction of two rods of the same species. Since the theory does not give satisfying results, it is advisable to additionally employ a polydispersity dependent particle-interaction potential like that developed by Marrucci and Grizzuti [113], where the inter-particle potential, presented here in the Dhont-Briels framework, equation 2.57, would have to be replaced by that of the i-th species present in the mixture:

$$\overline{V}_i = \frac{5\pi}{8}\frac{L_i}{d}\beta^{-1}\sum_j \varphi_j \left(1 - \frac{3}{5}\mathbf{S}_j : \mathbf{uu}\right) \quad . \tag{5.2}$$

However, we learned from our experimental investigation of the ideal rod, chapter 4, that such an effective potential is insufficient to correctly predict the flow behavior in the Fokker-Planck approach. This might also explain the differences between this theory and the experiment by Larson and Mead [114]. We propose that instead of equation 5.2, an inter-particle potential for polydisperse rods should, at last, also include a revised pair-correlation function.

We did not develop such an expression yet, but it could be seen as an extension of the Marrucci-Grizzuti theory and seems to be an interesting future research topic.

Also, measurements of the dynamics of rods in a bidisperse mixture would be needed in order to gain a deeper understanding of these rheological results. Laser confocal microscopy of a sheared bidisperse mixture with two differently labeled rod-like viruses would be an interesting tool for such an investigation.

5.7 Shear banding close to the isotropic-nematic transition

In section 4.4, we established that a low shear-thinning coefficient is indispensable for the occurrence of a gradient shear banding instability, in accordance with the literature [182, 165, 159]. We also observed that the ideal rod, fd-Y21M, does not yield strong shear-thinning, which might be related with its relatively moderate length. As seen in figure 5.10(a), the strongest shear-thinning bacteriophage is the relatively long Pf1 virus ($L = 1.96$ μm). In this section, the goal is to identify the strongest shear-thinning system, which is of course to be found very close to the IN transition and using the longest particle. In figure 5.26(b), the difference between shear-thinning coefficients of the ideal rod, fdY21M, and the longer and more flexible rods m13k07 and Pf1 are plotted as obtained from flowcurves of the shear stress, $\Sigma_{21} = \Sigma_{yx}$, as a function of shear-rate, all very close to the I-N transition.

The shear-thinning parameter of Pf1 in the intermediate shear-rate regime reaches a value of $m = 0.2$, roughly a factor 1.5 smaller than the shear-thinning coefficient of fdY21M. This shows that Pf1 is the likeliest of all used rodlike phages to undergo gradient shear banding, as expected.

In order to test for a GSBI in Pf1 samples which are sufficiently close to the isotropic nematic spinodal, a combination of SANS and flow-HDLS is used. SANS, thereby, constitutes another possibility of detecting a GSBI by measuring the order parameter along the gradient direction. Since the order parameter strongly depends on the shear-rate, also this quantity should display a sudden change of slopes along the gradient direction, such as the fluid velocity. This method is less direct than measuring the flow profile. Figure 5.27 displays the velocity profiles and orientation profiles of Pf1 in the low and intermediate shear-rate regime. In accordance with the low shear-thinning coefficients obtained from the flow curves, m_{fc}, low shear-thinning coefficients, m, are found in both regimes, see figures 5.27(a) and (c).

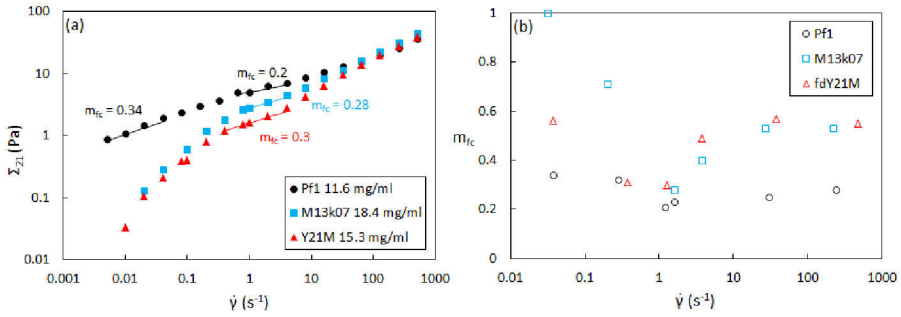

Figure 5.26: (a): Shear stress as a function of shear-rate for fdY21M (L=0.91 μm, L_p = 9.9 μm), M13k07 (L=1.2 μm, L_p = 2.8 μm), and Pf1 (L=1.96 μm, L_p = 2.8 μm) in an aqueous buffer of 100 mM ionic strength. The concentrations are very close to the individual IN transitions. (b): Shear-thinning coefficients of three viruses as a function of the shear-rate, obtained by fitting a power law with exponent m to the curves in (a). Fits in (a) are shown for selected shear-rate ranges (colored lines). Error bars are negligibly small.

While no shear-banded velocity profiles can be detected in either shear-rate regime, the order parameter displays a significant gradient at certain shear-rates, see figures 5.27(b) and (d). These gradients have often been used in the literature to show the occurrence of a GSBI [183, 161, 184, 185]. The measurements presented here, however, clearly indicate that a gradient in the order parameter is not sufficient to cause shear banding as is obvious from the velocity profiles.

Still, two curve characteristics in figure 5.27 are interesting: the curve of $\langle P_2 \rangle$ at rest in figure 5.27(d), and the curve at a shear-rate of 0.0025 s^{-1} in figure 5.27(b). At rest, obviously, the wall induces an orientational ordering, or wall anchoring [186, 187], for a distance as far as 70 μm in gradient direction. This is a surprisingly long-ranged ordering for this kind of phenomenon. As soon as a small shear-rate is applied, however, the ordering reaches values far larger than those measured close to the wall throughout the whole gap, such that the influence of wall-anchoring on the behavior under flow can be neglected. At very low shear-rates, the gradient of the order parameter is especially steep, despite the fact that the shear-thinning parameter, m_{fc}, is comparatively large, reaching a value of 0.3. This motivates a closer study of the system in these conditions. Using time-resolved rheo-SANS in combination with time resolved flow-HDLS measurements, it becomes obvious that the system is indeed undergoing a GSBI,

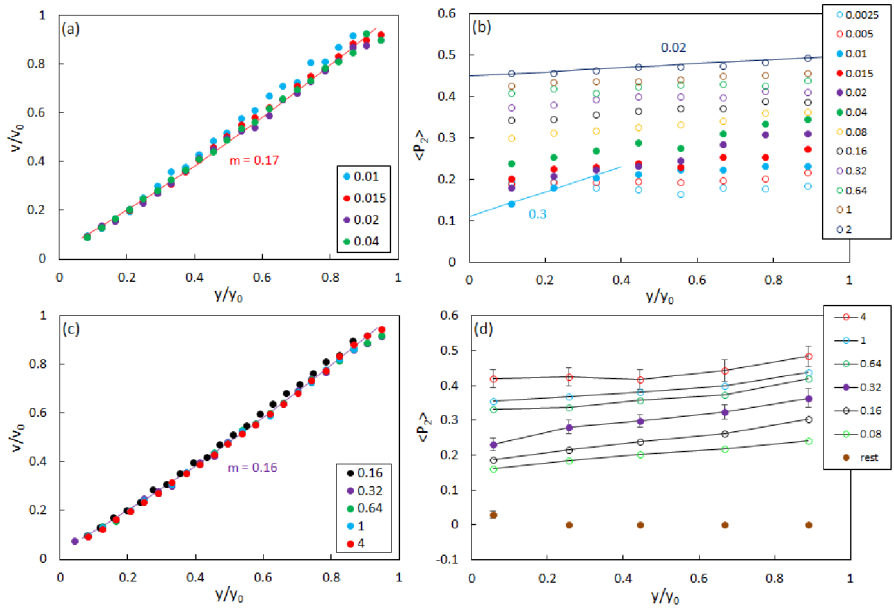

Figure 5.27: Scaled velocity versus relative gap position for Pf1 (L=1.96 μm, $L_p = 2.8$ μm), suspended in an aqueous buffer, in (a) the low shear-rate regime and (c) at intermediate shear-rates. The lines indicate fits to the data at 0.015 and 0.32 s^{-1}. Order parameter versus scaled gap position for different shear-rates in (b) the low shear-rate regime and (d) at intermediate shear-rates, the lines indicate the slope of $\langle P_2 \rangle$. Error bars are omitted for reasons of readability.

see figure 5.28.

This instability, however, is not stable over time and decomposes during an uptake of about 9 strain units. This is an indication that the interface between shear bands cannot be sustained [188, 189]. The reason for this remains unclear at the moment, but it should be added that the network formation of Pf1 could be inefficient compared to other shear banding systems with significantly higher contour length [190, 191, 159]. In addition to the instability, wall slip is observed which vanishes together with the instability, very similar to the GSBI detected in wormlike micellar systems [192, 193].

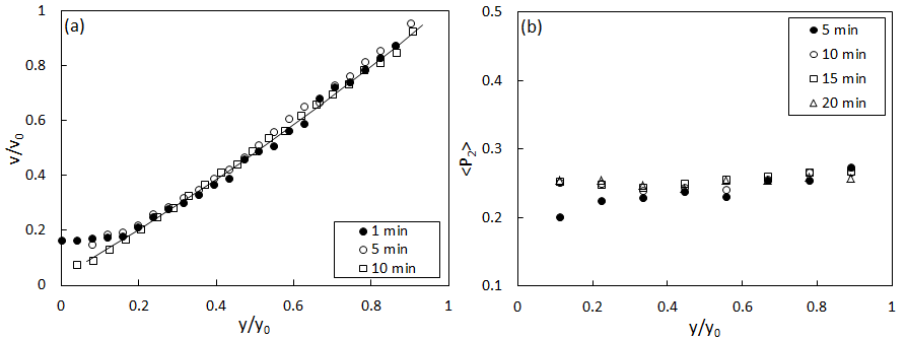

Figure 5.28: Gap scan of Pf1 (L=1.96 μm, L_p = 2.8 μm) at a shear-rate of 0.015 s^{-1} in (a) the velocity and (b) the orientational ordering. The line indicates the velocity profile for a shear-thinning coefficient of 0.17. Error bars are negligibly small.

5.8 Summary

In this chapter, the effect of length and flexibility on the linear and nonlinear rheological behavior is investigated. The particle length is clearly identified as the most important quantity. An increase in length forces the particles into a strongly entangled network, as described by the tube model, increasing the zero shear viscosity, the elongational viscosity, and the shear-thinning, such that for high lengths even shear banding can be provoked. The strong length dependence of visco-elastic properties also plays a decisive role in length-polydisperse samples. For the zero shear viscosity of bidisperse samples, where both species have an aspect ratio larger than 80, however, the tube size seems to be unaffected, only the shear-thinning, again, increases strongly with increasing concentration of the longer species relative to the shorter one. Also, the particle flexibility is of importance for the behavior of rods under shear flow, as both the zero shear viscosity and the shear-thinning are reduced with increasing flexibility and the relaxation time spectrum becomes broader, manifesting itself clearly in relaxation experiments. While the more flexible species shows less shear-thinning, the elongational viscosity also reduces in comparison with the stiffer rods, resulting in higher achievable Trouton ratios for the stiffer particles. From the measured biaxiality of rods with different flexibility, we conclude that flexible rods undergo hairpin formation under shear flow. This conformational change underlies our experimental observations in shear as well as elongational flow.

Chapter 6

Conclusions

Based on the development of a library of ideal and non-ideal monodisperse rodlike viruses, the linear and nonlinear rheological behavior of rods in the dilute and especially in the semi-dilute concentration regime, up to the isotropic-nematic spinodal, is investigated. Generally, these systems undergo shear thinning and concomitant biaxial orientational ordering in the flow direction. This work contains guidelines for understanding the effects of non-ideality aspects, such as particle flexibility and polydispersity, on this behavior.

In accordance with the theory of Morse, however not in perfect correspondence, small amplitude oscillatory shear experiments performed on the ideal rodlike virus, fdY21M, prove the existence of a relaxation time spectrum for rods. The relaxation times for rotational diffusion and chain undulation, therefore, are quantities which can be measured rheologically. The existence of such a spectrum is also evident from stress relaxation experiments, investigated using time resolved rheo-small angle neutron scattering. The non-exponential decay of the order parameter with time, resulting from these measurements, can only be fitted using the assumption of several relaxation times. In addition, these measurements provide indirect evidence for tube dilation.

The importance of reptation as well as tube dilation for the nonlinear rheology of ideal rods is further established. Various experimental investigations are compared to theoretical investigations, confirming that without the inclusion of the tube model as well as tube dilation for the rotational diffusion coefficient as well as the interaction potential, Doi-Edwards-Kuzuu theory fails to predict the onset and magnitude of shear thinning of ideal semidilute rodlike suspensions. Thus, a suitable theoretical description uniting both aspects is carried out. While the inclusion of reptation in the expression for the rotational diffusion

coefficient is straight forward and provides us with a quantitative prediction of the zero shear viscosity, no solution for the full inclusion of a shear mediated inter-particle potential is found. Under certain strong assumptions, however, a simple solution to this problem is established which captures the magnitude of shear thinning quite well.

Flexibility influences on the relaxation time spectrum are found, specifically, a broadening of the elastic response regime for high concentrations of rods. In addition, flexibility of the particles hampers the phase transition and lowers the zero shear viscosity of the suspension. Under strong shear, however, flexible particles undergo less shear thinning than their stiff counterparts, most probably due to the formation of hairpins. Hairpin formation under elongational flow is impossible, leading to the observation that the elongational viscosity has the same flexibility dependence as the zero shear viscosity, provoking comparatively large Trouton ratios for stiff rodlike systems in the absence of high normal forces.

While particle thickness has no influence on the flow behavior of rods, their length is the most important quantity influencing their rheological response. A strong increase of the zero shear viscosity with increasing length of the rods is found experimentally and described theoretically. With increasing length, such as predicted theoretically, the shear thinning becomes stronger. In very long systems, sufficiently close to the isotropic-nematic phase transition, shear thinning becomes so strong that time dependent gradient shear banding is observed.

Polydispersity of the constituent particles influences both, the particle dynamics as well as the interactions among particles. From a bidispersity study, it is concluded that the existence of a tube allows for a linear mixing rule for the zero shear viscosity of rods. This opens the path for a simple prediction of this quantity for fully polydisperse rodlike colloids. The shear thinning behavior of rod mixtures, on the other side, is still poorly understood. The reason is the complex particle-interaction. Based on the observations in this work, however, two potential routes towards a solution of this problem are introduced.

Chapter 7

Outlook

For a continuation of the work presented in this thesis, the following topics are suggested:

Using scaling procedures for the nonlinear viscosity and orientational ordering curves, we extracted the rotational self-diffusion coefficient as a function of particle length and concentration from our experimental data, see sections 4.3.2, 5.2, and 5.3.2. Our results compare well with the tube model, but we find that tube dilation plays a non-negligible role. In order to confirm these results, direct observations of fluorescently labeled rods in quiescent conditions as well as under shear flow are needed, using the home-built shear-cell in Jülich, combined with a confocal laser microscope.

From rheo-SANS experiments, we concluded that flexible particles undergo hairpin formation under steady shear flow, see section 5.3.5. This assertion was used in section 5.3.1 to explain the unusually high hydrodynamic radius of flexible rods, and in section 5.4 to explain the differences between shear and elongational viscosity for stiff and flexible rods. Therefore, it seems important to test for hairpin formation in these systems using laser confocal microscopy under shear flow.

The same technique should be used in a future investigation in order to test whether bidisperse species interact in a different manner than monodisperse species, a conclusion drawn from rheological experiments presented in section 5.6.2. For this purpose, fd virus and Pf1 virus should be fluorescently labeled with different colors and their dynamics under shear should be directly investigated.

Resulting from disparities between theory and measurements for the nonlinear rheology of bidisperse rod-like particle suspensions, presented in section 5.6.2, we advise the derivation of a polydispersity dependent particle-particle interaction with the aim of explaining the non-equilibrium shear flow behavior of polydispcerse rod suspensions.

As the comparison of rheological results in shear and elongational flow showed opposite stiffness dependencies, we further suggest to conduct rheo-SANS measurements of rods under elongational flow with special emphasis on the influence of stiffness on the particle dynamics. These experiments should be highly time-resolved and could be combined with the already measured rheo-SANS data of rods in start-up flow experiments (conducted for but not shown in this thesis).

As the experiments on ideal viruses under steady shear flow are still not completely understood, although the tube dilation mechanism was introduced in section 2.7, and a strongly simplified non-equilibrium pair-correlation function was developed in section 2.8, it is suggested that further research is done on equation 2.84. This could lead to the development of a shear dependent pair-correlation function under the least necessary approximations, using the Fokker-Planck equation for N rods and subsequently reducing the equations to the two particle case. Such an approach could potentially lead to a complete understanding of rods in shear flow.

Bibliography

[1] Y.-G. Tao, W. K. den Otter, and W. J. Briels. Shear Viscosities and Normal Stress Differences of Rigid Liquid-Crystalline Polymers. *Macromolecules*, 39(17):5939–5945, 2006.

[2] Teraoka I, Ookubo N, and Hayakawa R. Molecular theory on the entanglement effect of rodlike polymers. *Phys. Rev. Lett.*, 55:2712, 1985.

[3] W. D. Kingery, H. K. Bowen, and D. R. Uhlmann. *Introduction to ceramics*. Wiley-Interscience, 1976.

[4] D. Hradil, T. Grygar, J. Hradilova, and P. Bezdicka. Clay and iron oxide pigments in the history of painting. *Appl. Clay Science*, 22:223–236, 2003.

[5] L. Bailey, H. N. W. Lekkerkerker, and G. C. Maitland. Smectite clay–inorganic nanoparticle mixed suspensions: phase behaviour and rheology. *Soft Matter*, 3:1145–1162, 2007.

[6] W. M. Stanley and T. F. Anderson. A study by means of the electron microscope of the reaction between tobacco mosaic virus and its antiserum. *J. Biol. Chem.*, 139:325–338, 1941.

[7] J. B. Hays, M. E. Magar, and B. H. Zimm. Persistence length of dna. *Biopolymers*, 8:531–536, 1969.

[8] P. Westermark. Amyloid of human islets of lagerhans. *Virchows Archiv A*, 373:161–166, 1977.

[9] P. J. Whitcomb and C. W. Macosko. Rheology of xanthane gum. *J. Rheol.*, 22:493, 1978.

[10] E. L. Elson. Cellular mechanics as an indicator of cytoskeletal structure and function. *Ann. Rev. Biophys. Chem.*, 17:397–430, 1988.

[11] M. T. Cabeen and C. Jacobs-Wagner. Bacterial cell shape. *Nat. Rev. Microbiol.*, 3:601–610, 2005.

[12] M. L. Gardel, J. H. Shin, F. C. MacKintosh, L. Mahadevan, P. Matsudaira, and D. A. Weitz. Elastic behavior of cross-linked and bundled actin networks. *Science*, 304:1301–1305, 2004.

[13] M. M. de Souza Lima and R. Borsali. Rodlike cellulose microcrystals: Structure, properties, and applications. *Macro. Rap. Comm.*, 25(7):771–787, 2004.

[14] Y. C. Lin, G. H. Koenderink, and F. C. MacKintosh andD. A. Weitz. *Macromolecules*, 40:7714, 2007.

[15] K. M. Schultz, A. Baldwin, K. L. Kiick, and E. M. Furst. Gelation of covalently cross-linked peg-heparin hydrogels. *Macromolecules*, 42:5310–5316, 2009.

[16] D. S. W. Benoit, A. R. Durney, and K.i S. Anseth. The effect of heparin-functionalized peg hydrogels on three-dimensional human mesenchymal stem cell osteogenic differentiation. *Biomaterials*, 28(1):66 – 77, 2007.

[17] S. Kheirandish, I. Guybaidullin, W. Wohlleben, and N. Willenbacher. Shear and elongational flow behavior of acrylic thickener solutions. *Rheol. Acta*, 47:999–1011, 2008.

[18] D. Srivastava, C. Wei, and K. Cho. Nanomechanics of carbon nanotubes and composites. *Appl. Mech. Rev.*, 56:215–230, 2003.

[19] A. V. Kyrylyuk and P. van der Schoot. Continuum percolation of carbon nanotubes in polymeric and colloidal media. *PNAS*, 105:8221–8226, 2008.

[20] E. K. Hobbie, J. A. Fagan, J. Obrzut, and S. D. Hudson. Microscale polymer-nanotube composites. *ACS App. Mater. and Interface*, 1:1561–1566, 2009.

[21] A. D. Maynard. Nanotechnology: assessing the risks. *Nanotoday*, 1:22–33, 2006.

[22] T. Schilling, S. Jungblut, and M. A. Miller. Depletion-induced percolation in networks of nanorods. *Phys. Rev. Lett.*, 98:108303–1–4, 2007.

[23] E. Grelet and S. Fraden. What is the origin of chirality in the cholesteric phase of virus suspensions? *Phys. Rev. Lett.*, 90:198302–1–4, 2003.

[24] Z. Dogic and S. Fraden. Ordered phases of filamentous viruses. *Curr. Opin. Colloid. In.*, 11, 2006.

[25] J. T. Yang. *J. Am. Chem. Soc.*, 80:1783, 1958.

[26] J. Hermans. The viscosity of concentrated solutions of rigid rodlike molecules (poly-y-benzyl-l-glutamate in m-cresol). *J. Coll. Sci.*, 17(7):638 – 648, 1962.

[27] N. Ookubo, M. Komatsubara, H. Nakajima, and Y. Wada. Infinite dilution viscoelastic properties of poly(y-benzyl-l-glutamate) in m-cresol. *Biopolymers*, 15(5):929–947, 1976.

[28] J. Li, J-F. Revol, and R.H. Marchessault. Rheological properties of aqueous suspensions of chitin crystallites. *J. Coll. Int. Sci.*, 183(2):365 – 373, 1996.

[29] M. P. Lettinga, Z. Dogic, H. Wang, and J. Vermant. Flow Behavior of Colloidal Rodlike Viruses in the Nematic Phase. *Langmuir*, 21:8048–8057, 2005.

[30] Z. Dogic and S. Fraden. Smectic phase in a colloidal suspension of semiflexible virus particles. *Phys. Rev. Lett.*, 78:2417, 1997.

[31] Z. Dogic and Z. Fraden. Development of model colloidal liquid crystals and the kinetics of the isotropic–smectic transition. *Phil.Trans. R. Soc. London Series A-Mathematical Physical and Engineering Sciences*, 359:997–1014, 2001.

[32] K. R. Purdy, Z. Dogic, S. Fraden, A. Rühm, L. Lurio, and S. G. J. Mochrie. Measuring the nematic order of suspensions of colloidal fd virus by x-ray diffraction and optical birefringence. *Phys. Rev. E*, 67(3):031708, 2003.

[33] Z. Dogic, J. Zhang, A. W. C. Lau, H. Aranda-Espinoza, P. Dalhaimer, D. E. Discher, P. A. Janmey, Randall D. Kamien, T. C. Lubensky, and A. G. Yodh. Elongation and fluctuations of semiflexible polymers in a nematic solvent. *Phys. Rev. Lett.*, 92:125503, Mar 2004.

[34] M. P. Lettinga and J. K. G. Dhont. Non-equilibrium phase behaviour of rod-like viruses under shear flow. *J. Phys.: Cond. Mat.*, 16(38):S3929, 2004.

[35] F. Tombolato, A. Ferrarini, and E. Grelet. Chiral nematic phase of suspensions of rodlike viruses: Left-handed phase helicity from a right-handed molecular helix. *Phys. Rev. Lett.*, 96:258302, Jun 2006.

[36] M. P. Lettinga, K. Kang, P. Holmqvist, A. Imhof, D. Derks, and J. K. G. Dhont. Nematic-isotropic spinodal decomposition kinetics of rodlike viruses. *Phys. Rev. E*, 73:011412, Jan 2006.

[37] M. P. Lettinga and E. Grelet. Self-diffusion of rodlike viruses through smectic layers. *Phys. Rev. Lett.*, 99:197802, Nov 2007.

[38] M. Ripoll, P. Holmqvist, R. G. Winkler, G. Gompper, J. K. G. Dhont, and M. P. Lettinga. Attractive Colloidal Rods in Shear Flow. *Phys. Rev. Lett.*, 101(16):168302, 2008.

[39] E. Grelet, M P. Lettinga, M. Bier, R. van Roij, and P. van der Schoot. Dynamical and structural insights into the smectic phase of rod-like particles. *J. Phys.: Cond. Mat.*, 20(49):494213, 2008.

[40] E. Pouget, E. Grelet, and M. P. Lettinga. Dynamics in the smectic phase of stiff viral rods. *Phys. Rev. E*, 84:041704, Oct 2011.

[41] L. Onsager. The effects of shape on the interaction of colloidal particles. *Ann. N. Y. Acad. Sci.*, 51:627, 1949.

[42] M. Zrinyi, M. Kabai-Faix, F. Horkay, and S. Fuhos. Sedimentation and gelation of flocculated iron (iii) hydroxide sols. *Langmuir*, 9:71–76, 1993.

[43] M. J. Solomon and D. V. Boger. The rheology of aqueous dispersions of spindle-type colloidal hematite rods. *J. Rheol.*, 42:929–949, 1998.

[44] A. Mohraz and M. J. Solomon. Gelation and internal dynamics of colloidal rod aggregates. *J. Colloid. Interface Sci.*, 300:155–162, 2006.

[45] V. A. Davis, L. M. Ericson, A. N. G. Parra-Vasquez, H. Fan, Y. Wang, V. Pietro, J. A. Longoria, S. Ramesh, R. K. Saini, C. Kittrell, W. E. Billups, W. W. Adams, R. H. Hauge, R. E. Smalley, and M. Pasquali. Phase behavior and rheology of swnts in superacids. *Macromolecules*, 37:154–160, 2004.

[46] A. N. G. Parra-Vasquez, I. Stepanek, C. A. Davis, V. C. Moore, E. H. Haroz, J. Shaver, R. H. Hauge, R. E. Smalley, and M. Pasquali. Simple length determination of single-walled carbon nanotubes by viscosity measurements in dilute suspensions. *Macromolecules*, 40:4043–4047, 2007.

[47] S. Marceau, P. Dubois, R. Fulchiron, and P. Cassagnau. Viscoelasticity of brownian carbon nanotubes in pdms semidilute regime. *Macromolecules*, 42:1433–1438, 2009.

[48] L. Czarnecki and J. L. White. Shear flow rheological properties, fiber damage, and mastication characteristics of aramid-, glass-, and cellulose-fiber-reinforced polystyrene melts. *J. Appl. Polym. Sci.*, 25(6):1217–1244, 1980.

[49] F. Folgar and C. L. Tucker. Orientation Behavior of Fibers in Concentrated Suspensions. *J. Reinf. Plast. Comp.*, 3(2):98–119, 1984.

[50] F. C. MacKintosh, P. A. Janmey, and J. Kas. *Phys. Rev. Lett.*, 75:4425, 1995.

[51] L. A. Hough, M. F. Islam, P. A. Janmey, and A. G. Yodh. Viscoelasticity of single wall carbon nanotube suspensions. *Phys. Rev. Lett.*, 93:168102–1–4, 2004.

[52] W. N. Takahashi and T. E. Rawlins. Rod-shaped particles in tobacco mosaic virus demonstrated by stream double refraction. *Science*, 77(1984):26–27, 1933.

[53] M. A. Lauffer. Viscosity of tobacco mosaic virus protein solutions. *J. Bio. Chem.*, 126:443–453, 1938.

[54] F. C. Baeden and N. W. Pirie. The isolation and some properties of liquid crystalline substances from solanaceous plants infected with three strains of tobacco mosaic virus. *P. Roy. Soc. Lon. B Bio.*, 123(832):274–320, 1937.

[55] C. Graf, H. Kramer, M. Deggelmann, M. Hagenbüchle, C. Johner, C. Martin, and R. Weber. Rheological properties of suspensions of interacting rodlike fd virus particles. *J. Chem. Phys.*, 98(6):4920–4928, March 1993.

[56] J. Sambrook, E. F. Fritsch, and T. Maniatis. *Molecular cloning: A laboratory Manual*. Cold Spring Harbor University Press, Cold Spring Harbor Press, 1989.

[57] S. A. Overmann, K. L. Aubrey, N. S. Visbo, G. Cesareni, and G. J. Thomas Jr. Novel tyrosine markers in raman spectra of wild-type and mutant (y21m and y24m) ff virions indicate u nusual environments for coat protein phenoxyls. *Biochemistry*, 33:1037–1042, 1994.

[58] S. Ogawa and S. Oka. Theory of electric birefringence in dilute solutions of tobacco mosaic virus. *Journal of the Physical Society of Japan*, 15(4):658–668, 1960.

[59] J. M. Schurr and K. S. Schmitz. Rotational relaxation of macromolecules determined by dynamic light scattering. i. tobacco mosaic virus. *Biopolymers*, 12(5):1021–1045, 1973.

[60] T. Maeda and S. Fujime. Effect of filament flexibility on the dynamic light-scattering spectrum with special reference to fd virus and muscle thin filaments. *Macromolecules*, 14:809–818, 1981.

[61] D.A. Marvin. X-ray diffraction and electron microscope studies on the structure of the small filamentous bacteriophage fd. *J. Mol. Bio.*, 15(1):8 – IN4, 1966.

[62] J. Torbet. Neutron scattering study of the solution structure of bacteriophages pf1 and fd. *FEBS Letters*, 108(1):61–65, 1979.

[63] S. Förster, M. Konrad, and P. Lindner. Shear Thinning and Orientational Ordering of Wormlike Micelles. *Phys. Rev. Lett.*, 94(1):017803, January 2005.

[64] H. Kramer, M. Deggelmann, C. Graf, M. Hagenbuechle, C. Johner, and R. Weber. Electric birefringence measurements in aqueaous fd virus solutions. *Macromolecules*, 25:4325–4328, 1992.

[65] F. G. Schmidt, B. Hinner, and E. Sackmann ans J. X. Tang. Viscoelastic properties of semiflexible filamentous bacteriophage fd. *Phys. Rev. E*, 62:5509–5517, 2000.

[66] K. Kang, M. P. Lettinga, Z. Dogic, and J. K. G. Dhont. Vorticity banding in rodlike virus suspensions. *Phys. Rev. E.*, 74:026307–1–12, 2006.

[67] E. Sarmiento-Gomez, D. Montalvan-Sorrosa, C. Garza, J. Mas-Oliva, and R. Castillo. Rheology and dws microrheology of concentrated suspensions of the semiflexible filamentous fd virus. *Eur. Phys. J. E*, 35:35–49, 2012.

[68] Z. Zhang, N. Krishna, M. P. Lettinga, J. Vermant, and E. Grelet. Reversible gelation of rod-like viruses grafted with thermoresponsive polymers. *Langmuir*, 25:2437–2442, 2009.

[69] M. Huang, R. Rotstein, S. Fraden, Kasza K. E, and N. T. Flynt. Phase behavior and rheology of attractive rod-like particles. *Soft Matter*, 5:2766–2771, 2009.

[70] E. Barry, D. Beller, and Z. Dogic. A model liquid crystalline system based on rodlike viruses with variable chirality and persistence length. *Soft Matter*, 5, 2009.

[71] G. B. Jeffery. The motion of ellipsoidal particles immersed in a viscous fluid. *Proc. R. Soc. London*, 102:161–179, 1922.

[72] J. G. Kirkwood and R. J. Plock. Non-newtonian viscoelastic properties of rod-like macromolecules in solution. *J. Chem. Phys.*, 24:665–669, 1956.

[73] J. Broersma. Rotational diffusion constant of a cylindrical particle. *J. Chem. Phys.*, 32:1626–1632, 1964.

[74] G. K. Batchelor. Slender-body theory for particles of arbitrary cross-section in stokes flow. *J. Fluid. Mech.*, 41:545–557, 1970.

[75] E. J. Hinch and L. G. Leal. The effect of brownian motion on the rheological properties of a suspension of non-spherical particles. *J. Fluid. Mech.*, 52:683–712, 1972.

[76] P. G. de Gennes. Reptation of a polymer chain in the presence of fixed obstacles. *J. Chem. Phys.*, 55(2):572–579, 1971.

[77] M. Doi and S. F. Edwards. Dynamics of rod-like macromolecules in concentrated solution. part 1. *J. Chem. Soc., Faraday Trans. 2*, 74:560–570, 1978.

[78] S. Hess. Fokker-planck-equation approach to flow alignment in liquid crystals. *Z. Naturforschung A*, 36:1034–1037, 1976.

[79] D. C. Morse. Viscoelasticity of concentrated isotropic solutions of semiflexible polymers. 1. model and stress tensor. *Phys. Rev. E*, 58:1237, 1998.

[80] D. C. Morse and Viscoelasticity. Viscoelasticity of concentrated isotropic solutions of semiflexible polymers. 1. model and stress tensor. *Macromolecules*, 31:7030, 1998.

[81] M. Doi and S. F. Edwards. Dynamics of rod-like macromolecules in concentrated solution. part 2. *J. Chem. Soc., Faraday Trans. 2*, 74:918–932, 1978.

[82] E. S. G. Shaqfeh and G. H. Fredrickson. The hydrodynamic stress in a suspension of rods. *Phys. Fluids A*, 2:7–24, 1990.

[83] P. D. Olmsted. Dynamics and flow-induced phase separation in polymeric fluids. *Curr. Opin. Colloid. In.*, 4:95–100, 1999.

[84] P. D. Olmsted and C.-Y. D. Lu. Phase coexistence of complex fluids in shear flow. *Faraday Discuss.*, 112:183–194, 1999.

[85] P. D. Olmsted and C.-Y. D. Lu. Phase separation of rigid-rod suspensions in shear flow. *Phys. Rev. E*, 60:4397–4415, 1999.

[86] J. K. G. Dhont and W. J. Briels. Viscoelasticity of suspensions of long, rigid rods. *Coll. Surf. A*, 213(2–3):131–156, February 2003.

[87] M. Doi and S. F. Edwards. *The theory of polymer dynamics.* Oxford University Press, Oxford, 1986.

[88] M. Doi andT. Shimada and K. Okano. Concentration fluctuation of stiff polymers. *J. Chem. Phys.*, 88:4070, 1988.

[89] D. M. Sussman and K. S. Schweizer. Microscopic theory of quiescent and deformed topologically entangled rod solutions: General formulation and relaxation after nonlinear step strain. *Macromolecules*, 45(7):3270–3284, 2012.

[90] C. W. Oseen. Über die wechselwirkung zwischen zwei elektrischen dipolen und über die drehung der polarisationsebene in kristallen und flüssigkeiten. *Ann. Phys.*, 353(17):1–56, 1915.

[91] G. K. Batchelor. The stress generated in a non-dilute suspension of elongated particles by pure straining motion. *J. Fluid. Mech.*, 46:813–829, 1971.

[92] N. Kuzuu and M. Doi. Constitutive equation for nematic liquid crystals under weak velocity gradient derived from a molecular kinetic equation. *J. Phys. Soc. Jpn.*, 52:3486, 1983.

[93] P. G. de Gennes. Phenomenology of short-range-order effects in the isotropic phase of nematic materials. *Phys. Letters*, 30:454, 1969.

[94] L. Hong, S. M. Anthony, and S. Granick. Rotation in Suspension of a Rod-Shaped Colloid. *Langmuir*, 22(17):7128–7131, 2006.

[95] S. M. Anthony, M. Kim, and S. Granick. Translation-rotation decoupling of colloidal clusters of various symmetries. *J. Chem. Phys.*, 129(24):244701, 2008.

[96] D. M. Sussman and K. S. Schweizer. Microscopic theory of the tube confinement potential for liquids of topologically entangled rigid macromolecules. *Phys. Rev. Lett.*, 107:078102, Aug 2011.

[97] D. M. Sussman and K. S. Schweizer. Microscopic theory of topologically entangled fluids of rigid macromolecules. *Phys. Rev. E*, 83:061501, Jun 2011.

[98] D. M. Sussman and K. S. Schweizer. Communication: Effects of stress on the tube confinement potential and dynamics of topologically entangled rod fluids. *J. Chem. Phys.*, 135(13):131104, 2011.

[99] D. M. Sussman and K. S. Schweizer. Microscopic theory of entangled polymer melt dynamics: Flexible chains as primitive-path random walks and supercoarse grained needles. *Phys. Rev. Lett.*, 109:168306, Oct 2012.

[100] S. Leitmann, F. Höfling, and T. Franosch. Tube concept for entangled stiff fibers predicts their dynamics in space and time. *Phys. Rev. Lett.*, 117:097801, Aug 2016.

[101] B. Tsang, Z. E. Dell, L. Jiang, K. S. Schweizer, and S. Granick. Dynamic cross-correlations between entangled biofilaments as they diffuse. *PNAS*, 114(13):3322–3327, 2017.

[102] A. Einstein. Über die von der molekularkinetischen theorie der wärme geforderte bewegung von in ruhenden flüssigkeiten suspendierten teilchen. *Ann. Phys.*, 322:549–560, 1905.

[103] Q. Zhou and R. G. Larson. Direct calculation of the tube potential confining entangled polymers. *Macromolecules*, 39:6767, 2006.

[104] T. Odijk. The statistics and dynamics of confined or entangled stiff polymers. *Macromolecules*, 16:1340, 1983.

[105] G. J. Vroege and H. N. W. Lekkerkerker. Phase transitions in lyotropic colloidal and polymer liquid crystals. *Rep. Prog. Phys.*, 55(8):1241, 1992.

[106] A. R. Khokhlov and A. N. Semenov. Liquid-crystlline ordering in a solution of long persistent chains. *Physica*, 108A:546–556, 1981.

[107] N. Fakhri, F. C. MacKintosh, B. Lounis, L. Cognet, and M. Pasquali. Brownian motion of stiff filaments in a crowded environment. *Science*, 330:1804–1807, 2010.

[108] Sedgwick H, Cameron J. E, Poon W. C. K, and Egelhaaf S. U. Models and equilibrium properties of stiff molecular chains. *J. Chem. Phys.*, 101:8119, 1997.

[109] R. G. Winkler. Semiflexible polymers in shear flow. *Phys. Rev. Lett.*, 97:128301, 2006.

[110] E. P. Petrov, T. Ohrt, R. G. Winkler, and P. Schwille. Diffusion and segmental dynmics of double-stranded dna. *Phys. Rev. Lett.*, 97:258101, 2006.

[111] D. C. Morse. Viscoelasticity of concentrated isotropic solutions of semiflexible polymers. 2. linear response. *Macromolecules*, 31:7044, 1998.

[112] D. C. Morse. *Macromolecules*, 32:5934–5943, 1999.

[113] G. Marrucci and N. Grizzuti. Predicted effect of polydispersity on rodlike polymer behavior in concentrated solutions. *J. Non-Newtonian Fluid. Mech.*, 14:103–119, 1984.

[114] R. G. Larson and D. W. Mead. Toward a quantitative theory of the rheology of concentrated solutions of stiff polymers. *J. Polym. Sci., Part B: Polym. Phys.*, 29:1271, 1991.

[115] P. Gutjahr, R. Lipowsky, and J. Kierfeld. Persistence length of semiflexible polymers and bedning riidity renormalizetion. *Europhys. Lett.*, 76:994–1000, 2006.

[116] G. Bertani. Studies on lysogenesis i.: The mode of phage liberation by lysogenic escherichia coli1. *J. Bacteriol.*, 62:193–300, 1951.

[117] S. E. Luria and M. L. Human. A nonhereditary, host-induced variation of bacterial viruses. *J. Bacteriol.*, 64:557–569, 1952.

[118] J. Sambrook and D. W. Russel. *Molecular Cloning: A laboratory manual*. Cold Spring Harbor Press, New York, 2001.

[119] J. Vieira and J. Messing. 11 - production of single-stranded plasmid {DNA}. In Ray Wu, Lawrence Grossman, and Kivie Moldave, editors, *Recombinant {DNA} Methodology*, Selected Methods in Enzymology, pages 225 – 233. Academic Press, San Diego, 1989.

[120] S. Brown, J. Majikes, A. Martinez, T. M. Giron, H. Fennell, E. C. Samano, and T. H. LaBean. An easy-to-prepare mini-scaffold for dna origami. *Nanoscale*, 7:16621–16624, 2015.

[121] J. Griffith, M. Manning, and K. Dunn. Filamentous bacteriophage contract into hollow spherical particles upon exposure to a chloroform-water interface. *Cell*, 23:747–753, 1981.

[122] R. Zhang and K. S. Schweizer. Dynamic free energies, cage escape trajectories, and glassy relaxation in dense fluids of uniaxial hard particles. *J. Chem. Phys.*, 133(10):104902, 2010.

[123] L. G. Kostrikis, D. J. Liu, and L. A. Day. *Biochemistry*, 33:1694–1703, 1994.

[124] B. van Grinsven, K. Eersels, O. Akkermans, S. Ellermann, A. Kordek, M. Peeters, O. Deschaume, C. Bartic, H. Diliën, Steen R. E., P. Wagner, and T. J. Cleij. Label-free detection of escherichia coli based on thermal transport through surface imprinted polymers. *ACS Sensors*, 1(9):1140–1147, 2016.

[125] D. T. Papageorgiou. On the breakup of viscous liquid threads. *Phys. Fluids*, 7:1529–1544, 1995.

[126] G. H. McKinley and A. Tripathi. How to extract the newtonian viscosity from capillary breakup measurements in a filament rheometer. *J. Rheol.*, 44:653–670, 2000.

[127] J. Eggers. Universal pinching of 3d axisymmetric free-surface flow. *Phys. Rev. Lett.*, 71:3458–3460, 1993.

[128] J. Eggers. Nonlinear dynamics and breakup of free-surface flows. *Rev. Mod. Phys.*, 69:865–929, 1997.

[129] W. Maier and A. Saupe. Eine einfache molekular-statistische theorie der nematischen kristallinflüssigen phase. teil l1. *Z. Naturforsch. A*, 14:882–889, 1959.

[130] I. Bihannic, C. Baravian, J. F. L. Duval, E. Paineau, F. Meneau, P. Levitz, J. P. de Silva, P. Davidson, and L. J. Michot. Orientational order of colloidal disk-shaped particles under shear-flow conditions: a rheological-small-angle x-ray scattering study. *J. Phys. Chem. B*, 114(49):16347–16355, 2010.

[131] K. V. Hongladrom, D. K. Uglaz, W. R. Cinader, J. P. Burghardt, B. S. Quintana, M. D. Hsia, W. A. Hamilton, and P. D. Butler. Birefringence, x-ray scattering, and neutron scattering measurements of molecular orientation in sheared liquid crystal polymer solutions. *Macromolecules*, 29:5346–5355, 1996.

[132] J. Delgado, H. Kriegs, and R. Castillo. Flow velocity profiles and shear banding onset in a semidilute wormlike micellar system under couette flow. *J. Phys. Chem. B*, 113:15485–15494, 2009.

[133] F. Durst, A. Melling, and J. H. Whitelaw. Principles and practice of laser-Doppler anemometry. *NASA STI-Recon Technical Report A*, 76, 1976.

[134] L. E. Drain. *The laser Doppler techniques.* 1980.

[135] H. Kriegs. *Die Doppelplus-Speckle-Strophometrie- Ein optisches Verfahren zur Messung der Momentanwerte von Geschwindigkeitsgradienten in turbulenten Strömungen.* Dissertation University of Bremen, 1993.

[136] D. H. Berry and W. B. Russel. The rheology of dilute suspensions of slender rods in weak flows. *J. Fuid. Mech.*, 180:475–494, 1987.

[137] S. J. Gason, D. V. Boger, and D. E. Dunstan. Rheo-optic measurements on dilute suspensions of hematite rods. *Langmuir*, 15:7446–7453, 1999.

[138] D. Mukhija and M. J. Solomon. Translational and rotational dynamics of colloidal rods by direct visualization with confocal microscopy. *J. Colloid Interface Sci.*, 314:98, 2007.

[139] K. F. Wissbrun. Rheology of rod-like polymers in the liquid-crystalline state. *J. Rheol.*, 25(6):619–662, 1981.

[140] D. Doraiswamy and A. B. Metzner. The rheology of polymeric liquid crystals. *Rheol. Acta*, 25:580–587, 1986.

[141] A. B. Metzner and G. M. Priluiski. Rheological properties of polymeric liquid crystals. *J. Rheol.*, 30:661, 1986.

[142] M. P. B. van Bruggen, J. K. G. Dhont, and H. N. W. Lekkerkerker. Morphology and kinetics of the isotropic-nematic phase transition in dispersions of hard rods. *Macromolecules*, 32:2256–2264, 1999.

[143] Y.-G. Tao, W. K. den Otter, and W. J. Briels. Kayaking and Wagging of Rods in Shear Flow. *Physical Review Letters*, 95(23):237802, 2005.

[144] E. K. Hobbie and D. J. Fry. Nonequilibrium Phase Diagram of Sticky Nanotube Suspensions. *Phys. Rev. Lett.*, 97(3):036101, July 2006.

[145] Marrucci G. Rheology of rodlike polymers in the nematic phase with tumbling or shear orientation. *Rheol. Acta*, 6:523–528, 1990.

[146] C. Lang, J. Kohlbrecher, L. Porcar, and M. P. Lettinga. *Polymers*, 8:291, 2016.

[147] M. Doi and S. F. Edwards. Dynamics of rod-like macromolecules in concentrated solution. *J. Chem. Soc. Faraday Trans. 2*, 74:560–570, 1977.

[148] M. Doi. *J. Polym. Sci., Polym Lett. Ed.*, 19:265, 1981.

[149] C. J. S. Petrie. The rheology of fibre suspensions. *J. Non-Newtonian Fluid Mech.*, 87:369–402, 1999.

[150] I. Kirchenbuechler, D. Guu, N. A. Kurniawan, G. H. Koenderink, and M. P. Lettinga. Direct visualization of flow-induced conformational transitions of single actin filaments in entangled solution. *Nature Comm.*, 5:5060–1–8, 2014.

[151] R. D. Deegan, O. Bakajin, T. F. Dupont, G. Huber, S. R. Nagel, and T. A. Witten. Capillary flow as the cause of ring stains from dried liquid drops. *Nature*, 389:827, 1997.

[152] P. J. Carreau. Rheological equations from molecular network theories. *Trans. Soc. Rheol.*, 16:99–127, 1972.

[153] G. Marrucci and A. Ciferri. Phase equilibria of rod-like molecules in an extensional flow field. *J. Polym. Sci.*, 15:643–648, 1977.

[154] F. Pignon, A. Magnin, and J.-P. Piau. The orientation dynamics of rigid rod suspensions under extensional flow. *J. Rheol.*, 47:371–388, 2003.

[155] S. J. Picken, J. Aerts, R. Visser, and M. G. Northolt. Structure and rheology of aramid solutions: x-ray scattering measurements. *Macromolecules*, 23(16):3849–3854, 1990.

[156] M. P. Lettinga, J. K. G. Dhont, Z. Zhang, S. Messlinger, and G. Gompper. *Soft Matter*, 6:4556–4562, 2010.

[157] S. Hess and I. Pardowitz. On the unified theory for non-equilibrium phenomena in the isotropic and nematic phases of a liquid crystal; spatially inhomogeneous alignment. *Z. Naturforschung A*, 31:554–558, 1981.

[158] P. D. Olmsted. Perspectives on shear banding in complex fluids. *Rheol. Acta*, 47(3):283–300, March 2008.

[159] H. Tang, T. Kochetkova, H. Kriegs, J. K. G. Dhont, and M. P. Lettinga. Shear-banding in entangled xanthan solutions: tunable transition from sharp to broad shear-band interfaces. *Soft Matter*, 14:826–836, 2018.

[160] J.-B. Salmon, A. Colin, and S. Manneville. Velocity profiles in shear-banding wormlike micelles. *Phys. Rev. Lett.*, 90:228303, 2003.

[161] M. E. Helgeson, P. A. Vasquez, E. W. Kaler, and N. J. Wagner. Rheology and spatially resolved structure of cetyltrimethylammonium bromide wormlike micelles through the shear banding transition. *J. Rheol.*, 53:727–756, 2009.

[162] J. Sprakel, E. Sruijt, M. A. Cohen Stuart, N. A. M. Besseling, M. P. Lettinga, and J. van der Gucht. Shear banding and rheochaos in associative polymer networks. *Soft Matter*, 4:1696–1705, 2008.

[163] E. Sarmiento-Gomez, D. Montalvan-Sorrosa, C. Garza, J. Mas-Oliva, and R. Castillo. Rheology and DWS microrheology of concentrated suspensions of the semiflexible filamentous fd virus. *Eur. Phys. J.l E*, 35(5):35, May 2012.

[164] A. Kathory, F. Lequeux, F. Kern, and S. J. Candau. Linear and nonlinear viscoelasticity of semidilute solutions of wormlike micelles at high salt content. *Langmuir*, 9:1456–1464, 1993.

[165] D. Gaudino, R. Pasquino, H. Kriegs, N. Szekely, W. Pyckhout-Hintzen, M. P. Lettinga, and N. Grizzuti. Effect of the salt-induced micellar microstructure on the nonlinear shear flow behavior of ionic cetylpyridinium chloride surfactant solutions. *Phys. Rev. E*, 95:032603, 2017.

[166] K. Kang and J. K. G. Dhont. Double-layer polarization induced transitions in suspensions of colloidal rods. *EPL.*, 84:14005–1–6, 2008.

[167] J. K. G. Dhont, K. Kang, M. P. Lettinga, and W. J. Briels. Shear-banding instabilities. *Korea-Aust. Rheol. J.*, 22:291–308, 2010.

[168] J. F. Maguire and J. P. McTague. Rotational diffusion of sterically interacting rodlike macromolecules. *Phys. Rev. Lett.*, 45:1891–1894, 2010.

[169] M. Harasim, B. Wunderlich, O. Preleg, M. Kroeger, and A. R. Bausch. Direct observation of the dynamics of semiflexible polymers in shear flow. *Phys. Rev. Lett.*, 110:108302, 2013.

[170] D. E. Smith and S. Chu. Response of flexible polymers to a sudden elongational flow. *Science*, 281:1335–1340, 1998.

[171] P. LeDuc, C. Haber, G. Bao, and D. Wirtz. Dynamics of individual flexible polymers in a shear flow. *Nature*, 399:564–566, 1999.

[172] Y. Heo and R. G. Larson. The scaling of zero-shear viscosities of semidilute polymer solutions with concentration. *J. Rheol.*, 49:1117–1128, 2005.

[173] K.-W. Hsiao, C. Sasmal, J. R. Prakash, and C. M. Schroeder. Direct observation of dna dynamics in semidilute solutions in extensional flow. *J. Rheol.*, 61:151–167, 2016.

[174] L. Alvarez-Frances. *Single particle dynamics in liquid crystalline phases formed by filamentous viruses.* PhD Thesis KU Leuven, 2016.

[175] X. Ao, X. Wen, and R. B. Meyer. X-ray scattering from polymer nematic liquid crystals. *Physica A*, 176:63–71, 1991.

[176] J. L. Viovy, M. Rubinstein, and R. H. Colby. Constraint release in polymer melts: tube reorganization versus tube dilation. *Macromolecules*, 24, 1991.

[177] B. Huber, M. Harasim, B. Wunderlich, M. Kroeger, and A. R. Bausch. Microscopic origin of the non-newtonian viscosity of semiflexible polymer solutions in the semidilute regime. *ACS Macro Lett.*, 3:136–140, 2014.

[178] S. Köster. Brownian motion of actin filaments in confining microchannels. *Condens. Matter*, 17:4091–4104, 2005.

[179] J. Rothstein and G. H. McKinley. A comparison of the stress and birefringence growth of dilute, semi-dilute and concentrated polymer solutions in uniaxial extensional flows. *J. Non-Newtonian Fluid Mech.*, 108:275–290, 2002.

[180] H. Nakmura and K. Okano. Pretransitional phenomena in the isotropic phase of a lyotropic liquid crystal of bacterial virus fd. *Phys. Rev. Lett.*, 50:186–189, 1983.

[181] M. Baumgaertel and H. H. Winter. Determination of discrete relaxation and retardation time spectra from dynamic mechanical data. *Rheol. Acta*, 28:512–519, 1989.

[182] J. F. Berret, G. Porte, and J. P. Decruppe. Inhomogeneous shear flows of wormlike micelles: ma master dynamic phase diagram. *Phys.Rev. E*, 55:1668–1676, 1997.

[183] M. W. Liberatore, F. Nettesheim, N. J. Wagner, and L. Porcar. Spatially resolved small-angle neutron scattering in the 1-2 plane: A study of shear-induced phase-separating wormlike micelles. *Phys. Rev. E*, 73(2):020504, 2006.

[184] M. E. Helgeson, M. D. Reichert, Y. T. Hu, and N. J. Wagner. Relating shear banding, structure, and phase behavior in wormlike micellar solutions. *Soft Matter*, 5:3858–3869, 2009.

[185] M. E. Helgeson, L. Porcar, C. Lopez-Barron, and N. J. Wagner. Direct observation of flow-concentration coupling in a shear-banding fluid. *Phys. Rev. Lett.*, 105:084501, 2010.

[186] M. Dijkstra, R. van Roij an, and R. Evans. Wetting and capillary nematization of a hard-rod fluid: A simulation study. *Phys. Rev. E*, 61:051703, 2001.

[187] K. E. Klop, R. P. A. Dullens, M. P. Lettinga, S. A. Egorov, and D. G. A. L. Aarts. Capillary nematisation of colloidal rods in confinement. *Mol. Physics*, 116:2864–2871, 2018.

[188] S. Lerouge, M. Argentina, and J. P. Decruppe. Interface instability in shear-banding flow. *Phys. Rev. Lett.*, 96:088301, 2006.

[189] S. Lerouge, M. A. Fardin, M. Argentina, G. Gregoire, and O. Cardoso. Interface dynamics in shear-banding flow of giant micelles. *Soft Matter*, 4:1808–1819, 2008.

[190] I. Kunita, K. Sato, Y. Tanaka, Y. Takikawa, H. Orihara, and T. Nakagaki. Shear banding in an f-actin solution. *Phys. Rev. Lett.*, 109:248303, 2012.

[191] B. Lonetti, J. Kohlbrecher, L. Willner, J. K. G. Dhont, and M. P. Lettinga. Dynamic response of block copolymer wormlike micelles to shear flow. *J. Phys.: Cond. Mat.*, 20(40):404207, 2008.

[192] M. M. Britton, R. W. Mair, R. K. Lambert, and P. T. Callaghan. Transition to shear banding in pipe and couette flow of wormlike micellar solutions. *J. Rheol.*, 43:897–909, 1999.

[193] Y. T. Hu and A. Lips. Kinetics and mechanism of shear banding in an entangled micellar solution. *J. Rheol.*, 49:1001–1027, 2005.

Publications

Publications with relevance to this thesis are marked with an asterisk and the corresponding chapter of the thesis.

- Lang C. *MMD of polydisperse linear polymers from rheological data: IPP solution via heuristic modeling.* (2015) Akademiker Verlag, Saarbrücken, Germany.
- Lang C., Kohlbrecher J., Porcar L. and Lettinga M.P. The connection between biaxial orientation and shear thinning for quasi-ideal rods. (2016) *P*olymers **8**, 291 * 4.3.2
- Lang C. A Laplace transform method for molecular mass distribution calculation from rheometric data. (2017) *J.* Rheol. **61**, 947
- Lang C. Regularization methods for finding the relaxation time spectra of linear polydisperse polymer melts. (2018) *R*heol. Acta **57**, 339
- Lang C., Hendricks J., Zhang Z., Reddy N. K., Rothstein J. P., Lettinga M. P., Vermant J. and Clasen C. Effects of particle stiffness on the extensional rheology of model-rod-like nanoparticle suspensions. (2018) *S*oft Matter * 5.4
- Lang C., Porcar L., Kriegs H. and Lettinga M. P. A quest for shear banding in ideal and non ideal colloidal rods. (2018) *J.* Phys. D: Appl. Phys. * 5.7
- Lang C., Sellinghoff K., Kohlbrecher J., Porcar L., Radulescu A., Dhont J. K. G. and Lettinga M. P. Morphological influences on the shear thinning behavior of rod-like colloids. In preparation. * 5.3.3
- Lang C. and Lettinga M. P. Towards understanding the shear thinning behavior of polydisperse colloidal rods. In preparation. * 5.6.1

- Lang C., Kohlbrecher J., Porcar L., Abakumov S. and Lettinga M. P. A relaxation time spectrum for semiflexible rodlike colloids. In preparation. * 5.5

FACULTY OF SCIENCE
DEPARTMENT OF PHYSICS AND ASTRONOMY
LABORATORY OF SOFT MATTER AND BIOPHYSICS
Celestijnenlaan 200A, box 2402
B-3001 Leuven
http://www.fys.kuleuven.be/zmb